Single- and Two-Particle Excitations in the Vicinity of Mott Transition

DISSERTATION
zur
Erlangung des Doktorgrades
der Naturwissenschaftlichen Fakultät II
der Martin-Luther Universität, Halle-Wittenberg

vorgelegt von
Berlinson Dominikus Napitu

Gutachter:
Prof. Dr. Jamal Berakdar, Martin-Luther Universität Halle-Wittenberg
Prof. Dr. Steffen Trimper, Martin-Luther Universität Halle-Wittenberg
Prof. Dr. Michael Potthoff, Universität Hamburg
Halle-Saale, den 12. Juli 2010: Tag der Disputation

HALLE-SAALE
2010

ABSTRACT

The present work encompasses theoretical studies of single- and two-particle excitations of strongly correlated systems using the Hubbard model. For single and isotropic two-band system, the particle-particle spectral function is investigated within the framework of the Dynamical Mean Field Theory (DMFT), the ladder approximation and the first order perturbation theory. The results are analyzed and compared for a system in the vicinity of the Mott metal insulator transition (MIT). Under certain conditions specified in this work, the calculated two-particle spectral function is then related to the photocurrent of (one-photon, 2-electrons) experiment. The discussion is then extended to account for spatial fluctuations. To this end, the two dimensional Hubbard model is modified such that it incorporates nonlocal spin fluctuations. The extended Dynamical Mean Field Theory (EDMFT) is then employed to calculate the spin susceptibility, the single-particle spectral function, the optical conductivity and the two-particle spectral function. It is shown that the inclusion of the spin fluctuations assists the formation of pseudogap in the single-particle spectral function. Similarly, the particle-particle sector shows a reduction of the spectral weight as the spin exchange interaction increases. The interplay between the bandwidth anisotropy and the strong correlation in the multiorbital system is discussed using the anisotropic two-band Hubbard Hamiltonian. At first, the transport properties and the two-particle spectral function of the total band at the verge of MIT are calculated within DMFT. The influence of the spatial fluctuation is then addressed by means of EDMFT in the modified two-band Hubbard model that incorporates the spin-spin interaction. It is shown that the spatial fluctuation does not change the physics of the orbitally dependent Mott transition.

ZUSAMMENFASSUNG

Diese Arbeit umfasst die theoretische Untersuchungen der ein- und zwei-Teilchen Anregungen in stark korrelierten Systems im Rahmen des Hubbard Modells. Mittels der dynamische Mean-Field-Theorie (DMFT), der Leiter-Näherung und der Erste-Ordnung-Näherung wird die Spektralfunktion des Einband- und isotrope Zweiband-Hubbard-Modells untersucht. Die Ergebnisse werden in einem System in der Nähe des Mott Übergangs verglichen und analysiert. Die berechnete Spektralfunktion wird unter bestimmten Bedingungen mit Photostrom des (ein-photon, 2 Elektronen) Experiments gekoppelt. Die Diskussion wird dann erweitert, um die räumliche Fluktuation zu berücksichtigen. Hierbei wird das zweidimensionale Hubbard Modell mit Spinfluktuation zusammen mit der erweiterte dynamische Mean-Field-Theorie (EDMFT) angewendet, um die Einteilchen-Spektralfunktion, die optische Leitfähigkeit, und die Zweiteilchen - Spektralfunktion zu berechnen. Es wird gezeigt, dass die Spinschwankungen die Entstehung einer Pseudo-Lücke in der Eintelchen-Spektralfunktion unterstützen. In ähnlicher weise, mit der steigenden Spin-Wechselwirkung verringert sich das Spektralgewichts der Zwei-teilchen-Anregung. Das Zusammenspiel zwischen der Bandbreite-Anisotropie und der stark Korrelationen ist im Rahmen des Zweiband-Hubbard-Modells diskutiert. In dieser Hinsicht werden die Transporteigenschaften sowie die Zweiteilchen-Spektralfunktion durch DMFT ermittelt. Die Wirkung der Spinfluktuation in diesem Modell lässt sich anhand der EDMFT feststellen. Es zeigt sich, dass die räumliche Schwankungen nicht die Physik des orbital-abhänging Mott Übergangs ändern

For my parents,inangtua and my siblings

Contents

CHAPTER 1

Introduction

The fundamental objective of a theory of the solid state is to deduce the structure and properties of systems with large degrees of freedom. In practice, however, one focuses on the most relevant energy scales that contribute to the macroscopic characteristics of the system. This notion is embodied in the Born-Oppenheimer approximation that decouples adiabatically the nuclear from the electronic degrees of freedom. It is the latter that governs various properties of solids involving thermodynamic, electrical and magnetic response. While the problem has been substantially simplified, the Hamiltonian of the system remains intractable due to the fact that the system remains N-body problem consisting of kinetic and electronic interactions. Neglecting all interactions is the crudest approximation in which electrons are envisaged to wander freely through the volume of solid. This is the well-known Sommerfeld's theory which works interestingly well in describing qualitatively or even quantitatively the physical properties of systems like alkali or earth-alkali metals. This simplest model however fails to give a description why some of the solids have metallic, insulating or semiconducting character. The key to the question is to account for the periodic lattice in the independent electron picture which leads to the concept of band theory and the new important property so-called band gap.

Electron-electron interaction is, however, an essential factor for the realistic description of solids. In this connection, one of the most successful concept is the phenomenological theory of Landau or usually noted as Fermi liquid which was developed originally to understand the properties of low temperature liquid He^3. In his theory, the interaction of electrons is assumed to be adiabatically turned on. The non-interacting ground states thus evolves smoothly to the interacting one and there is one to one correspondence between the bare particle of the original system and the "dressed" or the quasiparticle of the interacting system. The notion of quasiparticles is of paramount importance from which an insight to the low-energy excitations (close to Fermi level) of the system may be gained. The concept of Fermi liquid generally holds in a wide range of solids ranging from the simple metals to the transition metal systems. The Landau

theory however breaks down when the electrons are strongly correlated.

Attempts to solve for the full electronic Hamiltonian is pursued in various ways. Early works initiated by Hartree and Fock (HF) remains in the spirit of the independent electron picture with the total wavefunction of the electrons is written in the form of a single Slater determinant. Following the argument of variational principles, one is then left with single-electron equations with the interaction of the electrons being expressed in the form of an effective potential interaction. The Hartree-Fock equations are then solved in a self consistent way. While the approach generally works for various systems, it is a well known problem that HF approximation overestimates band gap value than what is obtained in the experiments. This is mainly due to choice of the total wavefunction that neglects the electronic correlation. An innovative idea that incorporates the correlation yet still maintains the one-particle picture is pioneered by Hohenberg, Kohn and Sham employing the relation of the density and the energy and avoiding the use of wavefunctions. The actual implementation of DFT is manifested in the local density approximation (LDA) which turns out to be useful for ground state calculations of a vast range of compounds.

In the last few years, many new materials have been discovered that exhibit a wide range of fascinating phenomena such as high-temperature superconductivity, heavy fermion system, non Fermi liquid behavior and metal insulator transition. A fundamental characteristic of such a system is that the dynamics of the electrons are strongly influenced by the mutual Coulomb repulsions. Although technological applications of this material is interesting by itself, the most challenging issue is to elucidate the underlying physics. Rapid development of experimental tools with high resolution and sensitivity such as angular resolved photoemission (ARPES), neutron scattering, scanning tunneling microscope (STM) has made possible an accurate measurements of the electronic and magnetic structure. The theoretical description of the experimental data on the other hand is far from being complete. One of the reasons is the lack of controllable approximations. While DFT-LDA and similar approaches have been very useful to unravel the electronic structure of weakly correlated systems, they fail in general in describing the system with strong electronic correlations. This suggests that these phenomena are the results of cooperative many body interactions which can not be captured within a single-particle picture.

The Mott metal-insulator transition is a well-known phenomenon in which the perturbation theory breaks down as the energy scale of electron-electron interactions and the kinetic energy are comparable. In this respect, the behavior of electrons is also expected to deviate from the canonical Fermi-liquid picture. The underlying concept of the origin of Mott insulator is, therefore, different from the one that is driven by the electron-ion interaction described above. The archetypal examples of Mott systems are the transition-metal oxide such as high-T_c cuprates, V_2O_3, $NiS_{2-x}Se_x$. The recently discovered ruthenates oxide $Ca_{2-x}Sr_xRuO_4$ that displays a wealth of phase-diagram involving superconductivity and magnetism has also attracted considerable interests owing to a new class of Mott transition. The development of the dynamical mean field theory (DMFT) is an important step toward a thorough understanding of the role of correlations in general and the metal-insulator transition in particular.

The present work is aimed at studying the dynamic properties of single- and two-particle excitation in the vicinity of Mott metal-insulator transition. The structure of this work is as follows: The next chapter contains an introduction to the Hubbard model and its relation to the metal-insulator transition. This is followed by a brief discussion of the finite temperature Green's function derived within functional integrals. The formulation of the dynamical mean field theory (DMFT) in the Hubbard model is described which is then followed by the extended version of the method/extended dynamical mean field theory (EDMFT) that incorporates spatial fluctuations. The Quantum Monte Carlo (QMC) as a method of the solution of DMFT and EDMFT equations is then sketched. Subsequently, the maximum entropy method used to extract the dynamic properties of DMFT-QMC quantities will be outlined.

Formulation of the two-particle excitation is given in the third chapter. It is started with the derivation of the optical conductivity in the paramagnetic and antiferromagnetic phase within the limit of infinite dimension. The intent of the subsequent section is the formulation of particle-particle excitations within the ladder approximation (LA) in the single and orbitally degenerate cases. This chapter is then completed with the discussion of experimental techniques as well as the derivation of the photocurrent of the particle-particle spectroscopy.

The results of particle-particle excitations in the single and isotropic two-band Hubbard model are given in the fourth chapter. There are two main points of discussion. First, the behavior of the particle-particle excitations at the verge of the metal insulator transition. Second, the accuracy of the results of three different methods DMFT+QMC, DMFT+LA and the first order approximation. The last section of the chapter discusses the metal insulator transition in the two dimensional Hubbard model at and off half-filling. In this case, the extended DMFT together with the modified QMC is employed to calculate various quantities involving the single-particle spectral function, the spin susceptibility, the optical conductivity, the mass enhancements and the scattering rate. At the center of the investigations is the influence of the spatial fluctuation on the phase diagram of 2D Hubbard model and also on the two-particle properties. In the last part, the spectra of pair excitation of 2D Hubbard model are also presented.

The fifth chapter is devoted to the study metal insulator transition in the anisotropic two-band system which is an idealized picture of the strontium ruthenates compound. The chapter starts with a brief discussion of the electronic properties of the ruthenates based on the results of the experiments and first principles calculation. It is then directly followed by the presentation of the results of DMFT for the single- and the two-particle excitations in the paramagnetic and antiferromagnetic phase. The last part of the chapter discusses the influence of spatial fluctuations in the paramagnetic phase. To that end, EDMFT is employed in the modified two-band Hubbard model that incorporates the intersite spin fluctuations. Single- and two-particle Green's function are then calculated within quantum monte carlo that incorporates fermion and boson degrees of freedom. At last, Chapter 6 concludes this work and discusses possible extensions.

CHAPTER 2

Models for Correlated Systems and Methods of Solution

This chapter is intended to introduce the model and the methodology that will be used throughout the thesis. The first section discusses the model under investigations, and its extension to incorporate the orbital degrees of freedom. A related issue discussed also in this section is the correlation- driven metal insulator transition (MIT). Since DMFT is formulated within Green's function formalism and also for completeness reason, brief description of Green's function and related topics are presented in Sec. 2.2. The DMFT method is dicussed in Sec. 2.3. The presentation is started from the notion of the infinite coordination limit and ensued by heuristic derivation of the DMFT self-consistency equations. In the subsequent section, the single-site formulation of DMFT is extended to incorporate the influence of spatial contribution. The method of choice in this respect is the extended dynamical mean field theory (EDMFT) that takes spin-spin interactions into account. In addition to that, various proposals that also include spatial fluctuations will be briefly discussed. The single-site problem of DMFT and EDMFT equations however remains a difficult task. Often, one has to rely on numerical methods that can be applied in a wide range of parameter. In the present work, Hirsch-Fye quantum monte carlo (QMC) will be employed to solve the single-site or the impurity Hamiltonian of DMFT and EDMFT and to calculate the imaginary-time single- and two-particle Green's function. The last section discusses the analytical continuation method which is aimed at transforming the imaginary time quantity into real frequency.

2.1 Models and Related Phenomena

The simplest model that incorporate the basic ingredients of the electron correlations is the Hubbard model. In the standard notation, the Hamiltonian reads

$$H = -\sum_{ij\sigma} t_{ij} c^{\dagger}_{i\sigma} c_{j\sigma} + U \sum_{i} n_{i\uparrow} n_{i\downarrow}. \tag{2.1}$$

where t_{ij} and U correspond to the hopping matrix and Coulomb interaction respectively. This Hamiltonian describes the hopping of electrons and holes in a narrow band with a density-density interaction. In deriving this Hamiltonian, Hubbard assumed the ideal case in which only one band lies at the Fermi energy (ϵ_F) while other bands are energetically far above or below ϵ_F and thus can be neglected [1]. To further simplify the Hamiltonian, he considered only the maximal term of the matrix elements of Coulomb interaction namely intra-atomic contributions. This is supported by the fact that the onsite Coulomb interaction of *3d*-electrons system, is on the order of 20eV which is much larger than that long range Coulomb interactions which varies from 0.025eV to 3eV.

The Hubbard model has a rich phase diagram which can be realized by varying the hopping terms which determines the bandwidth W and the Coulomb interaction U. The model is thus considered to capture the essential physics of the various intriguing phenomena such as magnetism, metal insulator transition, superconductivity. A thorough understanding of the underlying physics of the model is however far from complete. This is perhaps due to the lack of analytical solutions and thus one relies mainly on the approximation which sometimes also not controllable. To date, the only analytical solution available is for one dimensional case which was obtained by Lieb and Wu [2] employing the Bethe ansatz . In contrast, analytical solutions for higher dimensional system are scarcely available. The model however can be treated analytically in two extreme limits. The limit of U=0 or non-interacting system, and t=0 or atomic limit. The former case corresponds to the systems of a free electron gas which is well understood using a theory such as that proposed by Sommerfeld. The atomic case on the other hand describes the system of electrons that are localized in solid since the coupling between sites is absent.

The Hamiltonian of the Hubbard model was independently proposed by three authors: Gutzwiller [3], Kanamori [4] and Hubbard [1]. Initially it was intended to investigate the possibility of ferromagnetism in transition metals. Hubbard soon realized that the model could be also used to study the correlation-driven metal insulator transition which was proposed by Mott. The importance of correlation in the context of metal insulator transition has been realized long before the Hubbard model was introduced. This issue was brought into attention initially by de-Boer and Verway [5] after studying NiO. They pointed out that the insulating phase of NiO could not be described within the standard band theory which predicts a metallic phase. In order to address this problem, Peierls [6] proposed that the insulating state is induced by strong Coulomb repulsion that controls the dynamics of the electrons. Subsequently Mott proposed a simple picture to describe the MIT. He argued that a crystalline array of one electron atoms with a lattice constant *a* at zero temperature should show a sharp transition from a metal to an insulator as the distance between atoms was varied [7, 8]. The microscopic description of this system was provided by Hubbard by introducing the simplified Hamiltonian of $d-$ band system as described above. By means of Green's function method, he showed the existence of MIT, marked by the splitting of the original density of states into two sub-bands, upper and lower bands.

In a realistic system, Mott transition can be realized by varying the bandwidth as well as

the chemical filling [9]. In the first route, the bandwidth is controlled by modifying the lattice parameters or the chemical composition while maintaining the original crystal structure. It is important to note that the on-site interaction U remains unchanged during the above process. Experimentally this method is realized by applying a hydrostatic pressure or substituting elements with different ionic radius and the same valence. Typical example are V_2O_3, $RNiO_3$, R being Pr or Nd, layered ruthenates $Ca_{2-x}Sr_xRuO_4$, two dimensional organic salt $\kappa-$(BEDT-TTF)$_2$Cu[N(CN)$_2$]Cl[10]. In the second route, the electron filling is changed typically by substituting certain elements of the original compound with the one that has different valence. Example for this method are $La_{2-x}Sr_xCuO_4$, $La_{1-x}Sr_xMO_3$, M being a transition metal. Tuning the properties of materials by varying the pressure is generally preferable than doping. The latter leads to some complications due to possible disorder in the structure and for certain cases should be avoided. Besides the two routes mentioned above, one could also use dimensionality as a control parameter. This is motivated by the fact that electronic structure is also modified by lowering the dimensionality. Realistic application of this method is however more difficult than that the two routes described above. Note that the temperature is not considered in this respect as a control parameter, and this distinguishes the Mott transition from that that is driven by temperature. In fact, this metal insulator transition should also occur at zero temperature and therefore is an example of quantum phase transition.

Application of the single band Hubbard model to describe MIT in the transitional metal oxides is realized in several systems. The most prominent examples are cuprates superconductor and vanadium sesquioxide V_2O_3 which shall be briefly discussed below for illustrative purposes. In both cases, it is implicitly assumed that orbital degeneracy is lifted by strong crystal fields effects and thus the relevant low-energy excitation is described by single band near the Fermi energy. As is already pointed out above, V_2O_3 is the example of bandwidth-controlled metal insulator transition. One thus obtains MIT by varying the pressure or by changing the chemical composition. The complete phase diagram has been obtained experimentally in the early 70s by Mc whan et.al [11, 12] and it is reproduced in Fig.2.1. As is clearly seen, vanadium sesquioxide has a rich phase diagram as a function of the temperature and the pressure/doping which involves antiferromagnetic insulating (AFI), paramagnetic metal (PM) and paramagnetic insulator (PI). By varying pressure, one observes the metal insulator transitions that is accompanied by the transition from AFM to PM in the low temperature and PI to PM at high temperatures. This is the classic example of the Mott transition discussed above. The metal-insulator transition in the vanadium sesquioxide is also accompanied by a structural distortion namely from monoclinic in AFI to corundrum structure in the PM and PI. Theoretical description of this system was firstly proposed by Castellani.et.al [13] that pointed out that only doubly degenerate e_g^π orbital is relevant. Based on this observation the physics of V_2O_3 is believed to be captured by the single band Hubbard model at half-filling.

A satisfactory theoretical description of the metal insulator transition within the Hubbard model is, however, not a trivial task and has been a long standing problem. This is in part due to

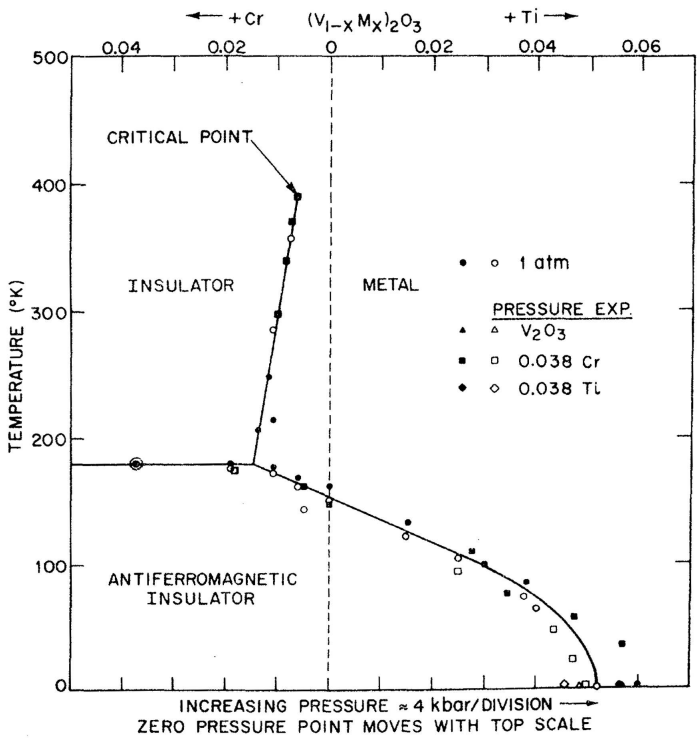

Figure 2.1: Pressure-Temperature phase diagram of the vanadium sesquioxide V_2O_3. The picture is taken from Ref [11].

the nature of the transition which occurs in the intermediate to strong coupling regime of U. In the past, various methods have been introduced to tackle this problem. The solution of Hubbard model mentioned in the previous paragraph distinguishes metal and insulating phase only by the presence of a gap in the spectra. In this picture, the original band is split into two bands (lower and upper band) for strong coupling and merges again as U decreases. This approach however fails to provide a coherent state that epitomizes the Fermi liquid properties.

Brinkman and Rice [14] used a different scenario which they describe as the strongly renormalized Fermi liquid with a reduced low energy scale. In their approach, they employed the Gutzwiller correlated wavefunction [15, 16]

$$|\Psi_G\rangle = g^D|\Phi\rangle = \prod_i \left(1-(1-g)D_i\right)|\Phi\rangle \tag{2.2}$$

where $|\Phi\rangle$ is the single-particle uncorrelated-state typically represented by Slater determinant, $D = \sum_i D_i = \sum_i n_{i\uparrow}n_{i\downarrow}$ is the operator of double occupancies at the same site and g is the variational parameter that determine the number of double occupancies in the system. For $g = 1$ one deals with the uncorrelated state while for $g < 1$ corresponds to the system with reduced double occupancies. Early work of Gutzwiller provided the explicit expression of the ground

state energy obtained from the expectation values of the Hubbard Hamiltonian

$$E = \frac{\langle \Psi_G | H | \Psi_G \rangle}{\langle \Psi_G | \Psi_G \rangle}. \tag{2.3}$$

This energy depends both on g and on the variational parameters which is then determined by a minimization of the ground state energy. The final expression of the ground state energy is then written as

$$E = q\left(\epsilon_\uparrow + \epsilon_\downarrow\right) + Ud, \tag{2.4}$$

where $d \equiv D/N$, N is the number of the lattice sites and $q = 8d(1-2d)$ corresponds to the discontinuities in the single-particle occupation. Finally by minimizing the energy with respect to d one obtains

$$d = \frac{1}{4}\left(1 - \frac{U}{U_c}\right), \tag{2.5}$$

$$q = 1 - \left(\frac{U}{U_c}\right)^2, \tag{2.6}$$

$$\frac{E}{N} = -|\epsilon_\uparrow + \epsilon_\downarrow|\left(1 - \frac{U}{U_c}\right)^2, \tag{2.7}$$

where $U_c = 8|\epsilon_\uparrow + \epsilon_\downarrow|$. Based on this result, Brinkman and Rice derived a relation for the quasiparticle renormalization $Z = \left(1 - \frac{\partial \Sigma(\omega)}{\partial \omega}\Big|_{\epsilon_F}\right)^{-1}$, the effective mass $\frac{m^*}{m}$ and q read

$$\frac{m^*}{m} = Z^{-1} = q^{-1} = \left(1 - \left(\frac{U}{U_c}\right)^2\right)^{-1}. \tag{2.8}$$

Straightforward calculations then give the spin susceptibility

$$\chi_s^{-1} \quad \propto \quad 1 - \left(\frac{U}{U_c}\right)^2. \tag{2.9}$$

From the above equations, it can be seen that when U approaches U_c, both the spin susceptibility and the effective mass diverge whereas the quasiparticle renormalization Z vanishes. While it successfully explains the effects of correlations on the quasiparticle peak, the approximation does not account for the formation of Hubbard bands which starts as the system approaches the insulating phase.

A significant development on this subject has been the introduction of the high dimensional limit [17]. This approach treats both the quasiparticle and Hubbard bands on equal footing and thus is able to describe the continues transition from the weak to the strong coupling regime. More interestingly is that the Mott transition in the three dimensional limit can be treated within a local approximation. The complicated many body methods is thus simplified in such a way that one has to deal with the dynamics fluctuation on certain site while spatial fluctuation can be ignored. Further discussion on this method will be provided in the next section.

Other approaches based on single-particle description such as LDA generally fails to describe the Mott metal insulator transition. Extensions of this approach by incorporating additional correction to the correlation as manifested in the LDA+U and LDA+SIC (self interaction correction) leads to a more reasonable prediction in the insulating phase. A unified description of the correlated metal-insulator transition however can not be provided by these approaches.

A realistic description of most of the materials requires the inclusion of orbital degrees of freedom. Various physical properties of strongly correlated materials, e.g magnetism, charge transfer metal insulator, orbital ordering, are the results of the interplay of the spin, the orbital, and also lattice effects. Numerous recent studies have also shown undoubtedly that the orbital degrees of freedom are of primary importance for understanding the nature of Mott MIT. The inclusion of orbital degeneracy leads to a complex many body Hamiltonian since the interactions terms neglected in the single band Hubbard model are now taken into consideration. The multiband Hubbard model is written as

$$\begin{aligned} H = & -\sum_{ij\alpha\sigma} t_{ij\alpha} c^{\dagger}_{i\alpha\sigma} c_{j\alpha\sigma} + U \sum_{i\alpha} n_{i\alpha\uparrow} n_{i\alpha\downarrow} + \sum_{i\alpha<\beta\sigma\sigma'} (U' - \delta_{\sigma\sigma'} J) n_{i\alpha\sigma} n_{i\beta\sigma'} \\ & -J' \sum_{i\alpha<\beta\sigma} \left(c^{\dagger}_{i\alpha\sigma} c_{i\alpha-\sigma} c^{\dagger}_{i\beta-\sigma} c_{i\beta\sigma} + c^{\dagger}_{i\alpha\sigma} c^{\dagger}_{i\alpha-\sigma} c_{i\beta\sigma} c_{i\beta-\sigma} \right) \end{aligned} \tag{2.10}$$

where $t_{ij\alpha}$ describes hopping of an electron from sites i to j, U and U' represent intra- and inter-orbital Coulomb repulsion respectively and J is the exchange interaction. The last two terms in the Hamiltonian above, correspond to the spin flip and the pair-hopping term respectively with coupling J'. In the above equation index α and β stand for orbital number.

A rigorous analytical solution of this Hamiltonian for all regime of parameters is practically impossible. However, the behavior of the metal insulator transition that depends on the number of orbital degeneracy can be analytically solved using the extended Gutzwiller wavefunction for multiband system. It is shown [18] that the critical coupling U_c depends on the number of the orbital degeneracy N_α, or explicitly $Uc \approx 4(N_\alpha + 1)W$, where W is the bandwidth. It is important to note however that this exact relation is obtained by considering only the local and the interorbital interaction.

2.2 Formalism of Finite Temperature Green's Function

The n particle Green's function is defined as [19]

$$\mathcal{G}^n(\alpha_1\tau_1, \ldots, \alpha_n\tau_n | \alpha'_1\tau'_1, \ldots, \alpha'_n\tau'_n) = \zeta^n \langle T_\tau C_{\alpha_1}(\tau_1), \ldots, C_{\alpha_n}(\tau_n) C^{\dagger}_{\alpha'_n}(\tau'_n), \ldots, C^{\dagger}_{\alpha'_1}(\tau'_1) \rangle \tag{2.11}$$

where $\zeta = -1$ for fermion, T_τ is the time ordering operator in the imaginary time and $C_\alpha(\tau)$, $C^{\dagger}_\alpha(\tau)$ are the imaginary time Heisenberg operator with quantum number α explicitly expressed

as

$$\begin{aligned} C^{\dagger}_{\alpha}(\tau) &= e^{\tau(\hat{H}-\mu\hat{N})}c^{\dagger}_{\alpha}e^{-\tau(\hat{H}-\mu\hat{N})}, \\ C_{\alpha}(\tau) &= e^{\tau(\hat{H}-\mu\hat{N})}c_{\alpha}e^{-\tau(\hat{H}-\mu\hat{N})}. \end{aligned} \tag{2.12}$$

In the above expression, H denotes the Hamiltonian of the electron generally expressed as $H = H_0[c^{\dagger}_{\alpha}c_{\alpha}] + V[c^{\dagger}_{\alpha}c^{\dagger}_{\beta}\ldots c_{\gamma}c_{\delta}]$. μ and $N = \sum_{\alpha} c^{\dagger}_{\alpha}c_{\alpha}$ are the chemical potential and the number operator respectively. The grand partition function for this general Hamiltonian usually expressed as $Z = \mathrm{Tr}e^{-(H-\mu N)}$ can be also written in terms of functional integrals by using the Grassmann variables $\hat{c}^{\dagger}_{\alpha}(\tau), \hat{c}_{\alpha}(\tau)$ as follows

$$Z = \int D[\hat{c}^{\dagger}\hat{c}]e^{-\int_0^{\beta} d\tau \sum_{\alpha} \hat{c}^{\dagger}_{\alpha}(\tau)(\partial_{\tau}-\mu)\hat{c}_{\alpha}(\tau)+H_0[\hat{c}^{\dagger}_{\alpha}(\tau),\hat{c}_{\alpha}(\tau)]+V[\hat{c}^{\dagger}_{\alpha}(\tau)\hat{c}^{\dagger}_{\beta}(\tau)\ldots\hat{c}_{\gamma}(\tau)\hat{c}_{\delta}(\tau)]} \tag{2.13}$$

It is straightforward to obtain the expression of the n particles Green's function in terms of the functional integral formulation

$$\begin{aligned} \mathcal{G}^n(\alpha_1\tau_1,\ldots,\alpha_n\tau_n|\alpha'_1\tau'_1,\ldots,\alpha'_n\tau'_n) &= \zeta^n \frac{1}{Z}\int D[\hat{c}^{\dagger}\hat{c}]\left[e^{-\int_0^{\beta} d\tau \sum_{\alpha} \hat{c}^{\dagger}_{\alpha}(\tau)(\partial_{\tau}-\mu)\hat{c}(\tau)+H[\hat{c}^{\dagger}_{\alpha}(\tau)\hat{c}_{\alpha}(\tau)]}\right. \\ &\quad \left.\hat{c}_{\alpha_1}(\tau_1)\ldots\hat{c}_{\alpha_n}(\tau_n)\hat{c}^{\dagger}_{\alpha'_1}(\tau'_1)\ldots\hat{c}^{\dagger}_{\alpha'_n}(\tau'_n)\right] \qquad (2.14) \\ &= \zeta^n\left\langle \hat{c}_{\alpha_1}(\tau_1)\ldots\hat{c}_{\alpha_n}(\tau_n)\hat{c}^{\dagger}_{\alpha'_1}(\tau'_1)\ldots\hat{c}^{\dagger}_{\alpha'_n}(\tau'_n)\right\rangle. \qquad (2.15) \end{aligned}$$

In the absence of interactions $V = 0$, the single-particle Green's function is written as

$$\begin{aligned} \mathcal{G}_0(\alpha_1\tau_1|\alpha_2\tau_2) &= -\frac{1}{Z_0}\int D[\hat{c}^{\dagger}\hat{c}]\hat{c}_{\alpha_1}(\tau_1)\hat{c}^{\dagger}_{\alpha_2}(\tau_2)e^{-\int_0^{\beta}\sum_{\alpha}\hat{c}^{\dagger}_{\alpha}(\tau)(\partial_{\tau}+\epsilon_{\alpha}-\mu)\hat{c}_{\alpha}(\tau)} \\ &= -(\partial_{\tau}+\epsilon_{\alpha}-\mu)^{-1} \end{aligned} \tag{2.16}$$

where $Z_0 = \int D[\hat{c}^{\dagger}\hat{c}]e^{-\int_0^{\beta} d\tau \sum_{\alpha} \hat{c}^{\dagger}_{\alpha}(\tau)(\partial_{\tau}+\epsilon_{\alpha}-\mu)\hat{c}_{\alpha}(\tau)}$ is the partition function of the non-interacting system and ϵ_{α} is the eigenenergy of the kinetic operator $H_0 = \sum_{\alpha}\epsilon_{\alpha}c^{\dagger}_{\alpha}c_{\alpha}$. The momentum-dependent Green's function in the imaginary time and the Matsubara frequency are related via Fourier transform

$$\begin{aligned} \mathcal{G}(\mathbf{k},\tau) &= \frac{1}{\beta}\sum_n \mathcal{G}(\mathbf{k},i\omega_n)e^{-i\omega_n\tau} \\ \mathcal{G}(\mathbf{k},i\omega_n) &= \int_0^{\beta} d\tau \mathcal{G}(\mathbf{k},\tau)e^{i\omega_n\tau}. \end{aligned} \tag{2.17}$$

Thus the non-interacting Green's function of Eq.(2.16) expressed in terms of the momentum and the Matsubara frequency reads

$$\mathcal{G}_0^{-1}(\mathbf{k},i\omega_n) = i\omega_n + \mu - \epsilon(\mathbf{k}), \tag{2.18}$$

where $\epsilon(\mathbf{k})$ is the momentum representation of eigen energy of H_0 or the dispersion. In the interacting system, the full Green's function as well as the energy can be evaluated by means of

perturbation expansion . The partition function of Eq.(2.13) is expressed in the power series as follows

$$\frac{Z}{Z_0} = \sum_n^{\infty} \frac{(-1)^n}{n!} \int_0^{\beta} d\tau_1 \dots d\tau_n \left\langle V(\hat{c}_\alpha(\tau_1)^\dagger \dots \hat{c}_\gamma(\tau_1)) \dots V(\hat{c}_\alpha(\tau_n)^\dagger \dots \hat{c}_\gamma(\tau_n)) \right\rangle . \quad (2.19)$$

By means of Wick's theorem, one could evaluate the thermal averages of the products $\hat{c}^\dagger$ and $\hat{c}$ in the partition function above and derive systematic rules to construct the Feynman diagrams to all orders. Summation of the so-called irreducible diagrams to all orders provides the exact relation between non-interacting and interacting Green's function. Alternatively, this exact relation can be also derived within the functional integral formalism and will be used in this section. One starts with the generating function for the imaginary time Green's function

$$\begin{aligned} \mathcal{Z}[\overline{\eta}\eta] &= \frac{1}{Z} \int D[\hat{c}^\dagger \hat{c}] \exp\left(- \int_0^{\beta} d\tau \sum_\alpha \left[\hat{c}^\dagger_\alpha(\tau)(\partial - \mu)\hat{c}_\alpha(\tau) + H[\hat{c}^\dagger_\alpha \hat{c}_\alpha] \right.\right. \\ &\quad \left.\left. + \left[\overline{\eta}_\alpha(\tau)\hat{c}_\alpha(\tau) + \hat{c}^\dagger_\alpha(\tau)\eta_\alpha(\tau)\right] \right] \right), \quad (2.20) \\ &= \left\langle \exp\left(- \int_0^{\beta} d\tau \sum_\alpha [\overline{\eta}_\alpha(\tau)\hat{c}_\alpha(\tau) + \hat{c}^\dagger_\alpha(\tau)\eta_\alpha(\tau)] \right) \right\rangle , \end{aligned}$$

which follows from the expression of the partition function of Eq.(2.13) with additional source terms $\eta, \overline{\eta}$. This source terms can be imagined to play the role of a probe that is used to extract the Green's function. Thus by taking the functional derivative with respect to the source terms one obtains the n-particle imaginary time Green's function (explicit expression can be seen in ref [19]). It is important to notice that the generating functional $\mathcal{Z}$ does not ensure that all diagrams of Green's function are connected. The connected Green's function (cumulant) can be generated using the so-called linked cluster theorem that connects $\ln \mathcal{Z}(\overline{\eta}(x), \eta(x))$ and the sum of all connected diagrams. Assigning $\Omega(\overline{\eta}(x), \eta(x))$ as the generating functional of the connected diagrams, the n-particle imaginary-time Green's function $\mathscr{C}^n$ is expressed in the form of a functional derivative with respect to the sources $\eta(x), \overline{\eta}(x)$

$$\mathscr{C}^n(x_1, \dots, x_n | x'_1, \dots, x'_n) = \zeta^n \left. \frac{\delta^{2n}\Omega}{\delta\overline{\eta}(x_1) \dots \delta\overline{\eta}(x_n)\delta\eta(x'_n) \dots \delta\eta(x'_1)} \right|_{\overline{\eta},\eta=0} . \quad (2.21)$$

In the above expression, the variable x replaces $\{\tau, \alpha\}$ and $\overline{\eta}(x)$ is understood as $\overline{\eta}_\alpha(\tau)$. Using the above formula, it is then straightforward to obtain the connected single-particle Green's function

$$\mathcal{G}(x_1|x'_1) \equiv \mathcal{G}^1(x_1|x'_1) = \mathscr{C}^1(x_1, x'_1) = -\langle \hat{c}(x_1)\hat{c}^\dagger(x_{1'}) \rangle . \quad (2.22)$$

Similarly, the evaluation of the two-particle Green's function gives

$$\begin{aligned} \chi(x_1, x_2|x'_1, x'_2) \equiv \mathcal{G}^2(x_1, x_2|x'_1, x'_2) = \\ \left[\mathcal{G}(x_1|x'_1)\mathcal{G}(x_2|x'_2) + \mathcal{G}(x_1|x'_2)\mathcal{G}(x_2|x'_1)\right] - \mathscr{C}^2(x_1, x_2|x'_1, x'_2). \quad (2.23) \end{aligned}$$

In order to generate all connected diagrams that also one-particle irreducible, one usually generate the vertex functions. In doing so, it is convenient first to perform the Legendre transform to obtain a new functional Γ (effective action) as a function of the sources $\phi, \overline{\phi}$. This is written as follows

$$\Gamma[\overline{\phi}, \phi] = -\Omega[\overline{\eta}, \eta] - \sum_{y} \overline{\eta}(y)\eta(y) + \overline{\eta}(y)\phi(y), \tag{2.24}$$

where $\sum_y = \sum_\alpha \int_0^\beta$ and y is a composite variable similarly as defined above for x. The vertex function to all orders can be generated by defining

$$\gamma_{m\overline{\phi},n\phi}(x_1, \ldots, x_n | x'_1, \ldots, x'_n) = \frac{\delta^{m+n}}{\delta\overline{\phi}(x_1)\ldots\delta\overline{\phi}(x_n)\delta\phi(x'_n)\ldots\delta\phi(x'_1)}\Gamma[\overline{\phi}(x)\phi(x)]\Big|_{\overline{\eta},\eta=0}. \tag{2.25}$$

It is straightforward to show the relation between the vertex function and the single-particle Green's function

$$\begin{pmatrix} \gamma_{\overline{\phi}\phi} & \gamma_{\overline{\phi}\overline{\phi}} \\ \gamma_{\phi\phi} & \gamma_{\phi\overline{\phi}} \end{pmatrix} = \zeta \begin{pmatrix} \langle \hat{c}\hat{c}^\dagger \rangle & \langle \hat{c}\hat{c} \rangle \\ \langle \hat{c}^\dagger\hat{c}^\dagger \rangle & \langle \hat{c}^\dagger\hat{c} \rangle \end{pmatrix}^{-1}, \tag{2.26}$$

where the diagonal parts of the matrix on the right hand side are the usual single-particle Green's function while the off diagonals are usually noted as anomalous Green's function which is particularly useful for the systems with symmetry breaking. By assuming that the system is not in the broken symmetry phase, the relation between the vertex and the Green's function in the interacting and the non-interacting case may be written as follows

$$\left[\gamma_{\overline{\phi}\phi}(x, x')\right]^{-1} = \mathcal{G}(x|x'), \tag{2.27}$$

$$\left[\gamma^o_{\overline{\phi}\phi}(x, x')\right]^{-1} = \mathcal{G}_o(x|x'). \tag{2.28}$$

The difference between the vertex function in the interacting and the non interacting case is denoted by the new functional $\Sigma(x|x')$, noted as self energy

$$\gamma_{\overline{\phi}\phi} \equiv \gamma^0_{\overline{\phi}\phi} - \Sigma. \tag{2.29}$$

Transforming into the momentum-frequency representation, one obtains the familiar expression of the Dyson equation

$$\mathcal{G}^{-1}(\mathbf{k}, i\omega_n) = \mathcal{G}_0^{-1}(\mathbf{k}, i\omega_n) - \Sigma(\mathbf{k}, i\omega_n), \tag{2.30}$$

$$= i\omega_n + \mu - \epsilon(\mathbf{k}) - \Sigma(\mathbf{k}, i\omega_n). \tag{2.31}$$

One of the most important experimental observable which can be directly associated with the knowledge of single-particle Green's function is the spectral function $A(\mathbf{k}, \omega)$. It can be derived by first writing the Green's function as follows

$$\mathcal{G}(\alpha t|\alpha' t') = \theta(t - t')\mathcal{G}^>(\alpha t|\alpha' t') + \theta(t' - t)\mathcal{G}^<(\alpha t|\alpha' t') \tag{2.32}$$

where the real time t has been used following the change of the variables $\tau = it$. The explicit expression of the greater $\mathcal{G}^{>}$ and the lesser $\mathcal{G}^{<}$ Green's function read

$$\begin{aligned} i\mathcal{G}^{>}(\alpha t|\alpha' t') &= \frac{1}{Z}\mathrm{Tr}[e^{-(\beta - i(t-t'))(H-\mu N)}\, C_\alpha\, e^{-i(t-t')(H-\mu N)}\, C^\dagger_{\alpha'}] \\ i\mathcal{G}^{<}(\alpha t|\alpha' t') &= -\frac{1}{Z}\mathrm{Tr}[e^{-(\beta + i(t-t'))(H-\mu N)}\, C^\dagger_{\alpha'}\, e^{i(t-t')(H-\mu N)}\, C_\alpha]. \end{aligned} \tag{2.33}$$

By inserting a complete set of states, Eq.(2.32) together with Eq.(2.33) can be casted into

$$\begin{aligned} i\mathcal{G}(\alpha t|\alpha' t') = &\frac{\theta(t-t')}{Z}\sum_{m,n}\langle m|\, e^{-\beta(H-\mu N)} C_\alpha(t)\,|n\rangle\,\langle n|\, C^\dagger_{\alpha'}(t')\,|m\rangle \\ &-\frac{\theta(t'-t)}{Z}\sum_{m,n}\langle n|\, e^{-\beta(H-\mu N)} C^\dagger_{\alpha'}(t')\,|m\rangle\,\langle m|\, C_\alpha(t)\,|n\rangle\,. \end{aligned} \tag{2.34}$$

Fourier transforming into frequency and momentum domain leads to

$$\mathcal{G}(\mathbf{k},\omega) = \frac{1}{Z}\sum_{m,n}|\langle n\,|C_\sigma(\mathbf{k})|\,m\rangle|^2\,\frac{e^{\beta(\epsilon_m-\mu N_m)} + e^{-\beta(\epsilon_n-\mu N_n)}}{\omega - (\epsilon_n - \epsilon_m - \mu) + i\delta}. \tag{2.35}$$

The spectral function is finally obtained by taking the imaginary part of Eq.(2.35)

$$A(\mathbf{k},\omega) = \frac{2\pi}{Z}e^{\beta\Omega}\sum_{m,n}|\langle n|C_\sigma(\mathbf{k})|m\rangle|^2\left[e^{\beta(\epsilon_m-\mu N_m)} + e^{-\beta(\epsilon_n-\mu N_n)}\right]\delta(\omega - \epsilon_n + \epsilon_m + \mu). \tag{2.36}$$

The spectral equation corresponds to the probability of the single-particle excitation and satisfies the sum rule expressed as

$$\int_{-\infty}^{\infty}\frac{d\omega}{2\pi}A(\mathbf{k},\omega) = 1. \tag{2.37}$$

The two-particle vertex function $\gamma_{2\bar{\phi},2\phi}$ can be derived in the similar manner as described above for single particle. In terms of the vertex function, the two-particle Green's function of Eq.(2.23) is finally written as

$$\begin{aligned} \chi(x_1,x_2|x_1'x_2') = &\mathcal{G}(x_1|x_1')\mathcal{G}(x_2|x_2') + \mathcal{G}(x_1|x_2')\mathcal{G}(x_2|x_1') \\ &+ \sum_{x_3,x_4,x_3',x_4'}\mathcal{G}(x_1|x_3)\mathcal{G}(x_2|x_4)\gamma_{2\bar{\phi},2\phi}(x_3,x_4|x_3',x_4') \\ &\mathcal{G}(x_3'|x_1')\mathcal{G}(x_4'|x_2') \end{aligned} \tag{2.38}$$

or in the momentum space

$$\begin{aligned} &\chi(k_1,k_2|k_3,k_4) = \mathcal{G}(k_1)\mathcal{G}(k_2)(\delta_{k_1,k_3}\delta_{k_2,k_4} - \delta_{k_1,k_4}\delta_{k_2,k_3}) \\ &+\delta_{k_1+k_2,k_3+k_4}\mathcal{G}(k_1)\mathcal{G}(k_2)\Gamma(k_1,k_2,k_3,k_4)\mathcal{G}(k_3)\mathcal{G}(k_4) \end{aligned} \tag{2.39}$$

where $k = (\mathbf{k}, i\omega_n)$. The four-point vertex Γ (momentum representation of vertex function $\gamma_{2\bar{\phi},2\phi}$) contains all possible two-particle scattering. In general this four-point vertex consists of particle-hole and particle-particle channel, which can be treated separately. The choice of the diagram in the particle-hole or the particle-particle channel depends on the problem at hand.

2.2.1 Single-Particle Photoemission

One of the most powerful spectroscopic techniques that provides detailed information on the electronic properties of solid is the single-particle photoemission [20, 21, 22]. At the heart of this experimental technique is the photoelectric effect which was firstly observed by Hertz and Hallwachs [23, 24] and later theoretically explained by Albert Einstein in his seminal work on the theory of light quanta [25]. In the experiment (see Fig.2.2), a beam of monochromatized radiation from gas-discharge lamp or synchrotron beamline with known energy is incident on the surface of the sample. The energy of the photon is transferred to solid and is absorbed by an electron with the binding energy $|E_B|$ which stimulates the excitation of electron from its initial state. The electron escapes from the solid whenever its energy is sufficient to surmount the potential barriers at surface. The escaping photoelectron with well-defined energy and direction is detected by electron analyzer. The relation of all energies involved in this process comprises of the kinetic energy of emitted electron E_{kin}, the work function of the solid ϕ , the binding energy $|E_B|$ and the photon energy ν can then be expressed using the conservation of energy as follows

$$E_{kin} = \hbar\nu - \phi - |E_B|. \tag{2.40}$$

In the angle resolved technique, by measuring the kinetic energy of the photoelectron for a given emission angle, one also measures the wave vector or the momentum $\mathbf{K} = \mathbf{p}/\hbar$ of the emitted electron using the relation $\mathbf{K} = \sqrt{2mE_{kin}}/\hbar$. In this case the momentum conservation must be also fulfilled writing $\mathbf{K} + \mathbf{K}_{ph} = \mathbf{K}'$, where $\mathbf{K}_{ph}$ is the momentum of the photon, $\mathbf{K}$ and $\mathbf{K}'$ are the momentum of the electron before and after the absorption of the photon. Since the momentum of the photon ($0.05\mathring{A}$) is negligible with respect to the electron momentum ($\approx 1.6\mathring{A}$) then $\mathbf{K} = \mathbf{K}'$. The parallel part of electron momentum $\mathbf{K}_{\parallel} = K_x + K_y$ and perpendicular $\mathbf{K}_{\perp} = K_z$ components are obtained in terms of the polar (θ) and azimuthal (ϕ) emission angles defined as follows

$$K_x = \frac{1}{\hbar}\sqrt{2mE_{kin}}\sin(\theta)\cos(\phi), \tag{2.41}$$

$$K_y = \frac{1}{\hbar}\sqrt{2mE_{kin}}\sin(\theta)\sin(\phi), \tag{2.42}$$

$$K_z = \frac{1}{\hbar}\sqrt{2mE_{kin}}\cos(\phi). \tag{2.43}$$

In the actual experiments, the photon energy used to bombard the material lies in the range of ultraviolet or x-ray energy which is suitable for investigating the valence band and the core-level states in the solid. ARUPS/ARPES (Angle-resolved ultraviolet photoelectron spectroscopy/ Angle-resolved photoemission spectroscopy) is the common name of the single photoemission operated in the ultraviolet energy scale while XPS (x-ray photoemission spectroscopy) is operated in higher energy. In this context, the source of the photon energy such as synchrotron provides more advantages as one can choose a wide range of energies suitable for studying both the valence and the core states of solids.

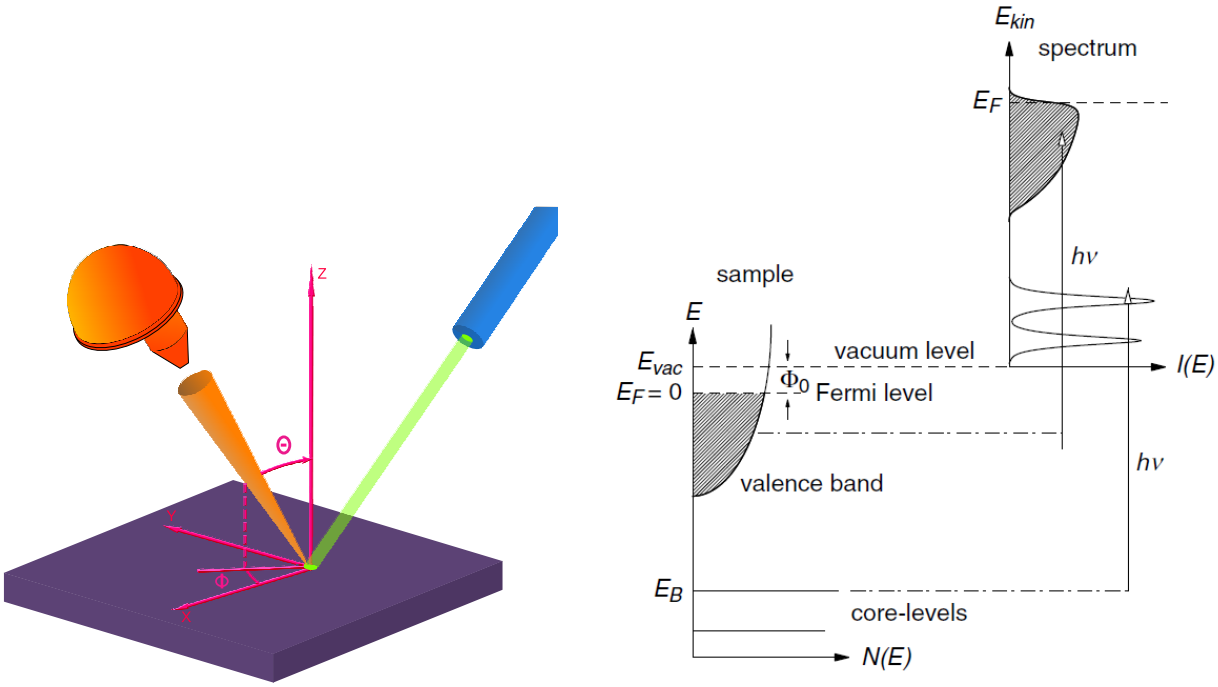

Figure 2.2: Left panel:Geometry of single photoemission in which the emission direction of the excited electron (photoelectron) is specified by polar and azimuthal angles. Right panel shows the energetic of the photoemission process (from reference [21]).

The last decade has witnessed tremendous progress in the angle-resolved photoemission spectroscopy due to the increase of the resolution of the spectra, thus allows to study various complex systems such as cuprates, ruthenates, manganites. Today by using photons with low initial energy $h\nu$ <100eV, one has 2-meV in the energy resolution and 0.2^o in the angular resolution. The simplest way to show why the use of low energy leads to the increase of momentum resolution, is by using the relation of the momentum resolution $\Delta\mathbf{k}_{||}$ and finite acceptance length of the electron analyzer $\Delta\theta$ written as follows

$$\Delta\mathbf{k} \approx \sqrt{\frac{2mE_{kin}}{\hbar^2}}.\cos(\theta).\Delta\theta. \tag{2.44}$$

It is obvious from the above equation that higher momentum resolution can be obtained when using low photon energy (low kinetic energy) but large polar angle θ. The main shortcoming of using low energy is the extreme surface sensitivity implying that the contribution to the total photoemission intensity mainly originates from the topmost layer. This is true in particularly for systems with high structural anisotropy. In order to overcome this problem especially in the case of bulk system, one has to perform ARPES on the atomically clean and well ordered system or flat and clean surface which has to be prepared immediately prior the experiment in an ultrahigh vacuum conditions $\approx$ 5x10^{-11} torr.

Formal description of the photoemission relies on Fermi's golden rule as a result of perturbation theory in the first order. The transition probability w_{fi} for an optical excitation between

N-electron ground state Ψ_i^N and one possible final states Ψ_f^N is written as follows

$$w_{fi} = \frac{2\pi}{\hbar} |\left\langle \Psi_f^N | \Delta | \Psi_i^N \right\rangle|^2 \delta(E_f^N - E_i^N - \hbar\nu), \tag{2.45}$$

where E_i^N and E_f^N are the energies of the initial and the final state of the N-electron system respectively. Microscopically, the interaction between light and matter is embodied in the Hamiltonian particularly in the coupling between the vector potential of the electromagnetic field $\mathbf{A}(\mathbf{r})$ and the momentum of the electron in the system. In the minimal coupling, Hamiltonian reads

$$\begin{aligned} H &= \frac{p^2}{2m} + V - \left[\frac{e}{2mc}(\mathbf{A}(\mathbf{r}).\mathbf{p} + \mathbf{p}.\mathbf{A}(\mathbf{r}))\right] + \frac{e^2}{2mc^2}|\mathbf{A}(\mathbf{r})|^2, & (2.46)\\ &= H_0 + \Delta. & (2.47) \end{aligned}$$

The coupling of the photon and the electron in the solid (third and fourth terms in equation (2.46)) can be further simplified by noting that the quadratic term is relevant only for light with high intensity. In addition to that by using the Coulomb gauge $\nabla.\mathbf{A}(\mathbf{r}) = 0$ as well as the commutator relation $[\mathbf{p}, \mathbf{A}] = -i\hbar\nabla.\mathbf{A}(\mathbf{r})$ the light-matter interaction reduces to

$$\Delta = -\frac{e}{mc}\mathbf{A}(\mathbf{r}).\mathbf{p}. \tag{2.48}$$

In the well-known dipole approximation, $\mathbf{A}(\mathbf{r}) = \mathbf{A}_0 e^{i\mathbf{k}.\mathbf{r}} \approx \mathbf{A}_0$ the coupling Hamiltonian is expressed as $\Delta = -\frac{e}{mc}\mathbf{A}_0.\mathbf{p}$. Excitation of a single electron by photon leaves the system with $N-1$ particles in the excited states. A detailed description of how the ejected electrons interacts with the rest of the system left behind is however a complex process. The so-called sudden approximation offers a drastic simplification to this problem by assuming that the interaction between the photoelectron and the rest of the system is negligible. This is due to the fact that electron is instantaneously removed and the potential effective of the system changes discontinuously at that instant. Based on this consideration the relation of the state and the energy before and after the emission of the electron is expressed as follows

$$\begin{aligned} \Psi_f^N &= \mathcal{A}\phi_f^{\mathbf{k}}\Psi_f^{N-1}, & (2.49)\\ E_f^N &= E_f^{N-1} - E_{kin}, & (2.50)\\ E_i^N &= E_i^{N-1} - E_B^{\mathbf{k}}, & (2.51) \end{aligned}$$

where $\mathcal{A}$ is the operator that antisymmetrizes the N-electron wave function, Ψ_f^{N-1} is the final state for (N-1)-electrons system, $\phi_f^{\mathbf{k}}$ is the wave function of the photoelectron with the momentum $\mathbf{k}$, $E_B^{\mathbf{k}}$ is the binding energy of photoelectron with kinetic energy E_{kin} and momentum $\mathbf{k}$.

The sudden approximation described above is basically one part of the photoemission process introduced in the 1960s by Berglund and Spicer [26] for angle resolved photoemission. In their model, the complex process of electron ejection by the photon is subdivided into three independent steps consisting (i) excitation of the electron in the bulk solid, (ii) scattering of the electron during travel to the surface and (iii) the escape of the photoelectron from the solid. The

total photoemission intensity is then obtained by the product of these three independent parts. Nevertheless, the contribution of the second step due to the inelastic process is usually neglected or subtracted. Following the expression of Eq.(2.49), the initial state can be expressed as

$$\Psi_i^N = \mathcal{A}\phi_i^{\mathbf{k}}\Psi_i^{N-1}, \tag{2.52}$$

the matrix elements of transition probability w_{fi} is then written as

$$\left\langle \Psi_f^N \right| \Delta \left| \Psi_i^N \right\rangle = \left\langle \phi_f^{\mathbf{k}} \right| \Delta \left| \phi_i^{\mathbf{k}} \right\rangle \left\langle \Psi_m^{N-1} \right| \left. \Psi_i^{N-1} \right\rangle, \tag{2.53}$$

where $M_{fi}^{\mathbf{k}} = \left\langle \phi_f^{\mathbf{k}} \right| \Delta \left| \phi_i^{\mathbf{k}} \right\rangle$ is the dipole matrix element of single electron and the last part denotes the overlap integral. The measured photocurrent as a function of E_{kin} at momentum $\mathbf{k}$ is finally written as

$$J(\mathbf{k}, E_{kin}) = \sum_{fi} w_{fi} \tag{2.54}$$

$$= \sum_{fi} \left| M_{fi}^{\mathbf{k}} \right|^2 \sum_n |c_{ni}|^2 \, \delta(E_{kin} + E_n^{N-1} - E_i^N - \hbar\nu), \tag{2.55}$$

where $|c_{ni}|^2 = \left\langle \Psi_m^{N-1} \right| \left. \Psi_i^{N-1} \right\rangle$ denotes the probability to remove electron from site i which leaves the system in the excited state m. Recalling the result obtained in the previous section particularly in the equation (2.36) one observes the relation of the imaginary part of the Green's function and the photocurrent of ARPES.

2.3 Dynamical Mean Field Theory

At the heart of the mean field like approach lies the idea of reducing the complexity of many body problems into a more manageable two-body problems consists of single site o and the effective field that represents all sites except the selected site o. The classic example of the use of this method is the mean field approximation of Ising model where one obtains a solution for spontaneous magnetization. In this classical system, the influence from the surrounding environments of the chosen spin S_o is replaced by the effective magnetic field namely h_{eff} that contains the average of spin fluctuation $\langle S_i \rangle$ and the coupling between the field and site o.

The extended version of mean field approach into quantum systems is manifested in dynamical mean field theory (DMFT) which is originated from the study of Hubbard model in the infinite dimensional limit. By employing Gutzwiller-type variational method and perturbation theory, Metzner and Vollhardt [17] pointed out that in the infinite coordination limit, spatial fluctuations are completely suppressed and thus the self energy becomes local.

$$\Sigma(\mathbf{k}, i\omega_n) = \Sigma(i\omega_n) \tag{2.56}$$

It is important to note however, that a proper scaling of hopping amplitude in the limit of infinite coordination is necessary to ensure a finite kinetic energy. This can be clearly seen for example

from the dispersion relation of hypercubic lattice that include only nearest neighbor reads

$$\epsilon(\mathbf{k}) = -2t \sum_{j=1}^{d} \cos k_j \tag{2.57}$$

where t and d correspond to hopping amplitude and dimensionality respectively. Density of states (DOS) is then obtained from the relation

$$D(\epsilon) = \frac{1}{N} \sum_{\mathbf{k}} \delta(\epsilon - \epsilon(\mathbf{k})) \tag{2.58}$$

which then gives

$$D(\epsilon) = \frac{1}{2t\sqrt{\pi d}} \exp\left(-\frac{\epsilon^2}{2t\sqrt{d}}\right) \tag{2.59}$$

Thus it is clear that finite DOS will only be obtained after scaling the hopping amplitude reads

$$t = \frac{t^*}{\sqrt{2d}} \tag{2.60}$$

Substituting the above rescaled-hopping amplitude to Eq.(2.59) gives DOS that free from dimensionality parameter reads

$$D(\epsilon) = \frac{1}{\sqrt{2\pi}} \exp\left(-\frac{\epsilon^2}{\sqrt{2}}\right) \tag{2.61}$$

where t^* is fixed to unity. In contrast, since Coulomb interaction purely local, it remains unchanged even in the high dimensional limit and thus does not need a rescaling.

Another significant finding in the limit of infinite dimensions is the result of correlation energy of $d = 3$ which quantitatively close to that in $d = \infty$. As a consequence, results of infinite dimensions remain relevant in the realistic case and can be applied directly in the three dimensional system.

2.3.1 Self Consistency Equations - Impurity Hamiltonian

The successful practical implementation of the large d limit is based on the mapping of the original lattice problem onto the corresponding impurity Hamiltonian [27, 28]. In order to show this, one can start by rewriting the action in Eq.(2.13) using Hubbard model as follows

$$S = \int_0^\beta d\tau \sum_{i\sigma} \left(c^\dagger_{i\sigma}(\tau) \left[\frac{\partial}{\partial \tau} - \mu \right] c_{i\sigma}(\tau) \right) - \sum_{ij\sigma} t_{ij} c^\dagger_{i\sigma}(\tau) c_{j\sigma}(\tau) + U \sum_i n_{i\uparrow}(\tau) n_{i\downarrow}(\tau) \tag{2.62}$$

Following the classical mean field analogy, all fermions are traced out except for site o, thus the final effective action that describes the interaction between the the chosen site o and the average field is written as follows

$$S = -\int_0^\beta d\tau_1 \int_0^\beta d\tau_2 \sum_\sigma c^\dagger_{o\sigma}(\tau_1) \mathcal{G}_o^{-1}(\tau_1 - \tau_2) c_{o\sigma}(\tau_2) + U \int_0^\beta d\tau n_{o\uparrow}(\tau) n_{o\downarrow}(\tau) \tag{2.63}$$

where β is the inverse temperature and $\mathcal{G}_o^{-1}(\tau_1 - \tau_2)$ play role of the Weiss effective field. The relation between the original lattice and the Weiss field is then expressed via DMFT Dyson equation reads

$$\mathcal{G}_0^{-1}(i\omega_n) = \Sigma(i\omega_n) + \mathcal{G}^{-1}(i\omega_n). \tag{2.64}$$

In terms of free density of states (DOS) $D(\epsilon)$, the self consistency condition of DMFT can be straightforwardly written as follows

$$\mathcal{G}(i\omega_n) = \int d\epsilon \frac{D(\epsilon)}{i\omega_n - \epsilon + \mu - \Sigma(i\omega_n)}. \tag{2.65}$$

Expression in Eq.(2.63)-Eq.(2.65) thus close self consistent relation of DMFT.

It is straightforward to show that the Hamiltonian representation of effective action in Eq.(2.63) is the Anderson Hamiltonian reads [29]

$$H = \sum_{k\sigma} \epsilon_k c^\dagger_{k\sigma} c_{k\sigma} + V \sum_{k\sigma} [c^\dagger_{k\sigma} c_{o\sigma} + c^\dagger_{o\sigma} c_{k\sigma}] - \epsilon_d \sum_{\sigma} n_{o\sigma} + U n_{o\uparrow} n_{o\downarrow}. \tag{2.66}$$

This Hamiltonian describes the impurity on site o with Coulomb interaction U that is embedded in the conduction band represented by ϵ_k. Solving this Hamiltonian thus equivalent to solving the single site action of Hubbard model expressed above.

Extending the DMFT self consistency into the antiferromagnetic phase can be done straightforwardly [28]. In order to take account of two sub lattices A and B in the Neel state, the kinetic part of Hubbard Hamiltonian may be written as follows

$$H = \sum_{\sigma \mathbf{k}} \epsilon(\mathbf{k}) \left[c^\dagger_{A\mathbf{k}\sigma} c_{B\mathbf{k}\sigma} + c^\dagger_{B\mathbf{k}\sigma} c_{A\mathbf{k}\sigma} \right] + \sum_{\sigma \mathbf{k}} \sigma h \left[c^\dagger_{A\mathbf{k}\sigma} c_{A\mathbf{k}\sigma} - c^\dagger_{B\mathbf{k}\sigma} c_{B\mathbf{k}\sigma} \right] \tag{2.67}$$

where h stands for external magnetic field, and momentum summation runs over all values of $\mathbf{k}$ in the magnetic Brillouin zone. Following Eq.(2.26), the Green's function are then obtained by inverting matrix

$$\begin{pmatrix} \zeta_{A\sigma} & -\epsilon(\mathbf{k}) \\ -\epsilon(\mathbf{k}) & \zeta_{B\sigma} \end{pmatrix} \tag{2.68}$$

where $\zeta_{A\sigma} = i\omega_n + \mu - \sigma h - \Sigma_{A\sigma}$ and $\zeta_{B\sigma} = i\omega_n + \mu + \sigma h - \Sigma_{B\sigma}$. The self consistency equation in the antiferromagnetic phase then explicitly reads

$$\mathcal{G}_{\alpha\sigma}(i\omega_n) = \zeta_{\overline{\alpha}\sigma} \int d\epsilon \frac{D(\epsilon)}{\zeta_{A\sigma}\zeta_{B\sigma} - \epsilon^2} \tag{2.69}$$

with $\alpha = A, B$ and $\overline{\alpha} = B, A$.

The details about lattice structure in the DMFT calculation enters from density of states $D(\epsilon)$. In three dimensional system, it has been previously shown that DOS becomes Gaussian like distribution in the infinite dimensional limit. The Gaussian DOS in $d \to \infty$ however does not have real band edges and thus becomes unphysical. This is overcome by replacing Gaussian

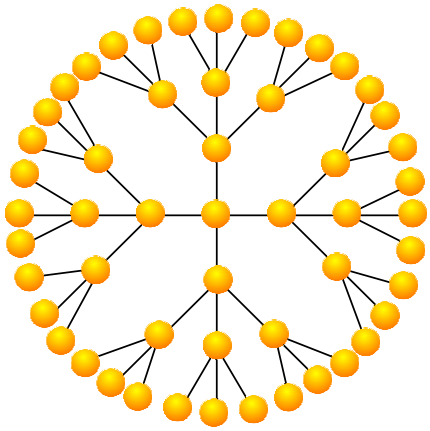

Figure 2.3: Bethe lattice with coordination number $z = 4$

DOS with that Bethe lattice which is not regular lattice but form a treelike structure [1](see Fig.2.3) The density of states of Bethe lattice is written as

$$D(\epsilon) = \frac{2}{\pi t}\sqrt{(1-(\epsilon/t)^2)} \tag{2.70}$$

where t is the kinetic energy parameter.

2.4 Extended Dynamical Mean Field Theory

While some strongly correlated phenomena can be described within single site approximation with local self energy, the approach becomes unsuitable in the system with pronounced non-local fluctuation. This is due to fact that DMFT treats all non-local correlations at the level of Hartree approximation. As will be shown in Chapter 4, the interplay of local and non-local interactions is also essential in Mott transition. The changes in the low-energy of two-particle influence the character of single-particle excitation.

Over the past few years, a number of proposals have been put forward to incorporate the spatial fluctuation in DMFT. They are different in the way the non-local fluctuation effects are included in the DMFT. In the cluster generalization of DMFT, the momentum dependency of self energy is introduced by mapping a lattice into a number of sites that are embedded in the bath together with self consistency relation. The choice of cluster is, however, not unique and two different approaches are usually applied namely cluster dynamical mean field approximation (CDMFT) and dynamical cluster approximation (DCA) [31, 32].

In contrast with quantum cluster approach, there are several approaches that retains single site nature of DMFT but modifies self energy or even Hamiltonian in order to include the non-local effects. DMFT+$\Sigma_{\mathbf{k}}$ proposed by Kuchinskii.et.al [33, 34] introduces the non-locality directly in the self energy. In their approach the interacting Green's function within local self

[1]Further discussions see [30].

energy is expressed as follows

$$\mathcal{G}(\mathbf{k}, i\omega_n) = \frac{1}{i\omega_n + \mu - \epsilon(\mathbf{k}) - \Sigma(i\omega_n) - \Sigma(\mathbf{k}, i\omega_n)} \tag{2.71}$$

where $\Sigma_{\mathbf{k}}(i\omega_n)$ is the non-local contribution of self energy due to either interaction of electron with collective modes, order parameter fluctuations or other non-local contribution. Although there are two self energy in the above equation, they emphasize that there is no double counting problem to appear as the local contribution of $\Sigma(\mathbf{k}, i\omega_n)$ will eventually vanish in the limit of infinite dimensionality and thus is not taken into account in the standard DMFT. The momentum dependent self energy is chosen in such a way it contains the effects of scattering of electrons from short-range spin density wave (SDW) or charge density wave (CDW) fluctuations. Explicitly this is written as

$$\Sigma(\mathbf{k}, i\omega_n) = \Sigma_{n=1}(\mathbf{k}, i\omega_n) \tag{2.72}$$

where

$$\Sigma_n(\mathbf{k}, i\omega_n) = \Delta \frac{s(n)}{i\omega_n + \mu - \Sigma(i\omega_n) - \epsilon_n(\mathbf{k}) + in\nu_n\kappa - \Sigma_{n+1}(i\omega_n, \mathbf{k})} \tag{2.73}$$

Δ characterizes the energy scale,$\kappa = \xi^{-1}$ is the inverse correlation length of the short-range SDW (CDW) fluctuations, $\epsilon_n(\mathbf{k}) = \epsilon(\mathbf{k}+\mathbf{q})$ and $\nu_n = |\nu^x_{\mathbf{k}+\mathbf{q}}| + |\nu^y_{\mathbf{k}+\mathbf{q}}|$ for odd n while $\epsilon_n(\mathbf{k}) = \epsilon(\mathbf{k})$ and $\nu_n = |\nu^x_{\mathbf{k}}| + |\nu^y_{\mathbf{k}}|$ for even n. Finally $s(n)$ represents a combinatorial factor of diagrams that corresponds to the type of fluctuation. Solving the recursion problem in the non-local self energy is thus additional effort in the calculation which can be done relatively fast. The rest of the computational scheme follows that of DMFT as outlined in the previous section.

Dynamical vertex approximation (DΓA) [35] restores the non-locality of DMFT in the same spirit with DMFT+$\Sigma_{\mathbf{k}}$. In this case, the **k**-dependent self energy is obtained from the knowledge of the two-particle vertex function where the relation between both quantities is expressed by the Schwinger-Dyson equation as follows

$$\Sigma(\mathbf{k}, i\omega_n) = U\frac{n}{2} - \sum_{\mathbf{kq}, i\nu' i\nu} \Gamma^{i\omega i\nu' i\nu\uparrow\downarrow}_{\mathbf{k},\mathbf{k}'\mathbf{q}} \mathcal{G}(\mathbf{k}'+\mathbf{q}, i\nu'+\nu)\mathcal{G}(\mathbf{k}', i\nu'+i\nu')\mathcal{G}(\mathbf{k}+\mathbf{q}, i\omega'+i\nu) \tag{2.74}$$

The reducible vertices $\Gamma^{i\omega i\nu' i\nu\uparrow\downarrow}_{\mathbf{k},\mathbf{k}'\mathbf{q}}$, in principle, can be obtained through the self-consistent solution of the parquet equations. However, in the specific case such as the effect of paramagnon fluctuations, one restricts to the ladder subset of the parquet diagrams. In this respect, the momentum-dependent vertex is written as follows

$$\Gamma^{i\omega i\nu' i\nu\uparrow\downarrow}_{\mathbf{k},\mathbf{k}'\mathbf{q}} = \frac{1}{2}\left(\Gamma^{i\omega i\nu' i\nu}_{s,\mathbf{q}} - \Gamma^{i\omega i\nu' i\nu}_{c,\mathbf{q}}\right) + \Gamma^{i\omega, i\omega+i\nu, i\nu'-i\nu}_{s,\mathbf{k}'-\mathbf{k}} - \frac{1}{2}\left(\Gamma^{i\omega i\nu' i\nu}_{s,loc} - \Gamma^{i\omega i\nu' i\nu}_{c,loc}\right) \tag{2.75}$$

where the first two terms describes the longitudinal and transverse paramagnon respectively and the last terms subtracts the double-counted local contribution. Substitution of Eq.(2.75) into Eq.(2.74) finally gives the momentum-dependent self energy reads

$$\begin{aligned}\Sigma(\mathbf{k}, i\omega_n) = U\frac{n}{2} + \frac{1}{2}TU\sum_{\nu'\nu\mathbf{q}} \chi_0(\mathbf{q}, i\nu, i\nu')\Big(3\Gamma^{i\omega i\nu' i\nu}_{s,\mathbf{q}} - \Gamma^{i\omega i\nu' i\nu}_{c,\mathbf{q}} \\ + \Gamma^{i\omega i\nu' i\nu}_{s,loc} - \Gamma^{i\omega i\nu' i\nu}_{c,loc}\Big)\mathcal{G}(\mathbf{k}+\mathbf{q}, i\omega+i\nu)\end{aligned} \tag{2.76}$$

with $\chi_0(\mathbf{q}, i\nu, i\nu') = -T\sum_{\mathbf{k}} \mathcal{G}(\mathbf{k}, i\nu')\mathcal{G}(\mathbf{k}+\mathbf{q}, i\nu + i\nu')$ is momentum dependent particle-hole quantity and $\mathcal{G}(\mathbf{k}, i\omega_n)$is the $\mathbf{k}$-dependent Green's function with DMFT self energy. The main issue in the practical implementation of this scheme is the evaluation of the four-point vertex function $\Gamma^{v',v,\omega}_{s(c),loc}$ that requires local susceptibility $\chi^{vv',\omega\sigma\sigma'}_{loc}$ [2]with three Matsubara frequencies. This quantity is usually calculated directly within the DMFT loops which according to the original work of Ref.[35] can be done straightforwardly within the exact diagonalization scheme. Once this is obtained, the fully irreducible vertex function can then be determined. At last, one obtains the momentum-dependent self energy of DΓA following the lines described above.

The alternative route to incorporate the effects of non-local correlation in DMFT is offered by Extended Dynamical Mean Field Theory (EDMFT). In contrast with the above-presented approach, the feedback of spatial fluctuations in EDMFT are directly included in the local self energy [36, 37, 38, 39, 40]. This is done by extending the Hubbard model with additional intersite terms such as spin-spin interactions. Hubbard model (2.1) is then written as

$$H = \sum_{ij} t_{ij} c^{\dagger}_{i\sigma} c_{j\sigma} + U\sum_{i} n_{i\uparrow} n_{i\downarrow} + \sum_{ij} I_{ij}\mathbf{S}_i.\mathbf{S}_j, \tag{2.77}$$

where the last term describes spin exchange interaction with coupling I. Following the argument of infinite coordination limit, the hopping term t_{ij} has to be scaled so as to retain finite kinetic energy. This can then be written as $t_{ij} \to t/\sqrt{d}$. The same also applies to intersite interactions I_{ij} where, after scaling gives $I_{ij} \to I/\sqrt{d}$. As is outlined above, the most significant consequences of infinite dimensional approximation is the locality of self energy. In the EDMFT, one thus has the momentum-independent self energy $\Sigma(\mathbf{k}, i\omega_n) \approx \Sigma(i\omega_n)$ in the single-particle as well as in the two-particle $\Pi(\mathbf{q}, i\omega_m) \approx \Pi(i\omega_m)$. Self consistency equations of EDMFT, can be derived in a manner similar to that described for DMFT. Within the path integral formalism, the effective action of the single site problem can thus be written as follows

$$\begin{aligned} S_{eff} = &-\int_0^\beta d\tau_1 \int_0^\beta d\tau_2 c^{\dagger}_{0\sigma}(\tau_1)\mathcal{G}_0^{-1}(\tau_1-\tau_2)c_{0\sigma}(\tau_2) + \int_0^\beta U n_{0\uparrow}(\tau) n_{0\downarrow}(\tau) \\ &-\frac{1}{2}\int_0^\beta d\tau_1 \int_0^\beta d\tau_2 \mathbf{S}_0(\tau_1)\chi_0(\tau_1-\tau_2)\mathbf{S}_0(\tau_2). \end{aligned} \tag{2.78}$$

The impurity site of EDMFT is now coupled not only with the fermionic bath that is represented by the Weiss field but also with bosonic bath that is dictated by the two-particle field quantity $\chi_0(\tau_1 - \tau_2)$. It is clear that in the absence of the latter term one again obtains the standard DMFT equation. The intersite fluctuations is thus manifested in the coupling between local spin and bosonic bath. For the purpose of numerical solution, the last term of action can be decoupled by means of Hubbard Stratonovich transformation

$$\begin{aligned} S_{eff} = &-\int_0^\beta d\tau_1 \int_0^\beta d\tau_2 c^{\dagger}_{0\sigma}(\tau_1)\mathcal{G}_0^{-1}(\tau_1-\tau_2)c_{0\sigma}(\tau_2) + \int_0^\beta U n_{0\uparrow}(\tau) n_{0\downarrow}(\tau) \\ &-\frac{1}{2}\int_0^\beta d\tau_1 \int_0^\beta d\tau_2 \phi_0(\tau_1)\chi_0^{-1}(\tau_1-\tau_2)\phi_0(\tau_2) + \int_0^\beta d\tau \phi_0(\tau)\mathbf{S}_0, \end{aligned}$$

[2] $\chi^{vv'\omega}_{s(c),loc} = \chi^{v}_{0\omega,loc}\delta_{vv'} + \chi^{v}_{0\omega,loc}\Gamma^{v',v,\omega}_{s(c),loc}\chi^{v'}_{0\omega,loc}$

where $\phi_0(\tau)$ stands for bosonic field. Further details about the implementation of the numerical solution of single site action consisting of fermion and boson degrees of freedom will be described in the subsequent section. Dyson equations of EDMFT for single and two particles can be expressed as

$$\mathcal{G}^{-1}(i\omega_n) = \mathcal{G}_0^{-1}(i\omega_n) - \Sigma(i\omega_n), \tag{2.79}$$

$$\chi^{-1}(i\omega_m) = \Pi^{-1}(i\omega_m) - \chi_0(i\omega_m), \tag{2.80}$$

where $\omega_n = (2n+1)\pi/\beta$ and $\omega_m = 2m\pi/\beta$ are Matsubara frequencies for fermions and bosons respectively. In terms of the non-interacting DOS of the single particle $D(\epsilon)$ and the two particles $\rho_I(\epsilon)$, the self consistency condition can be written as follows

$$\mathcal{G}(i\omega_n) = \int d\epsilon \frac{D(\epsilon)}{i\omega_n - \epsilon + \mu - \Sigma(i\omega_n)}, \tag{2.81}$$

$$\chi(i\omega_m) = \int d\epsilon \frac{\rho_I(\epsilon)}{\Pi^{-1}(i\omega_m) + \epsilon}. \tag{2.82}$$

Eq.(2.78) to Eq.(2.82) represent a closed set of self-consistent equations of EDMFT. The effective action of Eq.(2.78) can be also expressed in terms of the impurity Hamiltonian as

$$\begin{aligned} H = &\sum_{k\sigma} \epsilon_k c^\dagger_{k\sigma} c_{k\sigma} + V \sum_{k\sigma} (c^\dagger_{k\sigma} d_\sigma + d^\dagger_\sigma c_{k\sigma}) - \mu n_d + U n_{d\uparrow} n_{d\downarrow} + \sum_q \omega_q \mathbf{h}^\dagger_q . \mathbf{h}_q \\ &+ I \sum_q \mathbf{S}_d . (\mathbf{h}^\dagger_{-q} + \mathbf{h}_q) \end{aligned} \tag{2.83}$$

where $n_d = \sum_\sigma d^\dagger_\sigma d_\sigma$ and $\mathbf{S}_d = \frac{1}{2} \sum_{\sigma\sigma'} d^\dagger_\sigma \tau_{\sigma\sigma'} d_{\sigma'}$ is the single-particle occupation and the spin operator respectively, $\mathbf{h}_q = (h_{q1}, h_{q2}, h_{q3})$ stands for the vector-bosonic bath with commutation relation $\left[h^\alpha_q, h^\beta_{q'}\right] = \delta_{qq'}\delta_{\alpha\beta'}$.

2.5 Quantum Monte Carlo

One of the main difficult issues in the dynamical mean field theory is the solution of the impurity Hamiltonian or equivalently the single site action. There are two broad categories of impurity solver namely perturbative and non-perturbative based approaches. The former approach treats the Coulomb interaction U or the hybridization coupling perturbatively and considers up to second- or even higher-order contributions. The latter treats the impurity Hamiltonian in a different manner namely by performing numerically exact calculation. Examples of perturbative solver are Iterated Perturbation Theory (IPT) [41, 42, 43], Non Crossing Approximation (NCA)[44] and Fluctuation Local EXchange (FLEX)[45]. The exact Diagonalization [46], the Quantum Monte Carlo (QMC)[47, 48, 49], the Density Matrix Renormalization Group (DMRG)[50], the numerical renormalization group [51] represent the other one. The main advantage of perturbative techniques is that most of the integral equations involved in the calculation can be solved with much less numerical effort. Thus, in the computationally demanding task e.g multiorbitals system or

cluster extension DMFT, this approach provides more numerical advantage. Both IPT and FLEX are perturbative expansion in the Coulomb interaction. The self energy of the former contains second-order Feynman diagram contributions, while the latter consists of different contributions from the spin and the pair fluctuation. IPT captures both metallic and insulating regions in the half-filled single band Hubbard model but gives unphysical results in other fillings. There has been a proposal to overcome this problem by introducing an ansatz for the self energy that interpolates between the weak and the strong couplings. The results within this method have been shown to be in a good agreement with that exact diagonalization method for different number of fillings [52]. FLEX on the other hand is known to give reasonable results only in the Fermi liquid regime for the single and the multiorbital system. In contrast to the above methods, perturbative approach within NCA is based on the hybridization expansion. It is applicable in the weak and the strong coupling but breaks down at low temperatures.In order to alleviate this problem, an extended version of this approach that includes vertex correction has been suggested.

The non-perturbative approach provides numerically exact calculation and applicable in a wide range of parameters. Its main drawback is the computational costs which limits the temperature, bath size and time slices. One of the most powerful methods is the quantum monte carlo (QMC) based on the algorithm of Hirsch and Fye[47]. This approach offers an accurate solution of the single- and the two-particle Green's function in a wide range of coupling and is also applicable even at low temperatures. Note however that lowering the temperature amounts to an increase in the time slices and thus also to more computational effort. The shortcomings of the method are the unpredictable sign problem away from half-filling and very low temperature and the fact that the output Green's function in terms of the imaginary time/frequency. The latter becomes problematic in the case of calculating the dynamical properties e.g the spectral function. In this respect, one requires additional methods that are capable of transforming the data of the imaginary time/frequency into that in real frequency. The most widely used approach is maximum entropy method which will be also discussed in the next section. Recently a new QMC algorithm has been developed which is based on the idea of continuous time slices and thus it is free from Trotter errors [53, 54]. It is shown that this method known as continuous time quantum monte carlo (CTQMC) in combination with DMFT captures the metal insulator transition and also gives reasonable results at low temperature. Another advantage is that it allows one to consider the multiband problems with off-diagonal exchange. The method is, however, plagued by negative sign problems which occur with the same probability as in the case of the Hirsch-Fye method. The universal impurity solver that works efficiently and at the same time produce accurate results in all regimes of parameters is not available at present.

All results of DMFT or EDMFT for the Hubbard model in the presented works were obtained with quantum monte carlo method that follows Hirsch and Fye [47] algorithm. In this section we will outline the derivation of QMC equations for single band case. Extension into orbitally degenerate case and fermion-boson systems will be discussed afterwards.

The first step of the algorithm is to discretize the imaginary time into N time slices

$\tau_i, i = 1, 2 \ldots N$ of size $\Delta\tau = \frac{\beta}{N}$. This is followed by Trotter decomposition that decouples the interacting and non-interacting part of the Hamiltonian as

$$Z = \mathrm{Tr} \prod_{\mathrm{n=1}}^{\mathrm{N}} \mathrm{e}^{-\Delta\tau(\mathrm{H}_0+\mathrm{H}_1)} \approx \mathrm{Tr} \prod_{\mathrm{n=1}}^{\mathrm{N}} \mathrm{e}^{-\Delta\tau \mathrm{H}_0} \mathrm{e}^{-\Delta\tau \mathrm{H}_1}. \tag{2.84}$$

The quadratic term in the Hamiltonian can be decoupled by using discrete Hubbard-Stratonovich transformation at the expense of introducing auxiliary field, Ising like variables taking values ± 1. One then obtains

$$e^{\Delta\tau U n_\uparrow n_\downarrow = \frac{1}{2}\sum_{S=\pm 1} e^{\lambda S(n_\uparrow - n_\downarrow)}} \tag{2.85}$$

where $\cosh(\lambda) \equiv e^{\Delta\tau U/2}$. Substituting equation (2.85) into the partition function in equation (2.84) gives

$$Z^{\Delta\tau} = \frac{1}{2^N} \sum_{S_1,\ldots,S_N=\pm 1} Z^{\Delta\tau}_{S_1,\ldots,S_N} \tag{2.86}$$

where

$$Z^{\Delta\tau}_{S_1,\ldots,S_N} = \prod_{\sigma=\pm 1} \mathrm{Tr}\left[\mathrm{e}^{-\Delta\tau \mathrm{H}_0} \mathrm{e}^{\mathrm{V}^\sigma(\mathrm{S}_1)} \mathrm{e}^{-\Delta\tau \mathrm{H}_0} \mathrm{e}^{\mathrm{V}^\sigma(\mathrm{S}_2)} \ldots \mathrm{e}^{-\Delta\tau \mathrm{H}_0} \mathrm{e}^{\mathrm{V}^\sigma(\mathrm{S}_\mathrm{N})}\right] \tag{2.87}$$

It is important to note here that the size of the conduction bath orbitals are numbered from $m = 1, \ldots, N_b$ and impurity orbital corresponds to $m = 1$. Explicit expressions of the diagonal matrix $V^\sigma(S)$ of the size $N_b \times N_b$ reads

$$V^\sigma(S) = \begin{pmatrix} e^{\lambda\sigma S} & 0 & . & . & . & 0 \\ 0 & 1 & 0 & . & . & 0 \\ 0 & 0 & 1 & 0 & . & 0 \\ . & . & . & . & . & . \\ 0 & . & . & . & 0 & 1 \end{pmatrix}. \tag{2.88}$$

The partition function (2.84) can be written in the form of a determinant matrix following the identity $\mathrm{Tr}\left[e^{-\sum_{ij} c_i^\dagger [A_{ij}+B_{ij}+C_{ij}] c_j}\right] \equiv \det[1 + e^{-(A+B+C)}]$. Thus the partition function reads

$$Z^{\Delta\tau}_{S_1,\ldots,S_N} = \det[O^\sigma_{S_1,\ldots,S_N}], \tag{2.89}$$

$$= \det[1 + B^\sigma(S_N) B^\sigma(S_{N-1}) \ldots B(S_1)^\sigma], \tag{2.90}$$

where $B^\sigma(S) \equiv e^{-\Delta\tau H_0} e^{V^\sigma(S)}$. Using a simple algebra, matrix $O^\sigma_{S_1,\ldots,S_N}$ which is $N \times N$ matrix of $N_b \times N_b$ is explicitly written as

$$O^\sigma_{S_1,\ldots,S_N} = \begin{pmatrix} 1 & 0 & . & . & 0 & B^\sigma(S_1) \\ -B^\sigma(S_2) & 1 & 0 & . & . & 0 \\ 0 & -B^\sigma(S_3) & 1 & . & . & 0 \\ . & 0 & -B^\sigma(S_4) & . & . & . \\ . & . & 0 & . & . & . \\ . & . & . & . & . & . \\ 0 & . & . & 0 & -B^\sigma(S_N) & 1 \end{pmatrix}. \tag{2.91}$$

An important identity in the quantum monte carlo algorithm is that the matrix $O^{\sigma}_{S_1,\ldots,S_N}$ is related to the Green's function by

$$g^{\Delta\tau}_{S_1,\ldots,S_N} = [O^{\sigma}_{S_1,\ldots,S_N}]^{-1}. \tag{2.92}$$

The relation between the Green's function with two different Ising spin configuration $S_1,\ldots,S_N$ and $S'_1,\ldots,S'_N$ is related to the Dyson like equation. To show this formula, one considers the following equation

$$\widetilde{O} = e^{-V} O. \tag{2.93}$$

Using Eq.(2.92), one then obtains

$$\widetilde{g} \equiv \widetilde{O}^{-1} \tag{2.94}$$

$$= \left[\widetilde{O}' + \underbrace{\widetilde{O} - \widetilde{O}'}_{e^{-V}-e^{-V'}}\right]^{-1} \tag{2.95}$$

$$= \widetilde{g}' - \widetilde{g}'(e^{-V} - e^{-V'})\widetilde{g}. \tag{2.96}$$

The last equation is derived by making use of the identity $\frac{1}{A+B} = \frac{1}{A} - \frac{B}{A(A+B)}$. Substituting $\widetilde{g} = ge^{V}$, leads to the expected Dyson equation

$$g' = g + (g-1)(e^{V'-V} - 1)g', \tag{2.97}$$

where $g \equiv g^{\Delta\tau}_{S_1,\ldots,S_N}$ and $g' \equiv g^{\Delta\tau}_{S'_1,\ldots,S'_N}$. The above Dyson equation holds even after integrating out the conduction bath and considering only the impurity site. Based on this observation one can then express eq.(2.97) for impurity problem as follows

$$G' = G + (G-1)(e^{V'-V} - 1)G', \tag{2.98}$$

with $G \equiv G^{\Delta\tau}_{S_1,\ldots,S_N}$ is now a matrix of the size $N \times N$.

The most efficient way to sum large number of possible configuration such as expressed in the partition function of Eq.(2.89) is achieved by means of monte carlo procedure. In this respect, one of the most important issue to be considered is the dynamics of monte carlo method which generally can be chosen arbitrarily as long as it satisfies the detailed balance condition explicitly written as follows

$$\frac{P(s \to s')}{P(s' \to s)} = \frac{\prod_\sigma \det \mathcal{O}(\sigma)_{s'}}{\prod_\sigma \det \mathcal{O}(\sigma)_{s}}. \tag{2.99}$$

The heat bath and the Metropolis algorithm satisfy the above condition. Thus, within Metropolis, the acceptance probability at the n-th imaginary time slice reads

$$R = \prod_\sigma \frac{\det[G_\sigma]}{\det[G'_\sigma]} \tag{2.100}$$

$$= 1 + (1 - G_{\sigma n,n})\,[e^{V'_l - V_l} - 1]. \tag{2.101}$$

If the move is accepted then the new impurity Green's function is upgraded using the relation

$$G'_{\sigma i,j} = G_{\sigma i,j} + \frac{\Delta V(G_{\sigma i,n} - \delta_{i,n})G_{\sigma n,j}}{1 + (1 - G_{\sigma n,n})\Delta V}, \tag{2.102}$$

where $\Delta V = e^{V'^{\sigma} - V^{\sigma}} - 1$.

For an orbitally degenerate model [55, 48], the formula described above has to be slightly modified. In this case, the total number of auxiliary fields depends on the number of orbital degeneracy. The relation between matrix O_m and Green's function is again written as $G_m = O_m^{-1}$. Straightforwardly, the Dyson formula for degenerate system can be expressed as

$$G'_m = G_m + (G_m - I)(e^{(V^m)' - V^m} - I)G'_m. \tag{2.103}$$

The index m takes account for orbital and spin degrees of freedom. The Boltzmann ratio of Eq.(2.100) now also depends on the number of orbitals

$$R = \prod_m \frac{\det(G_m)}{\det(G'_m)} = \det\left[I - (G_m - I)(e^{(V^m)' - V^m} - I)\right]. \tag{2.104}$$

When the move is accepted, the updated Green's function in the multiband case can be again expressed in the manner similar to that described above for single band.

In the fermion-boson system, one can again perform the somewhat similar steps as described above. In this respect, the partition function with the Hamiltonian of Eq.(2.4) or equivalently the action of Eq.(2.79) can be evaluated straightforwardly by performing a Gaussian integration of the Grassmann variables which leads to final expression as follows [56, 57]

$$Z^{\Delta\tau}_{S_1,\ldots,S_N;\phi_1,\ldots,\phi_N} = \det[O^{\sigma}_{S_1,\ldots,S_N;\phi_1,\ldots,\phi_N}]e^{B}. \tag{2.105}$$

where $B(\phi_{\nu n}) = \sum_{i=1}^{N} \phi_{\nu i}\chi^{-1}_{0\nu in}\phi_{\nu n}$ is the bosonic contribution with $\phi_{\nu n}$ being the bosonic field and $\chi_{0\nu in} = \chi_{0\nu}(\tau_i - \tau_l)$ is the propagator expressed in Eq.(2.80) . In the above equation, index $\alpha(\nu)$ stands for the degrees of freedom of fermions(bosons). Following the same expression given above, the probability to obtain the new state $(S'_n, \phi\prime_n)$ from the initial state (S_n, ϕ_n) reads

$$R = \prod_{\alpha} \frac{\det G_{\alpha} e^{-\Delta\tau B(\phi'_{\nu n})}}{\det G'_{\alpha} e^{-\Delta\tau B(\phi_{\nu n})}}. \tag{2.106}$$

In the implementation of the algorithm, the changes of bosonic field at each discretized time slices is performed by using the relation $\phi'_{\nu n} = \phi'_{\nu n} + r\delta$, where r is a random number between -1 and 1, and δ is the given amplitude so as to obtain the desired acceptance. For the accepted move due to spin flip, the Green's function is again updated via Eq.(2.102). Similarly when the boson is changed at nth time slices then the Green's function is updated via Dyson equation that is similar to the one in Eq.(2.102). In this case, however, ΔV incorporates the bosonic field.

2.6 Maximum Entropy

The Hirsch-Fye QMC method generates the Green's function defined on the imaginary time $G(\tau)$ or equivalently on Matsubara frequency points $G(i\omega_n)$. The relation between the imaginary-time Green's function and real-frequency quantity such as the spectral function $A(\omega)$ is expressed as

$$G(\tau) = \int d\omega K(\tau, \omega) A(\omega), \tag{2.107}$$

where the kernel $K(\tau, \omega)$ for $(+)$ fermion and $(-)$ boson reads

$$K(\tau, \omega) = \frac{e^{-\tau\omega}}{1 \pm e^{-\beta\omega}}. \tag{2.108}$$

It is easy to realize that the solution of $A(\omega)$ from this kind of integral can obtained by performing direct inversion method. This approach however becomes problematic in this respect and could lead to unphysical results. The primary reason is that the kernel becomes insensitive for large frequencies and thus there are many possible values of $A(\omega)$ that correspond to the same data of imaginary time. In addition, the problem is also exacerbated by the fact that QMC data are also noisy and incomplete particularly for the case of two particle Green's function. The most widely used approach for solving the inverse problems as in the Eq.(2.107) is the Bayesian-based maximum entropy method [58]. Within Bayesian statistical inference, one defines the posterior probability or probability of the solution $A(\omega)$ given the data $G(\tau)$ and the prior information about A. The maximum entropy provides a way to determine the most probable solution of A based on this set of data. It can be shown that the posterior probability has the form

$$P(A|G, m, \alpha) = \frac{\exp(\alpha S - \chi^2/2)}{Z_s Z_L}, \tag{2.109}$$

where Z_s and Z_L are normalization factors that are independent of A. α is a regularization parameter and S is the Shannon-Jaynes entropy

$$S = \sum_{\omega} \left[A(\omega) - m(\omega) - A(\omega) \ln \left(\frac{A(\omega)}{m(\omega)} \right) \right]. \tag{2.110}$$

This entropy is measured according to the default model $m(\omega)$ that contains prior information about A. The other quantity in the exponential of Eq.(2.109), χ^2 denotes the least square difference between the data G with standard errors $\sigma(\tau)$ and the constructed data $\int d\omega K(\tau) A(\omega)$ obtained using the trial input of A. Explicitly this is written as

$$\chi^2 = \sum_{\tau} \left[\frac{G(\tau) - \int d\omega K(\tau, \omega) A(\omega)}{\sigma(\tau)} \right]. \tag{2.111}$$

In the absence of data, the solution of A that maximizes the posterior probability is therefore the one that maximizes the entropy S. Similarly, for fixed α the most probable solution of A is the one that maximizes $Q = \alpha S - \chi^2/2$ namely by solving $\nabla Q = 0$ with respect to A. The most

common way to solve this equation is by employing the Newton-Raphson method. Since the size of the search space is typically very large, the most efficient way to reduce the search dimension is by employing the algorithm of Bryan [59]. In this scheme, the reduced space is equal to the largest possible number of eigenvalue of K obtained from the singular value decomposition (SVD). Practical application of this algorithm and additional issues such as the choice of the regularization parameter α and the model $m(\omega)$ can be found in the review of Ref.[58]. The dynamic of the single and the two particle Green's function presented in this work is obtained with maximum entropy method based on the Bryan algorithm.

CHAPTER 3

Two-Particle Excitation

3.1 Introduction

The knowledge of the single-particle spectrum is the key to understand the properties of solid. In order to understand the transport properties e.g. the optical conductivity, the dielectric function, the thermoelectrics one should go beyond single-particle quantities. In terms of Green's function, one resorts to higher *n*-point Green's functions namely, the two-particle Green's function. It may be classified in general into those associated with the particle-hole and the particle-particle channels. Different techniques are appropriate to access each of these channels.

Perhaps, the most studied one of them is the particle-hole channel relevant to a number of material properties such as the optical response, the dielectric and the magnetic susceptibility. With the rapid development of experimental tools one can now probe accurately the transport properties. Several techniques for this purpose have been employed such as the optical spectroscopy, the inelastic neutron scattering (INS), the raman spectroscopy, the electron energy loss spectroscopy (EELS). The particle-particle or hole-hole channels have been much discussed in connection with the Auger electron spectroscopy (AES) and the appearance potential spectroscopy (APS). The recently introduced two-particle technique so-called double photoemission (DPE) or $(\gamma, 2e)$ is expected to provide a new direction in the study of particle-particle excitation

3.2 Optical Conductivity

The frequency-dependent optical conductivity is an important probe of electronic degrees of freedom that yields various quantities such as the electronic band gaps, scattering processes, effective carriers[60]. This quantity has become increasingly important during the last decade in particularly for strongly correlated systems that show unusual optical characteristics. In order to measure the optical response as a function of frequency, there are three different approaches that

are commonly used. In the first method, a sample is exposed to monochromatic radiation. The amplitude and the phase of response are measured at single frequency ω. This might be the resistance and the capacitance, the complex reflection coefficient, or the amplitude drop and phase shift upon transmission. The problems of relating the dielectric function or the optical conductivity with the measured quantity boils down to solving the Maxwell equations. The next two approaches use, instead of monochromatic radiation, an excitation with a well-defined time or spectral dependence and therefore are capable of determining the response over a wide frequency range. The radiation wavelength used in the experiments for almost all cases is relatively large in comparison with any length scale in solids. In this way, the momentum dependence in the optical conductivity can be set as $\mathbf{q} \to 0$. In addition to that the magnitude of the perturbing field has to be small enough such that the signal is linearly proportional to the external perturbation.

The microscopic description of the optical excitation in solids has been formulated by Kubo [61]. In what follows we shall first derive the expression for optical conductivity in the continuum case and then discuss the formulation in the lattice system. The optical conductivity $\sigma_{ab}(\mathbf{q},\omega)$ determines the induced current $\mathbf{J}_a(\mathbf{q},\omega)$ upon an applied transversal electric field $\mathbf{E}_b(\mathbf{q},\omega)$ (Ohm's law)

$$\mathbf{J}_a(\mathbf{q},\omega) = \sigma_{ab}(\mathbf{q},\omega)\mathbf{E}_b(\mathbf{q},\omega). \tag{3.1}$$

Expressed in terms of field operators, the Hamiltonian reads

$$H = \int d^3r \frac{1}{2m}\left[\left(\nabla - \frac{ie}{c}\mathbf{A}\right)\psi(\mathbf{r})\right]^2 + H_{int}. \tag{3.2}$$

where $\psi(\mathbf{r})$ is the electron field operator, m is the mass of the electron and the H_{int} designates all possible interactions in the solid. In the Coulomb gauge, the relation of electric field and vector potential is given by $\mathbf{A}(\mathbf{r},t) = \frac{\mathbf{E}(\mathbf{r},t)c}{i\omega}$. The total current $\mathscr{J}(\mathbf{r})$ in the presence of the vector potential $\mathbf{A}$ can be straightforwardly obtained by taking the derivative of the Hamiltonian with respect to $\mathbf{A}$ which then leads to

$$\mathscr{J}(\mathbf{r}) = \frac{-ie}{2m}[\psi^\dagger(\mathbf{r})\nabla\psi(\mathbf{r}) - (\nabla\psi^\dagger(\mathbf{r}))\psi(\mathbf{r}) - \frac{e^2}{mc}\mathbf{A}\psi^\dagger(\mathbf{r})\psi(\mathbf{r}). \tag{3.3}$$

The next step is to take the average of the total current $\mathscr{J}(\mathbf{r})$ which is equivalent to the current of Eq.(3.1). In doing so, we recall that in the perturbation theory, the ensemble average of any operator $\mathcal{O}$ in the presence of the vector potential can be expressed as

$$\langle\mathcal{O}(\mathbf{r},t)\rangle = \langle\mathcal{O}_H(\mathbf{r},t)\rangle - i\int_{-\infty}^{t} dt' \left\langle\left[\mathcal{O}_H(\mathbf{r},t), H_A(t')\right]\right\rangle, \tag{3.4}$$

where $\mathcal{O}_H(\mathbf{r},t)$ is the operator in the Heisenberg picture and the H_A is the part of Hamiltonian that contains the vector potential $\mathbf{A}$ in linear order. The average sign in the right hand side corresponds to the average of the interacting but unperturbed system. A combination of Eq.(3.3)

and Eq.(3.4) gives

$$\mathbf{J}(\mathbf{r},t) \equiv \langle \mathscr{J}(\mathbf{r},t)\rangle = -\frac{e^2}{mc}\mathbf{A}(\mathbf{r},t)\left\langle \psi^\dagger(\mathbf{r},t)\psi(\mathbf{r},t)\right\rangle + \frac{i}{c}\int_{-\infty}^{t} dt' \int d^3r' \left\langle \left[j_0(\mathbf{r},t), j_0(\mathbf{r}',t').\mathbf{A}(\mathbf{r}',t')\right]\right\rangle, \tag{3.5}$$

where j_0 corresponds to the current operator for $\mathbf{A} = 0$. Fourier transforming into the momentum space and comparing with (3.1) yields the well-known Kubo formula for the optical conductivity in the continuum

$$\sigma_{ab}(\mathbf{q},\omega) = \frac{1}{\omega}\int_{-\infty}^{t} dt' e^{i\omega(t-t')}\langle [j_a(\mathbf{q},t), j_b(\mathbf{q},t')]\rangle + \frac{ine^2}{m\omega}\delta_{ab}. \tag{3.6}$$

This formula consists of the paramagnetic and the diamagnetic terms where the former is denoted by the current-current correlation function that contains many body interactions. The optical conductivity is obtained by solving the two-particle correlation function which can be done most conveniently in the Matsubara formalism

$$\Pi_{ab}(\mathbf{q}, i\omega_m) = \int_0^\beta d\tau e^{i\omega_m\tau}\langle T_\tau j_a(\mathbf{q},\tau) j_b(\mathbf{q},0)\rangle \tag{3.7}$$

where ω_m are bosonic Matsubara frequencies.

In the case of a lattice system e.g. the Hubbard model of Eq.(2.1), one can also derive a Kubo formula similar to the one in equation (3.6) [62]. By adopting the so called *Peierls ansatz*, the vector potential $\mathbf{A}$ enters the Hamiltonian by performing a substitution $c_i^\dagger \to c_i^\dagger e^{ie\int \mathbf{A}.d\mathbf{r}}$. It can be shown that the interaction term of the Hubbard model consisting of the density-density interaction is gauge invariant. On the other hand the kinetic energy now contains the vector potential thus suggesting that the optical processes arise from the electron that move from one site to another. Substituting the creation/annihilation operator with *Peierls ansatz* into Eq.(2.1) and expanding up to second order in $\mathbf{A}$ leads to

$$H = H_0 - \sum_{\mathbf{r}x}\left[e\mathbf{A}_x(\mathbf{r},t)j_x(\mathbf{r}) - \frac{e^2}{2}\mathbf{A}_x^2(\mathbf{r},t)K_x(\mathbf{r})\right] \tag{3.8}$$

where H_0 stands for the kinetic energy part of the Hamiltonian Eq.(2.1), $ej_x(\mathbf{r})$ is the x component of paramagnetic current density

$$j_x(\mathbf{r}) = it\sum_\sigma c^\dagger_{\mathbf{r}\sigma}c_{\mathbf{r}+x\sigma} - c^\dagger_{\mathbf{r}+x\sigma}c_{\mathbf{r}\sigma} \tag{3.9}$$

or in the momentum space

$$j(\mathbf{q}) = \sum_{\mathbf{k}\sigma}\mathbf{v}(\mathbf{k})c^\dagger_\sigma(\mathbf{k}-\mathbf{q})c_\sigma(\mathbf{k}+\mathbf{q}) \tag{3.10}$$

where $\mathbf{v}(\mathbf{k}) = \nabla\epsilon(\mathbf{k})$. The last term of Eq.(3.8) $K_x(\mathbf{r})$ is the kinetic part expressed as

$$K_x(\mathbf{r}) = -t\sum_\sigma c^\dagger_{\mathbf{r}\sigma}c_{\mathbf{r}+x\sigma} + c^\dagger_{\mathbf{r}+x\sigma}c_{\mathbf{r}\sigma}. \tag{3.11}$$

The total current density is then obtained by evaluating the first derivative of equation (3.11) with respect to $\mathbf{A}$

$$\mathscr{J}_x(\mathbf{r},t) = ej_x(\mathbf{r}) + e^2 K_x(\mathbf{r})\mathbf{A}_x(\mathbf{r},t). \tag{3.12}$$

Following the same steps as in the continuum case and transforming into the momentum domain one obtains the current density for the lattice system that consists of the usual diamagnetic and paramagnetic terms

$$\mathbf{J}_x(\mathbf{q},\omega) = e^2\left[\langle K_x\rangle + \Pi_{xx}(\mathbf{q},\omega)\right]\mathbf{A}_x(\mathbf{q},\omega). \tag{3.13}$$

Comparing with Eq.(3.1) one finds the optical conductivity that consists of a paramagnetic term or the two-particle correlation function which can be evaluated in the Matsubara formalism following Eq.(3.7). Explicitly, the current-current correlation function is then obtained by substituting Eq.(3.10) into Eq.(3.7) as follows

$$\Pi(i\omega_m) = \int_0^\beta d\tau e^{i\omega_m\tau}\sum_{\sigma\sigma'}\sum_{\mathbf{k}\mathbf{k}'}\mathbf{v}(\mathbf{k})\mathbf{v}(\mathbf{k}')\left\langle T_\tau c^\dagger_\sigma(\mathbf{k},\tau)c_\sigma(\mathbf{k},\tau)c^\dagger_{\sigma'}(\mathbf{k}')c_{\sigma'}(\mathbf{k}')\right\rangle \tag{3.14}$$

where the momentum dependence $\mathbf{q}$ in the above equation has been discarded following the argument mentioned before. The evaluation of the two-particle propagator can be done via the diagrammatic expansion. In this respect one has to deal with an expression similar to the one in Eq.(2.39) in the particle-hole sector. The limit of infinite dimension offers a great simplification in that only the first order survives while higher order vertex corrections vanish due to the different parity [63]. This simplification leads to the expression of the optical conductivity that consists of the bubble diagram only

$$\sigma(i\omega_m) = \frac{1}{\omega}\sum_{\mathbf{k},\sigma,i\nu_n}\mathbf{v}^2(\mathbf{k})\mathcal{G}_\sigma(\mathbf{k},i\nu_n)\mathcal{G}_\sigma(\mathbf{k},i\nu_n+i\omega_m) \tag{3.15}$$

where $\mathcal{G}(\mathbf{k},i\nu_n)$ is the full single-particle Green's function with the DMFT self energy. By evaluating the Matsubara summation which is ensued by an analytical continuation of the frequency one arrives at the expression of the optical conductivity in the infinite coordination limit [64]

$$\sigma_1(\omega) = \mathscr{C}_0\int d\epsilon\rho_0(\epsilon)\int d\nu A(\epsilon,\nu)A(\epsilon,\nu+\omega)\frac{f(\nu)-f(\nu+\omega)}{\omega} \tag{3.16}$$

where $A(\epsilon,\nu)$ is the single-particle spectral function, $f(\nu)$ is the Fermi function and $\mathscr{C}_0$ is the constant that incorporates various factors including the constants from the summation of spin and

$$\rho_0(\epsilon) = \sum_{\mathbf{k}}\mathbf{v}^2(\mathbf{k})\delta(\epsilon-\epsilon(\mathbf{k})) \tag{3.17}$$

is the factor of the lattice structure. It is important to note that the above equation is only the real part of the total optical conductivity expressed as $\sigma(\omega) = \sigma_1(\omega) + i\sigma_2(\omega)$. Once one of this quantity is known, the other part can be calculated via the Kramers-Kronig relation

$$\sigma_1(\omega) = \frac{1}{\pi}\int_{-\infty}^{\infty}\frac{\sigma_2(\nu)}{\nu-\omega}d\nu. \tag{3.18}$$

The optical constant obeys various sum rules. The most frequently used is the the well-known f-sum rule that relates the integrated optical spectra and the number of particles reads

$$\int_0^\infty \sigma_1(\omega)d\omega = \frac{\omega_p^2}{8} = \frac{\pi n e^2}{2m_0}, \tag{3.19}$$

where ω_p stands for plasma frequency, n is the carrier density and m_0 denotes the free electron mass. Within the $d \to \infty$ approximation, the sum rules takes the form

$$\int_0^\infty \sigma_1(\omega)d\omega = \mathscr{C}_0 \left\langle \frac{\rho'(\epsilon)}{D(\epsilon)} \right\rangle, \tag{3.20}$$

where $\rho'(\epsilon) = \frac{d}{d\epsilon}\rho_0(\epsilon)$ and $D(\epsilon)$ is the non-interacting DOS. In practice however, one relies mostly on the frequency-dependent spectral weight expressed as follows

$$K(\Omega) = \int_0^\Omega \sigma_1(\omega)d\omega. \tag{3.21}$$

For a detailed discussion on the optical conductivity in the single band Hubbard model within DMFT, we refer to Ref.[30].

Derivation of the optical conductivity in the antiferromagnetically ordered phase basically follows the same lines as in the paramagnetic phase. However in the present case, one has to deal with the kinetic energy that consists of two different species of operators $a^\dagger(a)$ and $b^\dagger(b)$ that correspond to the creation (annihilation) operators in the sublattice A and B respectively [61, 65]. Rewriting the kinetic energy of Eq.(2.67) in terms of a, b and hopping amplitude t one obtains

$$H = -t \sum_{ij\sigma} \left(a_{i\sigma}^\dagger b_{j\sigma} + b_{j\sigma}^\dagger a_{i\sigma} \right) \tag{3.22}$$

or in the momentum phase

$$H = \sum_{\mathbf{k}\sigma} \Psi_\sigma^\dagger(\mathbf{k}) \begin{pmatrix} 0 & \epsilon(\mathbf{k}) \\ \epsilon(\mathbf{k}) & 0 \end{pmatrix} \Psi_\sigma(\mathbf{k}), \tag{3.23}$$

with $\Psi_\sigma^\dagger(\mathbf{k})$ and $\Psi_\sigma(\mathbf{k})$ are the spinors

$$\begin{aligned} \Psi_\sigma^\dagger(\mathbf{k}) &= (a_\sigma^\dagger(\mathbf{k}), b_\sigma^\dagger(\mathbf{k})), \\ \Psi_\sigma(\mathbf{k}) &= (a_\sigma(\mathbf{k}), b_\sigma(\mathbf{k})). \end{aligned} \tag{3.24}$$

Similar as before, the current operator is related to the group velocity $\mathbf{v}$ and the density which in this context is replaced by spinor. This is written as follows

$$j = e \sum_{\mathbf{k}\sigma} \Psi_\sigma^\dagger(\mathbf{k}) \begin{pmatrix} 0 & \mathbf{v}(\mathbf{k}) \\ \mathbf{v}(\mathbf{k}) & 0 \end{pmatrix} \Psi_\sigma(\mathbf{k}). \tag{3.25}$$

Following the line as described before in the paramagnetic phase, the current-current correlation function reads

$$\begin{aligned} \Pi(i\omega_m) = \int_0^\beta d\tau e^{i\omega_m \tau} \sum_{\sigma,\sigma'} \sum_{\mathbf{k}\mathbf{k}'} \mathbf{v}(\mathbf{k})\mathbf{v}(\mathbf{k}') \Big\langle T_\tau \left[a_\sigma^\dagger(\mathbf{k},\tau) b_\sigma(\mathbf{k},\tau) + b_\sigma^\dagger(\mathbf{k},\tau) a_\sigma(\mathbf{k},\tau) \right] \\ \left[a_{\sigma'}^\dagger(\mathbf{k}') b_{\sigma'}(\mathbf{k}') + b_{\sigma'}^\dagger(\mathbf{k}') a_{\sigma'}(\mathbf{k}') \right] \Big\rangle . \end{aligned} \tag{3.26}$$

By using the approximation in the limit of infinite dimensions, one deals again with first order contributions. After some straightforward algebra and Fourier transforming into frequency domain, the correlation function in terms of the single-particle Green's function reads

$$\sum_{\mathbf{k},i\nu_n\sigma,} \mathbf{v}^2(\mathbf{k}) \left[\mathcal{G}_\sigma^{AA}(\mathbf{k},i\nu_n+i\omega_m)\mathcal{G}_\sigma^{BB}(\mathbf{k},i\nu_n)+\mathcal{G}_\sigma^{AA}(\mathbf{k},i\nu_n)\mathcal{G}_\sigma^{BB}(\mathbf{k},i\nu_n+i\omega_m)\right.$$
$$\left.+\mathcal{G}_\sigma^{AB}(\mathbf{k},i\nu_n+i\omega_m)\mathcal{G}_\sigma^{AB}(\mathbf{k},i\nu_n)+\mathcal{G}_\sigma^{BA}(\mathbf{k},i\nu_n+i\omega_m)\mathcal{G}_\sigma^{BA}(\mathbf{k},i\nu_n)\right], \quad (3.27)$$

where

$$\begin{aligned}\mathcal{G}_\sigma^{AA}(\mathbf{k},i\nu_n) &= \frac{\zeta'_\sigma}{\zeta_\sigma\zeta_{\sigma'}-\epsilon(\mathbf{k})^2}, \\ \mathcal{G}_\sigma^{BB}(\mathbf{k},i\nu_n) &= \frac{\zeta_\sigma}{\zeta_\sigma\zeta_{\sigma'}-\epsilon(\mathbf{k})^2}, \\ \mathcal{G}_\sigma^{AB}(\mathbf{k},i\nu_n) &= \mathcal{G}_\sigma^{BA}(\mathbf{k},i\nu_n) = \frac{\epsilon(\mathbf{k})^2}{\zeta_\sigma\zeta_{\sigma'}-\epsilon(\mathbf{k})^2},\end{aligned} \quad (3.28)$$

are the single-particle Green's function in the sub lattice A and B, $\zeta_\sigma^{A/B}(i\nu_n) = i\nu_n+\mu-\Sigma_\sigma^{A/B}$. In the Neel state, the relation $\zeta_\sigma^A = \zeta_{\sigma'}^B = \zeta_\sigma$ holds. The real part of optical conductivity in the antiferromagnetic phase is obtained by performing the analytical continuation of imaginary frequency and then taking the imaginary part of Green's function which leads to

$$\sigma_1(\omega) = \sum_\sigma \int d\epsilon\rho_0(\epsilon)\int d\nu \frac{f(\nu)-f(\nu+\omega)}{\omega}\left[A_\sigma(\epsilon,\nu)A_{\sigma'}(\epsilon,\nu+\omega)\right.$$
$$\left.+B_\sigma(\epsilon,\nu)B_\sigma(\epsilon,\nu+\omega)\right], \quad (3.29)$$

where $\rho_0(\epsilon)$ is the same as that Eq.(3.17), A and B describe the single-particle spectral function defined by

$$\begin{aligned}A_\sigma(\epsilon,\nu) &= -\frac{1}{\pi}\mathrm{Im}\mathcal{G}_\sigma^{AA}(\epsilon,\nu+i\delta), \\ B_\sigma(\epsilon,\nu) &= -\frac{1}{\pi}\mathrm{Im}\mathcal{G}_\sigma^{AB}(\epsilon,\nu+i\delta)].\end{aligned} \quad (3.30)$$

The generalization of the above formula to the multiband case can be done straightforwardly. One has to deal only with the summation over all orbitals which in the case of DMFT comes from the diagonal terms only.

3.3 Electron Pair Excitation

The particle-particle Green's function is readily calculated within the self-consistency loop of DMFT-QMC. The nature of the approximation however only allows for evaluating the local two-particle Green's function or the so-called onsite *s*-wave pair function. Thus, for other pairing symmetries such as *d*-wave, extended *s*-wave and *p*-wave pairing which are the central quantities in the context of high-T_c cuprates, one should go beyond the DMFT method. The extended

DMFT method that incorporates the non-local interaction via additional terms in the Hamiltonian but at the same time maintains the single site approximation does not provide any advantages in this respect. Nevertheless, the pair Green's function derived from this method already incorporates the influence of the non-local fluctuation that enters from the single-particle self energy and thus its structure should give more information than those obtained by the conventional DMFT method. In the single site approximation, one then evaluates the local two-particle Green's function expressed as

$$\chi_{pp}(\tau) = \left\langle T_\tau \Delta^\dagger(\tau)\Delta(0) \right\rangle, \tag{3.31}$$

where $\Delta = c_\uparrow c_\downarrow$. Since the particle-particle Green's function is obtained in terms of the imaginary time or Matsubara frequencies, one should rely on the maximum entropy to obtain the real frequency spectra.

Performing the calculation for single and two particles simultaneously within the same approximation as described above is certainly of an advantage. The changes in the two-particle Green's function lead to the renormalization of single-particle quantity and vice versa. It is instructive however to pursue other scheme that might be useful as a benchmark of the result of the DMFT+QMC method. The widely used approach to construct the particle-particle Green's function is the ladder approximation. As will be further elaborated in the next section, this scheme has been applied in the study of the two-particle spectroscopy combined with various approximations for the single-particle Green's function. The present section is thus intended to obtain the exact expression for the two-particle Green's function which will be derived in a manner similar to that described in Ref.[66, 67]. Note however that some modifications have been made in order to fit the approximation of the local self energy of DMFT. Starting with the full expression of the two-particle Green's function in the Matsubara representation one has

$$\chi_{pp}(\mathbf{q}, i\omega_m) = \int \langle T_\tau c_{-\sigma}(\mathbf{k},\tau) c_\sigma(\mathbf{q}-\mathbf{k},\tau) c^\dagger_\sigma(\mathbf{q}-\mathbf{p},0) c^\dagger_{-\sigma}(\mathbf{p},0)\rangle, \tag{3.32}$$

with $\int$ is short-hand notation for $-\sum_{\mathbf{k},\sigma}\int_0^\beta d\tau e^{i\omega_m\tau}$ and ω_m is a bosonic Matsubara frequency. This equation is a general expression of the local equation expressed in (3.31). The evaluation of the two-particle propagator may be performed with the aid of the perturbation expansion using the standard diagrammatic theory by selecting the diagrams appropriate for the physical problem at hand. For the Hubbard model with the short-range interaction, one selects the ladder-type diagrams. Summation of ladder diagrams in the particle-particle channel to all orders yields

$$\chi_{pp}(\mathbf{q}, i\omega_m) = -\frac{1}{\beta}\sum_{\mathbf{k}i\nu_n} \mathcal{G}(\mathbf{k}, i\nu_n)\mathcal{G}(\mathbf{q}-\mathbf{k}, i\omega_m - i\nu_n)\Gamma(\mathbf{k},\mathbf{q},i\omega_m). \tag{3.33}$$

Since U is static and independent of the wave vector, the vertex function Γ reads

$$\Gamma(\mathbf{k},\mathbf{q},i\omega_m) = 1 - \frac{U}{\beta}\sum_{\mathbf{p}i\nu'_n} \mathcal{G}(\mathbf{p}, i\nu'_n)\mathcal{G}(\mathbf{q}-\mathbf{p}, i\omega_m - i\nu'_n)\Gamma(\mathbf{p},\mathbf{q},i\nu'_n). \tag{3.34}$$

The right hand side of this relation is independent of $\mathbf{k}$. Thus one obtains

$$\chi_{pp}(\mathbf{q}, i\omega_m) = \frac{\chi(\mathbf{q}, i\omega_m)}{1 - U\chi(\mathbf{q}, i\omega_m)}, \tag{3.35}$$

where

$$\chi(\mathbf{q}, i\omega_m) = -\frac{1}{\beta}\sum_{\mathbf{k}, i\nu_n} \mathcal{G}(\mathbf{k}, i\nu_n)\mathcal{G}(\mathbf{q}-\mathbf{k}, i\omega_m - i\nu_n) \tag{3.36}$$

is the two-particle Green's function expressed in terms of the full single-particle Green's function. Performing standard analytical continuation and evaluating the imaginary part of the two-particle Green's function one arrives at the expression of the two-particle spectral function

$$P(\omega) = \mathrm{Im}[\chi_{\mathrm{pp}}(\omega)]. \tag{3.37}$$

In order to evaluate the above equation, it is sufficient to calculate the imaginary part of the two-particle propagator $\chi(\omega)$, and analytically continue it to real frequencies. This yields

$$\chi_i(\omega) = \mathscr{C}_0 \int_{-\infty}^{\infty} d\nu \int_{-\infty}^{\infty} d\epsilon D(\epsilon) \quad \big[A(\epsilon,\nu)A(-\epsilon,\omega-\nu)\times (1 - f(\nu) - f(\omega-\nu)\big], \tag{3.38}$$

where $\chi_i(\omega)$ stands for the imaginary part of $\chi(\omega)$, $D(\epsilon)$ is free density of states, $A(\epsilon,\omega)$ is the single-particle spectral function with the DMFT self energy and $\mathscr{C}_0$ is a constant. The real part of the two-particle Green's function is obtained via the Kramers-Kronig relation expressed in Eq.(3.18) which follows from the causality condition. It can be shown that the two-particle spectral function obeys the sum rule

$$\int_{-\infty}^{\infty} P(\omega) d\omega = \langle n_\uparrow n_\downarrow \rangle . \tag{3.39}$$

In addition, we note also a useful auxiliary quantity that is related to the partial double occupancy reads

$$K_p(\Omega) = \int_0^{\Omega} d\omega P(\omega). \tag{3.40}$$

In the case of the degenerate Hubbard model that neglects Hund's coupling, it is straightforward to extend the above formulation. In terms of a composite orbital spin index $\alpha = (\alpha, \sigma)$ one writes

$$\chi_{pp}^{\alpha,\alpha'}(\mathbf{q}, i\omega_m) = \frac{\chi^{\alpha,\alpha'}(\mathbf{q}, i\omega_m)}{1 - U\chi^{\alpha,\alpha'}(\mathbf{q}, i\omega_m)}. \tag{3.41}$$

The two-particle propagator $\chi^{\alpha,\alpha'}(\mathbf{q}, i\omega_m)$ reads in this case [68, 67]

$$\chi^{\alpha,\alpha'}(\mathbf{q}, i\omega_m) = -\frac{1}{\beta}\sum_{\mathbf{k}, i\nu_n} \mathcal{G}^{\alpha}(\mathbf{k}, i\nu_n)\mathcal{G}^{\alpha'}(\mathbf{q}-\mathbf{k}, i\omega_m - i\nu_n). \tag{3.42}$$

Straightforwardly, the sum rule in the degenerate case is expressed as follows

$$\int_{-\infty}^{\infty} P(\omega) d\omega = \sum_{\alpha\alpha'} \langle n_\alpha n_{\alpha'} \rangle . \tag{3.43}$$

3.3.1 Survey on Experimental and Theoretical Study of Two-Particle Excitation.

The most notable examples of two-particle spectroscopy are the Auger Electron Spectroscopy (AES) and the Appearance Potential Spectroscopy (APS), intended to probe the occupied and unoccupied states respectively [69]. What lies at the heart of AES and APS techniques is the Auger process characterized by the emission of the Auger electron. In the experiment, the high energy photon beam, sufficient to create the vacancy in the appropriate shell of the atom, bombards the sample material and ejects the single electron. The electron in the outer level fills the shell vacancy with a simultaneous emission of an X-ray quantum or the ejection of an Auger electron. The important difference between these cases is the final state of the system. The former is marked by a single vacancy in the outer shell which, in contrast to Auger process consisting of two vacancies. The kinetic energy of the Auger electron ejected from the atom in the solid is typically 25-3000eV which corresponds to the low effective sampling depth, meaning that the initial state of the Auger electron relatively close to the surface. Thus, the Auger spectroscopy is a surface sensitive method and appropriate for investigating the chemistry of the surface sample.

The technique is also used to investigate the electronic structure of solids. This was initiated by Lander [70], who pointed out that the valence-band Auger spectra is the self convolution of the single electron valence bands. In some cases, the concept of the self-convolution worked relatively well. However, it was later shown by Powell [71] that the core-valence-valence (CVV) line shape of Ag could not be obtained from the self convolution of the occupied states. Further studies on transition metal elements (Cu,Zn,Ga,Ge,As and Se) also showed disagreement with the concept of Lander[72]. Since then the ability of the AES/APS to reproduce the single-particle properties, i.e DOS has been seriously questioned. The need to understand this issue becomes important particularly for correlated systems since it might provide additional information to the single-particle properties. To address this problem, Sawatzky [73] and Cini[72] took the first step to study the behavior of the Auger spectra in the narrow band materials i.e transition metal. In the framework of the Hubbard model, they calculated the two-particle Green's function by means of the ladder approach. This was then combined with the single-particle spectrum obtained from the T-matrix approximation. They pointed out that in the strong coupling interaction regime, the spectra show a strong atomic peak while in the weak coupling the spectra are expected to have a broad band feature that resembles the result of the self convolution. Based on this study, AES/APS spectra were suggested to be able to give insights into the importance of correlation effects.

Theoretical studies on this subject were extended by several authors with different levels of approximations for the single-particle states as well as the two-particle states. Treglia et al. [74] calculated the single-particle properties by employing a second-order Coulomb interaction perturbation with an additional "local approximation" to simplify the calculation. The two-particle propagator on the other hand was calculated within ladder approach. Drchal and Kudrnovsky [75, 76] employed the self consistent T-Matrix approximation for the single-particle level in

combination with the ladder approximation for the two-particle propagator. In a series of works, Nolting and coworkers [66, 77, 68] utilized a simplified single-particle DOS namely B-Steeple DOS which mimics the satellite or the band like behavior. He coined the terms *direct* and *indirect* interaction to distinguish the influence of correlation on the single- and on the two-particle level. The former indicates the interaction between two excited electron or holes, while the latter is subsumed in the single-particle self energy that renormalizes the interacting Green's function. Despite being extensively studied for 30 years or so, there is no general consensus on what the actual advantages of AES and APS in elucidating the electronic structure of solids.

Other experimental techniques of interests in the context of two-particle are (γ,2e) and (e,2e) that allow to directly map the energy and the momentum of the electrons in solids [78, 79, 80]. These relatively new technique in the solid state physics were originally developed to investigate the electronic structure of atoms and molecules. In the experiments, the primary electron with an energy scale approximately 10-50 keV impinges onto the target surface and knocks out a pair of electrons that subsequently emerge on the opposite side of the surface that does not contain the incident beam. The excited electrons with the energy (momentum) $E_1, E_2(\mathbf{k}_1, \mathbf{k}_2)$ are counted only if they are detected coincidently. This ensures that both electrons originate from the same scattering event. Thus the electron with the binding energy ω and momentum $\mathbf{k}$ can be obtained by means of the energy and the momentum conservation as [81, 78, 82]

$$\omega = E_0 - E_1 - E_2, \tag{3.44}$$

$$\mathbf{k} = \mathbf{k}_1 + \mathbf{k}_2 - \mathbf{k}_0 \tag{3.45}$$

where E_0, $\mathbf{k}_0$, are the well-defined energy and momentum of the incident electron. Within this high energy (e,2e) experiments, it has been demonstrated that the measured photocurrent is related to the single-particle spectral function [83, 84]

$$J = (2\pi)^4 \frac{k_1 k_2}{k_0} f_{ee} A(\mathbf{k}, \omega), \tag{3.46}$$

where $f_{ee} = \left(\frac{d\sigma}{d\Omega}\right)$ is the Mott scattering cross-section that includes the effects of exchange between colliding electrons and $\mathrm{A}(\mathbf{k}, \omega)$ is the single-particle spectral function. Early (e,2e) spectrometer has an energy resolution within the range of 90-150 eV, thus inadequate for studying any valence bands of solid. It took almost two decades to reduce the resolution down to $\approx$ 6eV where some of the valence band structure of amorphorous carbon could be resolved. Development of the experimental setup by the addition of an electron monochromator [85] has improved the resolution of energy as well as of the momentum to 0.9-1.5eV and 0.1a.u respectively. To date, this high energy spectroscopy has been applied to variety of solid material e.g. Al, Cu and also vanadium sesquixoide (V_2O_3) in the metallic phase. For the vanadium compound the experimental spectra are in a good agreement with that obtained from band structure calculations using FP-LMTO (Full Potential Linear Muffin-Tin Orbital) [86]. The new (e,2e) experimental set-up uses low energy-incident electron $\approx$ 300eV and it is operated in reflection mode[87]. In

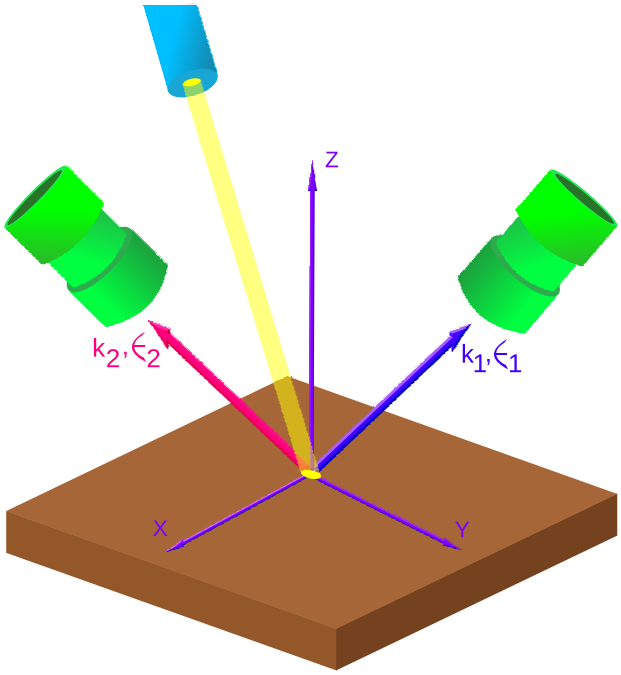

Figure 3.1: A schematics of the one-photon, two-electron (γ,2e) experiment. Upon the absorption of a VUV photon with an energy ν two electrons are excited into the vacuum and simultaneously detected at the energies $\varepsilon_1, \varepsilon_2$ and the momenta $\mathbf{k}_1, \mathbf{k}_2$.

this case, one does not require very thin samples $\approx 200\mathring{A}$ as usually needed in the high energy experiment.

The other type of coincidence spectroscopy is $(\gamma, 2e)$ which is schematically shown in Fig.3.1. These experiments are conducted in the regime where the radiation field is well described classically and the time-dependent perturbation theory in the light-matter interaction and the dipole approximations are well justified (low photon density and low photon frequency $\approx$ 50 eV). In terms of the energy of the two emitted electrons ε_1 and ε_2, the energy conservation law is

$$\hbar\nu - \omega = \varepsilon_1 + \varepsilon_2 + 2\phi \tag{3.47}$$

where ϕ is the work function, ω the initial (correlated) two-particle energy. Application of this technique to study the pair of electrons of the valence bands was first reported by Herrmann et al. [88] for clean Ni(001) and Cu(001) crystals. In the spirit of the single-particle photoemission as described by Caroli [89], the photocurrent of double photoemission (DPE) or $(\gamma, 2e)$ is written as [90, 91]

$$J \propto \int d\epsilon \left\langle \Psi^{(2)} \left| \Delta_2 A(\epsilon) A(E-\omega-\epsilon) \Delta_2^\dagger \right| \Psi^{(2)} \right\rangle \tag{3.48}$$

where $\left|\Psi^{(2)}\right\rangle$ stands for the correlated two-particle states, $E = E_1 + E_2$ is the kinetic energy of the outgoing electron pair with the momentum as defined above and $A(\epsilon)$ is the single-particle spectral function. The essential point is that the operator Δ_N for the photon-charge coupling is of a single-particle nature, i.e. $\Delta_N \propto \sum_{i=1}^{N} \mathbf{A}(\mathbf{r}_i).\hat{\mathbf{p}}_i$ where $\mathbf{A}$ is the vector potential and

$\hat{\mathbf{p}}_i$ is the momentum operator of the particle i. This means Δ_N cannot induce direct many-particle processes in absence of inter-particle correlations that help share among the particles the energy transferred by the photon to one-particle which then results in multiparticle excitations. A mathematical elaboration on this point is given in [92] and also confirmed below.

The formula of Eq.(3.48) has been employed in numerous theoretical studies of weakly correlated system such as simple metals [93, 91, 90]. Density functional theory (DFT) generates the initial state of the single-particle with the appropriate energies. The authors of Ref. [91] first calculated the single-particle states via LKKR (layer Korringa-Kohn Rostoker) method. These calculated states are then coupled by electronic interaction V to form the state $\left|\Psi^{(2)}\right\rangle$. The theory reproduced fairly well some of the observed experimental trends, e.g. intensity reduces as the mutual angles of the two excited electrons increase [94] . A detailed comparison however has not been successfully achieved partly due to the problem of the experimental resolution. Applications of DPE to strongly correlated system constitute a challenging task. In the previous section, it has been shown that the two-particle Green's function is intimately related to the double occupancy in the system. In the presence of correlation, electrons tend to be as far apart from each other as is possible which therefore reduces the probability of the formation of bound state. An example of this has been described in Chapter 2 in the context of the metal insulator transition (or see Eq.(2.5)). It is thus expected that the fluctuation of the double occupancy in the system owing to the strong electronic correlation is also reflected in the two-particle spectra.

To show the relation between the two-particle Green's function and the photocurrent of $(\gamma, 2e)$, we write the two-particle photocurrent (J), summed over the non-resolved initial and final states n and m, as follows [95, 91]

$$\begin{aligned} J &= \frac{\alpha_0}{Z}\sum_{N_v}\sum_{mn} e^{-\beta E_n(N_v)}\left|\langle E_m(N_v-2)|\Delta_2|E_n(N_v)\rangle\right|^2 \delta\left(E-[E_m(N_v-2)-E_n(N_v)]\right) \\ &= \frac{\alpha_0}{Z}\sum_{N_v}\sum_{mn,m'm''} e^{-\beta E_n(N_v)} M^{\dagger}_{mm'} M_{mm''} \langle E_n(N_v)|P_2^{\dagger}|E_{m'}(N_v-2)\rangle \\ &\qquad \langle E_{m''}(N_v-2)|P_2|E_n(N_v)\rangle \delta(E-[E_m(N_v-2)-E_n(N_v)]). \end{aligned} \tag{3.49}$$

where $\Delta_2 = \sum_{mm'} \langle E_{m'}(N_v-2)|\,\mathbf{A}.(\hat{\mathbf{p}_1}+\hat{\mathbf{p}_2})\,|E_m(N_v-2)\rangle\, P_2$. Here the short-hand notation M_{kl} stands for the matrix elements. The photon energy is denoted by $E=\hbar\nu$, and β is the inverse temperature. Furthermore, $\alpha_0 = 4\pi^2\alpha/\nu$, and α is the fine structure constant, $P_2 = c_m c_{m'}$ stands for the (hole-hole) two-particle operator acting on the state with N_v particles with the energy $E_n(N_v)$. Z is the partition function. Under certain conditions specified below (the sudden approximation and for high photoelectron energies), the variation of the matrix elements, when photon energy ν is varied as to scan the electronic states of the sample, is smooth in comparison to the change of the matrix elements of P_2. Furthermore, the diagonal elements of M_{kl} are dominant (see below for a justification), i.e. $M_{kl} \approx M$. In this situation Eq.(3.49) simplifies to

(ρ is the density operator).

$$\begin{aligned} J &= \frac{\alpha_0}{Z}\sum_{N_v}\sum_{mn} e^{-\beta E_n(N_v)}|M_{mm}|^2\langle E_n(N_v)|P_2^\dagger|E_m(N_v-2)\rangle\langle E_m(N_v-2)|P_2|E_n(N_v)\rangle \\ &\quad \delta(E-[E_m(N_v-2)-E_n(N_v)]) \\ &= \frac{\alpha_0 M^2}{2\pi Z}\sum_{N_v n}\int dt e^{-\beta E_n(N_v)}\langle E_n(N_v)|e^{iHt}P_2^\dagger e^{-iHt}\ P_2(t=0)|E_n(N_v)\rangle e^{iEt} \\ &= \frac{\alpha_0 M^2}{2\pi Z}\int dt\ \ \mathrm{tr}\left(\rho P_2^\dagger(t)P_2(t=0)\right)\ e^{iEt} \\ &= \frac{\alpha_0 M^2}{2\pi}\int dt \ll P_2^\dagger(t)P_2(t=0)\gg e^{iEt}. \end{aligned} \tag{3.50}$$

On the other hand, from the spectral decomposition of the two-particle Greens function [96] one infers for the two-particle spectral density $P(\omega)$ the relation

$$\begin{aligned} P(\omega) = \frac{\alpha_0}{Z}\sum_{N_v}\sum_{mn} e^{-\beta E_n(N_v)}|\langle E_m(N_v-2)|P_2|E_n(N_v)\rangle|^2 \\ (1-e^{-\beta\nu})\delta(\omega-E_m-E_n). \end{aligned} \tag{3.51}$$

Comparing this equation with equation (3.50) we conclude that under the assumption $M_{kl}\approx M$ the photon-frequency dependence of the two-particle photocurrent is proportional to the two-particle spectral density, i.e.

$$J(\omega)\propto\frac{e^{\beta\omega}}{e^{\beta\omega}-1}P(\omega). \tag{3.52}$$

The Matrix Elements

In the next few sections, we inspect the validity range of the approximation (3.52) that enabled us to assume for the matrix elements $M_{kl}\approx M$. In the experiments, (see Fig.3.1), the photoelectron momenta $\mathbf{k}_1$ and $\mathbf{k}_2$ are chosen to be large such that the escape time is shorter than the lifetime of the hole states. To describe the photoemission dynamics, one concentrates therefore on the degrees of freedom of the photo-emitted electrons (which amounts to the sudden approximation). The matrix elements, e.g. $M_{mm'}$, reduce in the sudden approximation to two particle transition matrix elements M_{if}. The high energy final state (with energies $\varepsilon_1,\varepsilon_2$, see Eq.(3.47)) can be written as a direct product of two Bloch states ($\psi_{\mathbf{k}}$) characterized by the wave vectors $\mathbf{k}_1$ and $\mathbf{k}_2$, i.e.

$$\Psi_{\mathbf{k}_1,\mathbf{k}_2}(\mathbf{r}_1,\mathbf{r}_2)=\psi_{\mathbf{k}_1}(\mathbf{r}_1)\psi_{\mathbf{k}_2}(\mathbf{r}_2). \tag{3.53}$$

Intersite Ground State Correlation

Correlation effects enter in the initial two-particle states. In the absence of spin-dependent scattering (as is the case here) it is advantageous to couple the spins of the two initial states to singlet (zero total spin) and triplet (total spin one) states [97]. In the paramagnetic phase and if the two electrons are not localized on the same sites (they are mainly around $\mathbf{R}_i$ and $\mathbf{R}_j$ with $i\neq j$) the

initial state is a statistical mixture of singlet and triplet states. The radial part can thus be written as [1]

$$\begin{aligned}\Psi_\omega(\mathbf{r}_1,\mathbf{r}_2) &= [\varphi_1(\mathbf{r}_1-\mathbf{R}_i)\varphi_2(\mathbf{r}_2-\mathbf{R}_j) \pm \varphi_1(\mathbf{r}_2-\mathbf{R}_i)\varphi_2(\mathbf{r}_1-\mathbf{R}_j)]\,\chi(|\mathbf{r}_2-\mathbf{r}_1+\mathbf{R}_i-\mathbf{R}_j|) \\ &= \Psi_\omega^{(0)}\chi(|\mathbf{r}_2-\mathbf{r}_1+\mathbf{R}_i-\mathbf{R}_j|. \end{aligned} \tag{3.54}$$

The "plus" ("minus" sign) stands for the singlet (triplet) channel. Note that since the transition operator Δ_2 is symmetric with respect to exchange of particles, there is no need to antisymmetrize the final state (3.53). In eq.(3.54) the functions $\varphi_1(\mathbf{r}_1-\mathbf{R}_i)$ and $\varphi_1(\mathbf{r}_2-\mathbf{R}_j)$ are single-particle Wannier orbitals localized at the sites $\mathbf{R}_i$ and $\mathbf{R}_j$, respectively. N_i is the number of sites and $\chi(|\mathbf{r}_2-\mathbf{r}_1+\mathbf{R}_i-\mathbf{R}_j|)$ is a (dynamical) correlation factor assumed to be dependent on the relative distance between the electrons. The part $\Psi_\omega^{(0)}$ contains correlation effects due to exchange only. Due to the localization of the Wannier states around the ionic sites $\chi(|\mathbf{r}_2-\mathbf{r}_1+\mathbf{R}_i-\mathbf{R}_j|)$ is expected to decay with increasing $r_{1/2}$ (for $i\neq j$). In a lattice periodic problem one expresses the Wannier functions as the Fourier transform of the Bloch states, i.e. $\varphi(\mathbf{r}-\mathbf{R}_i)=\frac{1}{N_i}\sum_{\mathbf{q}}^{1.BZ}\psi_{\mathbf{q}}(\mathbf{r})e^{-i\mathbf{q}\cdot\mathbf{R}_i}$ ($1.BZ$ stands for the first Brillouin zone). With this relation and exploiting the orthogonality of the Bloch states one obtains upon straightforward calculations the following expression for the matrix elements

$$\begin{aligned} M_{if} &= \langle\Psi_f|\mathbf{A}\cdot(\hat{\mathbf{p}}_1+\hat{\mathbf{p}}_2)|\Psi_i\rangle \\ &\approx \frac{1}{N_i}\left\{\sum_{\mathbf{q}_1\mathbf{q}_2}^{1.BZ}\exp(-i\mathbf{q}_1\cdot\mathbf{R}_i-i\mathbf{q}_2\cdot\mathbf{R}_j)M^{(1)}_{\mathbf{q}_1,\mathbf{k}_1}\,\delta_{\mathbf{q}_2,\mathbf{k}_2}\pm 1\leftrightarrow 2\right\}\chi(|\mathbf{R}_i-\mathbf{R}_j|) \\ &\quad+\int d^3r_1d^3r_2\;\Psi^*_{\mathbf{k}_1,\mathbf{k}_2}(\mathbf{r}_1,\mathbf{r}_2)\Psi_\omega^{(0)}\;\mathbf{A}\cdot(\hat{\mathbf{p}}_1+\hat{\mathbf{p}}_2)\chi(|\mathbf{r}_2-\mathbf{r}_1+\mathbf{R}_i-\mathbf{R}_j|). \end{aligned} \tag{3.55}$$

In this equation $M^{(1)}_{\mathbf{q}_1,\mathbf{k}_1}$ is the matrix element for the conventional single photoemission from the Bloch state $\psi_{\mathbf{q}_1}$, i.e. $M^{(1)}_{\mathbf{q}_1,\mathbf{k}_1}=\langle\psi_{\mathbf{k}_1}|\mathbf{A}\cdot\hat{\mathbf{p}}_1|\psi_{\mathbf{q}_1}\rangle$. In deriving the first term of (3.55) it is assumed that $\chi(|\mathbf{r}_2-\mathbf{r}_1+\mathbf{R}_i-\mathbf{R}_j|)$ varies smoothly with $r_{1/2}$, i.e. $\chi(|\mathbf{r}_2-\mathbf{r}_1+\mathbf{R}_i-\mathbf{R}_j|)\approx\chi(|\mathbf{R}_i-\mathbf{R}_j|)$ for $i\neq j$. For 3D periodic structure the first two terms of Eq.(3.55) vanish (momentum and energy conservation laws cannot be satisfied simultaneously). Hence, the transition matrix element is determined by the third term of (3.55), more precisely by the gradient of the correlation factor χ. If this gradient is smooth on the scale of the variation of $\Psi_{\mathbf{k}_1,\mathbf{k}_2}$ and/or $\Psi_\omega^{(0)}$ then the matrix element vanishes all together since $\Psi_{\mathbf{k}_1,\mathbf{k}_2}$ and $\Psi_\omega^{(0)}$ are orthogonal. Explicitly in this case one finds

$$\begin{aligned} M_{if} &\approx \frac{1}{N_i}\sum_{\mathbf{q}_1\mathbf{q}_2}^{1.BZ}\{\exp(-i\mathbf{q}_1\cdot\mathbf{R}_i-i\mathbf{q}_2\cdot\mathbf{R}_j)\delta_{\mathbf{q}_2,\mathbf{k}_2}\delta_{\mathbf{q}_1,\mathbf{k}_1}\pm 1\leftrightarrow 2\} \\ &\qquad \mathbf{A}\cdot(\hat{\mathbf{p}}_1+\hat{\mathbf{p}}_2)\chi(|\mathbf{r}_2-\mathbf{r}_1+\mathbf{R}_i-\mathbf{R}_j|)\Big|_{\mathbf{r}_2=0=\mathbf{r}_1}. \end{aligned} \tag{3.56}$$

[1] This form of the wave function is not the most general one. For a discussion of the terms omitted due to this (ladder-type) approximation see, for example, Ref.[98].

From this expression it can be concluded that the matrix elements diminish for decreasing correlation χ, in fact for $i \neq j$ this contribution to the pair emission is expected to be marginal due to screening.

On-site Ground State Correlation

The major contribution to the matrix element is expected to stem from the onsite emission $\mathbf{R}_i = \mathbf{R}_j$. In the context of Hubbard model, one assumes that the two electrons scatter via a contact potential of strength U when they are on the same site. In this way, the wavefunction reads

$$\begin{aligned}\bar{\Psi}_\omega(\mathbf{r}_1, \mathbf{r}_2) &= \left[\varphi_1(\mathbf{r}_1 - \mathbf{R}_i)\varphi_2(\mathbf{r}_2 - \mathbf{R}_i) + \varphi_1(\mathbf{r}_2 - \mathbf{R}_i)\varphi_2(\mathbf{r}_1 - \mathbf{R}_i)\right] \bar{\chi}(|\mathbf{r}_2 - \mathbf{r}_1|) \\ &= \bar{\Psi}^{(0)}_\omega \bar{\chi}(|\mathbf{r}_2 - \mathbf{r}_1|). \end{aligned} \tag{3.57}$$

$\bar{\Psi}^{(0)}_\omega$ describes the on-site two electron states that include exchange correlation only. Using only $\bar{\Psi}^{(0)}_\omega$ yields zero matrix elements as shown above. To obtain an expression for the correlation factor $\bar{\chi}(|\mathbf{r}_2 - \mathbf{r}_1|)$ (that tends to 1 for $U \to 0$), it is convenient to switch to relative $\mathbf{R}_-$ and center of mass coordinates $\mathbf{R}_+$. It can be argued that $\bar{\chi}(|\mathbf{r}_2 - \mathbf{r}_1|)$ is determined by the integral (Lippmann-Schwinger) equation (χ_0 is determined by asymptotic conditions) $\bar{\chi}(R_-) = \chi_0 + U \int d^3\mathbf{R}'_- g^r(\mathbf{R}_-, \mathbf{R}'_-)\delta^{(3)}(\mathbf{R}'_-)\bar{\chi}(\mathbf{R}'_-)$, where g^r is the retarded Green's function in the relative coordinate. For (3.57) one finds

$$\bar{\Psi}_\omega(\mathbf{r}_1, \mathbf{r}_2) = \bar{\Psi}^{(0)}_\omega(\mathbf{r}_1, \mathbf{r}_2)\left[1 + \bar{U} g^r(\mathbf{r}_1 - \mathbf{r}_2, 0)\right], \quad \bar{U} = \frac{U}{1 - U g^r(0,0)}. \tag{3.58}$$

The key point inferred from this relation is that the two-particle transition amplitude increases as $\bar{U}$ increases ($\bar{\Psi}^{(0)}_\omega$ does not contribute to the matrix elements) and it vanishes for $U \to 0$.
To summarize this section we can say for fixed momenta $\mathbf{k}_1, \mathbf{k}_2$ of the photoelectrons and a given U, the frequency dependence of the two-particle emission, $J(\omega)$, is related to the frequency dependence of the spectral function $P(\omega)$. For a given ω, the matrix elements vary with U; they contribute a $\bar{U}^2$ dependence to $J(\omega)$.

CHAPTER 4

Single and Isotropic Two-Band Hubbard model

4.1 One Band Hubbard Model

In this chapter we discuss the results of the single- and the two-particle spectral function of the single band Hubbard model. Our aim is to show the behavior of two-particle spectral function in the vicinity of Mott transition. In doing so, we employ three approximations namely DMFT-QMC and DMFT+ Ladder Approximation (LA) and first order approximation. As is already pointed out in the previous chapter, the first approach calculates the single- and two-particle within the same loop of DMFT. The other two methods on the other hand combine the results of the single-particle DMFT and additional approximation for two-particle Green's function. In this section, we therefore also compare the accuracy of the two-particle approximation that employs accurate single-particle spectral function. In what follows the presented results for the single band Hubbard model are obtained at temperature $T/W = 0.05$ and time interval $\Delta\tau < 0.5$. The unit energy is $W = 1$ and semicircular density of states is employed in the DMFT-QMC self consistency.

At half-filling (left panel of Figure 4.1) the quasiparticle peak at the Fermi energy is the dominant feature of the single-particle spectra in the weak coupling interaction signifying a metallic behavior; the carriers are itinerant and a Fermi liquid picture is appropriate. With an increasing strength of electronic correlations, localization sets in accompanied by a gradual disappearance of the quasiparticle weight and the formation of a pseudogap. Electron transfer between the two bands may occur, albeit its probability is smaller than that in the previous case. As the coupling strength further increases, the gap fully develops indicating an insulating state. The role of the double occupancy we inspect by studying the quantity $\langle n_\uparrow n_\downarrow \rangle$ calculated in the DMFT-QMC loop. Evolving from the weakly interacting (metallic) case to the strongly interaction (insulating) phase the double occupancy is reduced[28], for more energy is required to overcome the stronger repulsion whenever forming the double occupation.

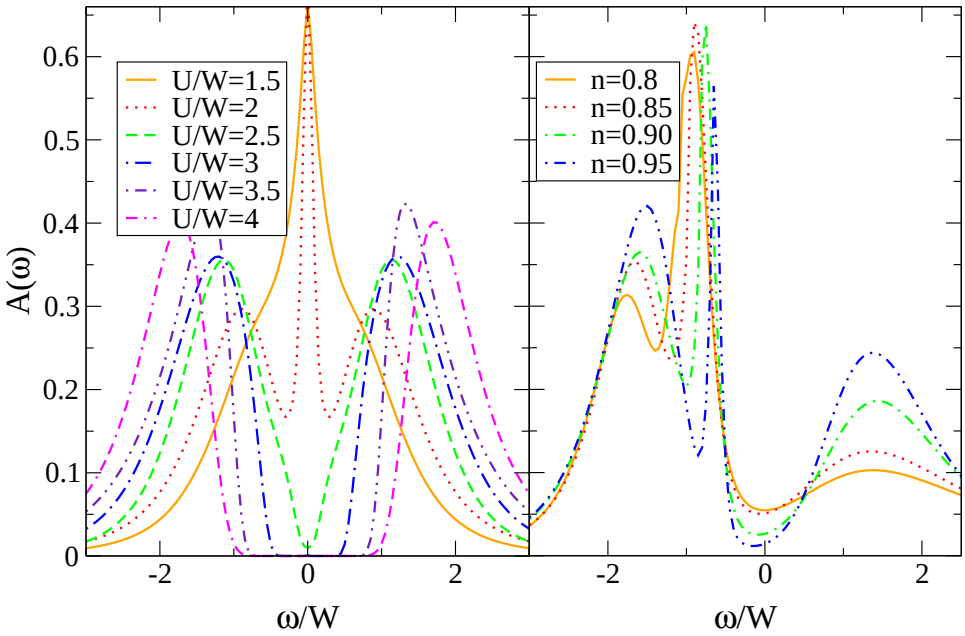

Figure 4.1: The results of the DMFT-QMC for the frequency dependence of the single-particle spectral function $A(\omega)$ for the single-band Hubbard model at half-filling for various interaction strength U (left panel) and for various electron occupancy at $U/W = 3$ (right panel).

The influence of dopant concentration on the MIT is demonstrated by doping the insulating phase as depicted in right panel of Figure 4.1. Contrasting with the results at half-filling with an interaction strength $U/W = 3$, one observes the existence of a pseudogap in the spectra. The hole doping stimulates the formation of quasi-particle peak so that the system attains a metallic character. This is because the doping enhances the number of holes which in turns increases the itineracy in such a way that electron can hop effectively from one site to the other.

Having commented on the generic single-particle properties of the single-band Hubbard model for Mott systems, we turn now to the discussion of the particle-particle spectral function. For small U/W one obtains an intense peak that lies close to $\omega/W = 0$. The origin of such features can be inferred from the structure of the single-particle spectral function as in this case P is expected to be well modeled by a convolution of two single-particle spectral functions. Small increase of U/W leads to the reduction of spectral weight and the shift of peak into higher energy (far from $\omega/W = 0$). The latter is attributed to the difference of the Hubbard peaks in the single-particle spectral function. As the interaction strength increases, the spectral weight decreases significantly signaling a reduction of double occupation. This argument is supported by the results of the integrated spectra depicted in the inset of Fig.4.2. In addition to the reduction of the spectral weight, one also observes the formation of a gap in the low energy regime (near to the zero frequency) for strong interaction. This two-particle gap resembles the one that appears in the single-particle spectra (cf. Figure.4.1) which is the usual indicator for an insulating state.

As is already pointed out above, the reappearance of the low energy resonance as a function of the doping in the single-particle spectral function is a signal for the metallic character. The

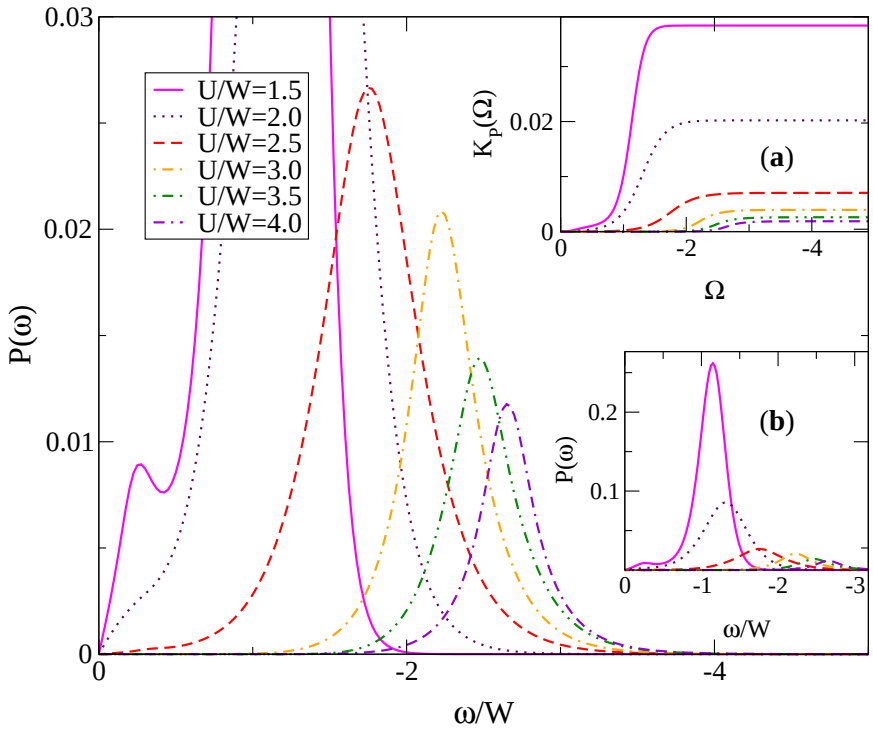

Figure 4.2: Two-particle spectral function as function of the correlated, two-particle initial energy ν for various interaction strengths. Calculations are performed within the self consistency scheme of DMFT-QMC method. The large scale figure is shown in inset (**b**). Inset (**a**) shows the integrated spectra using equation (3.40).

same pattern is also observed here in the two-particle spectral function where the strongest peak occurs in the lowest electron occupancy and decreases as the Mott insulating phase is approached. Thus the two-particle spectra highlight the contribution of holes to the double occupancy probability, which is supported by the results for the integrated spectra (see inset of Fig.4.3).

To inspect the role of the ladder diagram summation (i.e. Eq.(3.37) with results in the right panel of Fig.4.4), we compare with the results of the first-order approximation (shown in left panel of Fig.4.4) using (3.38) (i.e. with the convolution of the single-particle spectra). The results of the first order approximation show a smooth, broad Gaussian-like feature in the spectra for all interaction strengths. This is due to the self-convolution that tends to wash out the character of the original function. The presence of a gap in the two-particle spectra highlights the difference between the weak and the strong coupling interactions in agreement with the previous result of DMFT-QMC and with the same energetic origin as discussed above. That this correct energetic shift is reproduced by this simple scheme is the result of using an accurate single-particle spectral function. Another point is the evolution of the two-particle spectra from the weak through the strong coupling limit and the associated behavior of the spectral weight. In the scheme used in Fig.4.4, the weight seems to be comparable for all values of the interaction strengths except for $U/W = 2$ which originates from the low shoulder in the spectra in Figure.4.2 The reduction of the spectral weight is related to the probability of the double occupancy. It is then conceivable

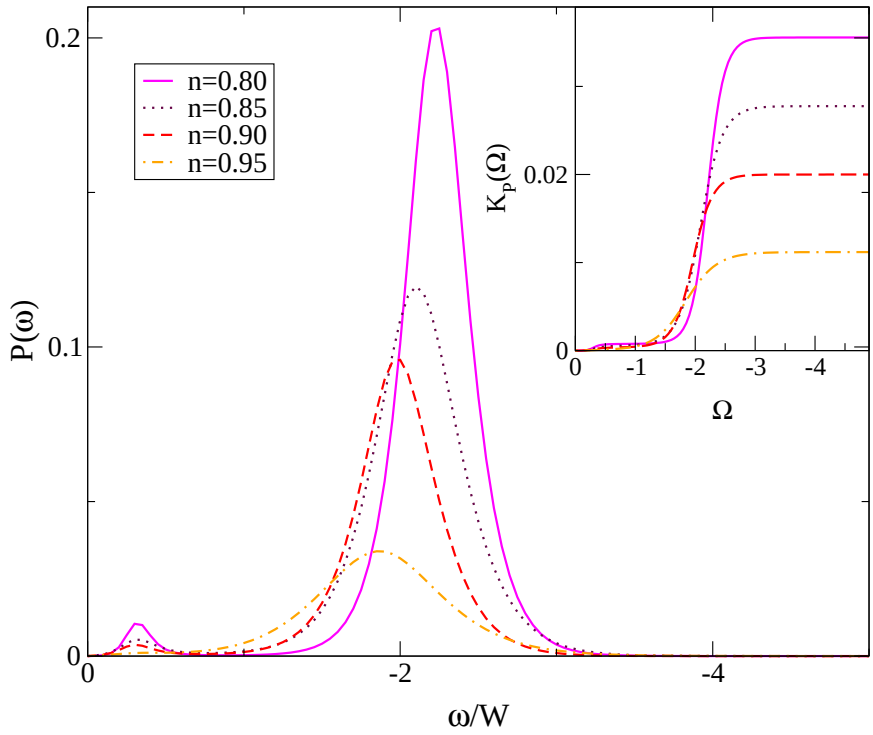

Figure 4.3: Particle-particle spectral function of the single-band Hubbard model away from half-filling for $U/W = 3$, $T/W = 0.05$ and various occupation numbers n . The inset shows the integrated spectra according to equation (3.40).

to infer that this scheme violates the sum rule for the two-particle spectral function (which is dictated by the double occupancy, see equation (3.39). This is endorsed by the results for the integrated spectra shown in the inset of figure 4.4. The shift to higher frequencies is due to the presence of the gap. No clear suppression is observed as in Figures 4.3 and 4.4.

Having obtained the imaginary part of the first order approximation we inspect the influence of the ladder diagram summation on the two-particle spectra. The results are presented in the right panel of Fig.4.4. In contrast with previous results obtained in the first order approximation, the spectra delivered by DMFT-LA are non-uniform with smooth broad feature and a satellite peak. For the weak interaction strength, the two-particle spectra hardly depend on the Coulomb interaction strength. As before no clear reduction of the spectral weight is observed. Interesting features in the DMFT-LA scheme emerge at higher interaction strengths, which from the point of view of the single-particle spectra, is already the regime of the insulating phase. Instead of suppressing the spectral weight, the increase of the coupling interaction strength results in a narrow satellite peak. The integrated spectra depicted in the inset of Fig.4.4 (right panel) shed some light on this result. The integrated spectra within the ladder approximation exhibit a suppression of the weight for higher frequencies in contrast to the results of the first-order approximation. We remark that in the ladder approximation the suppression of the integrated spectra is not related to a diminishing of the weight of the two-particle spectral function but is associated with the width

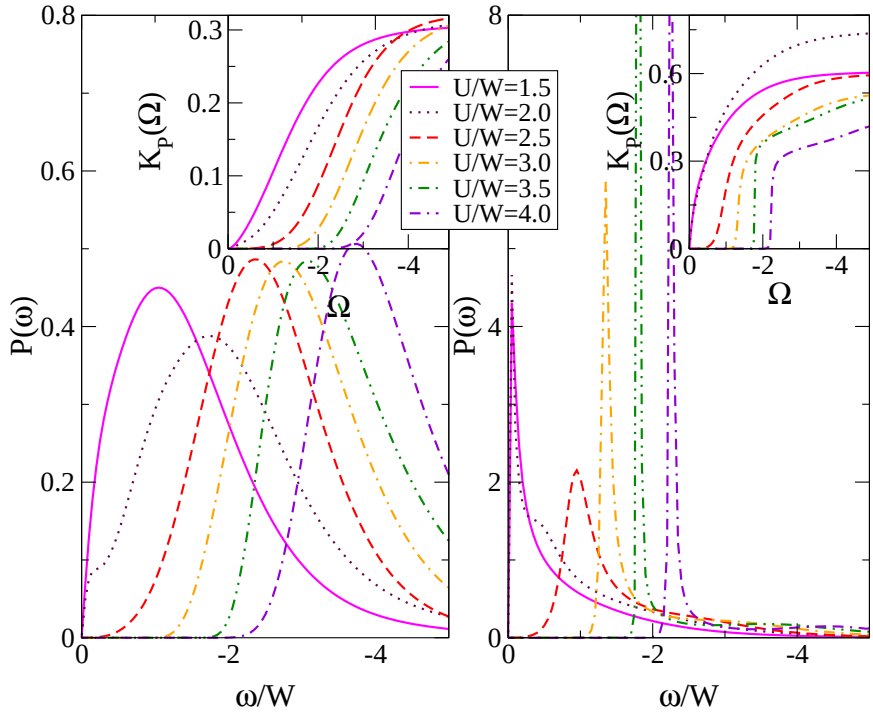

Figure 4.4: The frequency dependence of the two-particle spectral function at half-filling, calculated with the first order perturbation (left panel) and with the full ladder approximation (right panel). Various curves correspond to different interaction strengths. The insets show the integrated spectra. Same notation and parameters as in Fig.4.2.

of the spectra that become narrow as the interaction increases.

The two-particle spectral function away from half-filling is depicted in Fig.4.5 for various occupancies and for $U/W = 3$; calculations are performed within the first-order approximation and within the ladder approximation. No gap formation in the two-particle spectra takes place. This is consistent with the behavior of the single-particle spectral function for which the hole doping of the insulating phase stimulates the formation of quasiparticles. In the first-order approximation, one obtains the usual broad Gaussian-type structure that becomes more dominant as the dopant concentration increases. A somewhat similar situation is also observed for the results of DMFT-LA. In the latter, however, one observes an intense low-energy peak close to half-filling which decreases as the doping increases. The results from both approach thus in contrast with that of DMFT+QMC where the largest spectral weight is obtained for high doping concentration. These results therefore do not reflect the fact that the addition of doping leads to the increase of double occupancy in the system. The same is also indicated by the sum rule plotted in the inset of 4.5. Here one observes that the spectral weight becomes minimum for the maximum value of doping which thus violates the two-particle sum rule for the system close to Mott transition. A similar finding has been observed in reference [99] where the bare ladder approximation (BLA) has been utilized. In Ref. [99], the decrease of the electron occupancy also increases the peaks in the spectra, which is assumed to be a violation of the two-particle sum rule. On the other

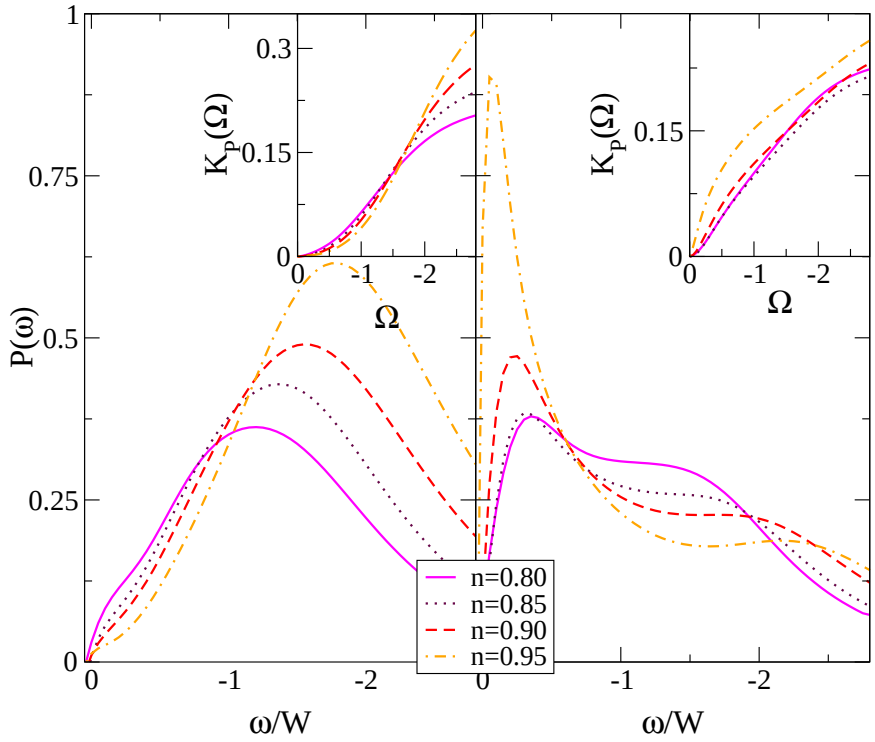

Figure 4.5: The same as in Fig.4.4, however the results are for two-particle spectra of the hole doped case for various electron occupancy n at an interaction strength $U/W = 3$. The left panel depicts the results of the first-order approximation whereas in the right panel the predictions of the ladder approximations are plotted.

hand, by using the time-dependent Gutzwiller approximation the opposite situation occurs: The two-particle spectral weight diminishes as the Mott insulating phase is approached, which is in line with what we obtained above within the DMFT-QMC.

4.2 Isotropic Two-Band Hubbard model

As is already pointed out, the single band Hubbard model upon which the above discussion is based, is useful for systems with only a single band being close to the Fermi energy. To inspect the role of the orbital degrees of freedom, which is known to be important for the properties of strongly correlated systems, a multi-orbital model is needed. It is the aim of this section to study the influence of the orbital degeneracy on the single and the two-particle spectra. The results for the single-particle spectral function within the two band Hubbard model are presented in Figure 4.6. The results are similar to those obtained within the single band Hubbard model (cf. Fig.4.2). The metallic phase shows an intense quasiparticle peak that diminishes as the coupling interaction becomes stronger. The formation of the gap for a high interaction strength shows the existence of an insulating phase in this degenerate system. As mentioned before, an essential point that distinguishes the Mott transition in the single from the degenerate band is the value of the critical coupling necessary to obtain a dip in the spectral function. From the orbitally resolved

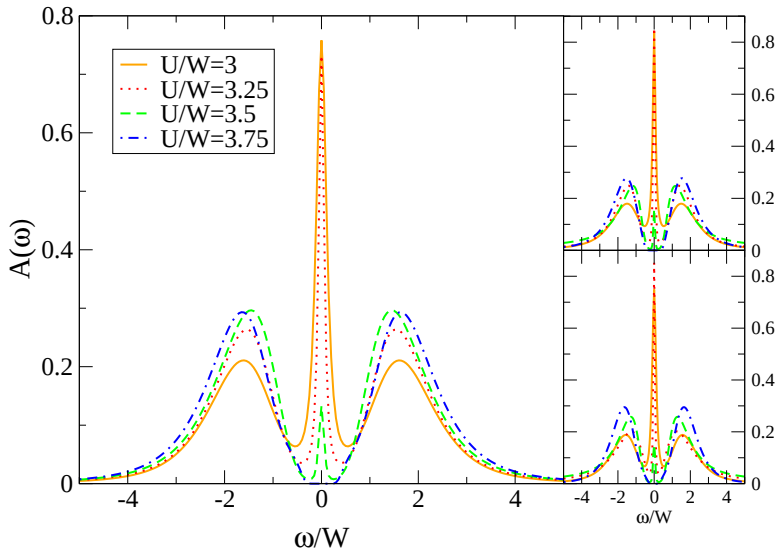

Figure 4.6: The DMFT-QMC results for the frequency dependence of the single-particle spectral function $A(\omega)$ of the two-band, isotropic Hubbard model at half-filling. Various curves corresponds to different interaction strengths U/W. The insets show the orbitally resolved spectral functions for the first (upper inset) and second bands (lower inset).

spectral function depicted in the embedded figures, one also learns that each band undergoes the same transition from the metallic to the insulating phase. For anisotropic bandwidth each band undergoes an independent metal-insulator transition, a behavior coined as the orbital-selective Mott-transition (OSMT) and will be further elaborated in the next chapter.

The results of DMFT-QMC calculation for the two-particle spectral function are illustrated in Figure 4.7 that contains the two spectral functions of the total band (left panel) and inter-band (right panel). From Fig.4.7 we see that a small increase of the Coulomb interaction in the weak coupling regime hardly affects the overall spectral weight. Further increasing the interaction strength leads however to the reduction of the spectra as well as to a shift of the dominant peak to higher energies.

The two-particle spectral function of the total bands from the first order approximation and the ladder approximation is depicted in left and right panel of Figs.4.8 respectively. As expected, the former approach delivers the broad Gaussian feature which is a consequence of the self-convolution. As the interaction increases the spectral weight is shifted to higher energies and the low energy gap becomes evident. In contrast, the results of ladder approach (see right panel of Fig.4.8) show an enhancement of the spectral intensity as the interaction increases. Despite the fact that a higher coupling is necessary for the formation of the gap, the behavior of the spectral function of the total bands for the two band Hubbard model mimics that of the single band case (see Fig.4.4)

For the case of interband spectra, the two-particle spectra obtained by means of the first order approximation as well as by the ladder approximation are shown in the left and right panel of

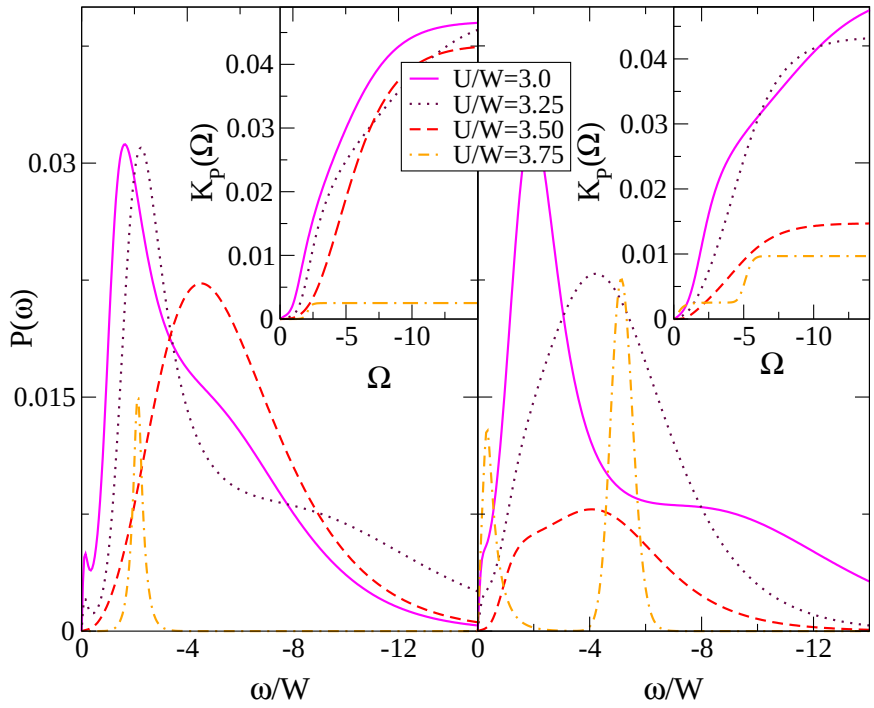

Figure 4.7: The two-particle spectral function of the degenerate Hubbard model at half-filling as a function of Coulomb interaction U/W. The calculations are performed by the DMFT-QMC method including total bands (left panel) and inter-band (right panel). The insets show the integrated spectra.

Fig.4.9 respectively. The behavior of the two-particle spectra in the single band Hubbard model obtained within the same scheme (see Fig.4.2) (e.g. the gap existence, absence of the spectral weight reduction) is also observed in the present case. In the metallic case however there are new features predicted by both approximations namely a double peak structure that disappears in the insulating phase. Other notable features such as the increase of the weight as the coupling strength increases are present in the results of both methods. The integrated spectra of the degenerate model indicates a violation of the sum rule for the two-particle spectra by both the first order approximation and the ladder approximation. From the three scheme: QMC-DMFT, first order and ladder approximations, the DMFT-QMC method provides the more reasonable predictions which practically always obey the sum rule as a constraint on the two-particle spectral function. This is because, both the single and the two-particle propagators are calculated on an equal footing in the self consistency DMFT. An accurate single-particle approach when formulating the two-particle propagator, does not however guarantee the fulfillment of the sum rules. The use of an accurate approach in the single-particle spectra captures however pertinent features such as the gap opening in the insulating state which is also observed in the result of DMFT-QMC.

To connect the results of the two-particle spectra of the Hubbard model (see for example Fig.4.2) to the $(\gamma, 2e)$ signal it is decisive to recall the statements of Eq.(3.47) and Eq.3.58). The correlated two-particle initial energy that appears in Eq.(3.47) and which is scanned in Fig.4.2,

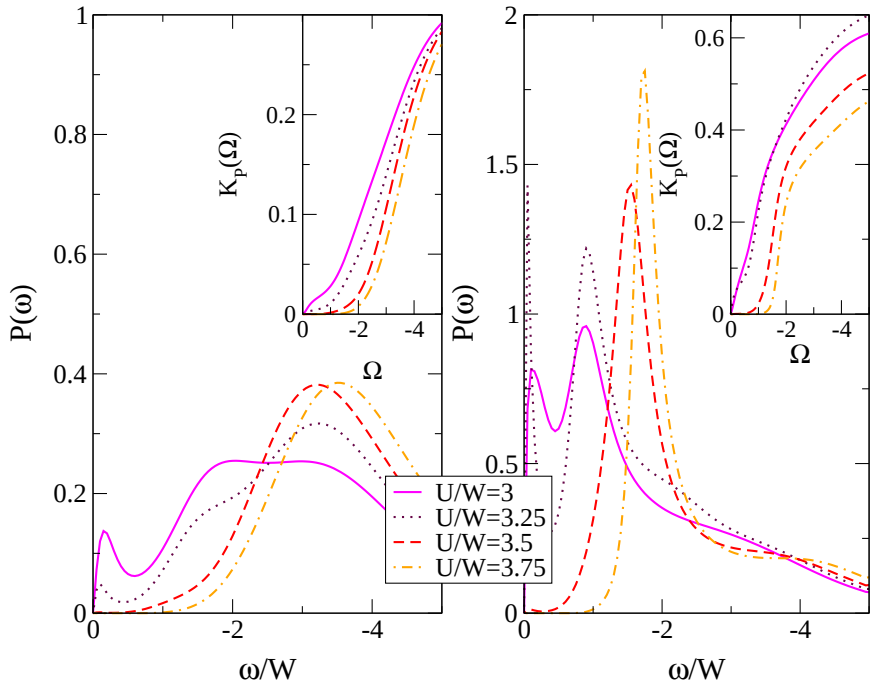

Figure 4.8: The same as in Fig.(4.7) for the total bands. The left panel shows the results of the first order approximation and in the right panel those of the ladder approximation.

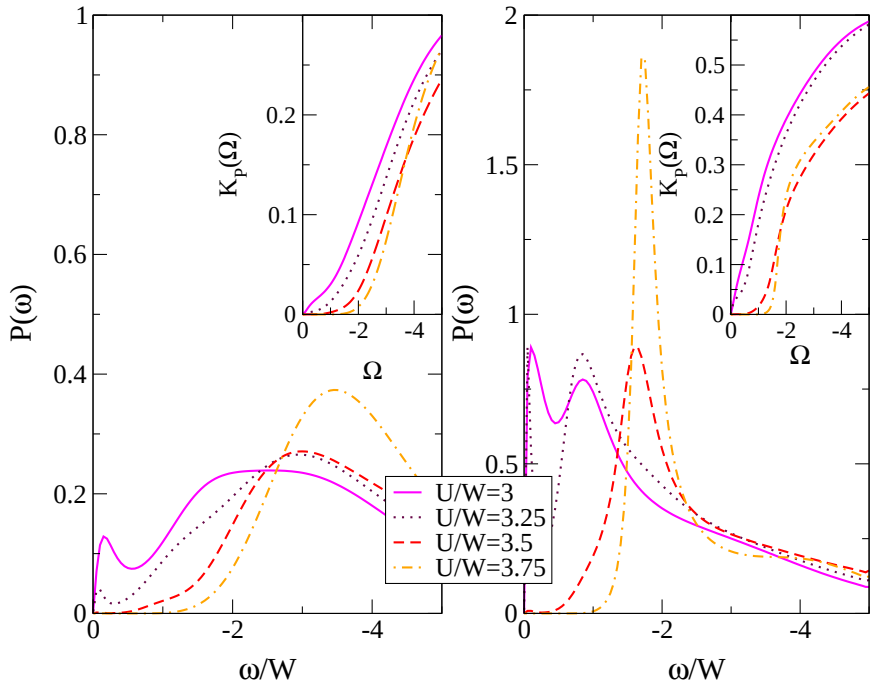

Figure 4.9: The same as in Fig.(4.8) for the interband Hubbard model at half-filling. The figure shows the results of the first order approximation (left panel) and of the ladder approximation (right panel).

is in the uncorrelated case merely the sum of two single-particle energies ω_i (ω_{uncor} = ω_1 + ω_2), i.e. in the metallic uncorrelated case we expect some spectral weight around $\omega = 0$ in Fig.4.2. For a finite U/W, i.e. for a correlated system one thus requires more energy to compensate the repulsion of the Coulomb interaction. This is the reason for the shift of the two-particle peak in Fig.4.2 with increasing U. The same can be observed in the single-particle spectral function where the distance between Hubbard band approximately in order of U/W. The tendency of larger spectral density with decreasing U is not reflected in the (γ,2e) signal J. In fact, the opposite will occur. The reason for this is that according to Eq.(3.52) and Eq.(3.58) J is proportional to the product of the matrix elements and the spectral function. On the other hand the matrix elements decrease with U (cf. Eq.(3.58)), and in fact vanishes for $U \to 0$ counteracting against the trend with U of the spectral function P (cf. Fig.4.2). We stress however, that the results of the two-particle spectral function depicted above are still relevant to the $(\gamma, 2e)$ measurements in that, for a given U, the matrix elements are hardly dependent on ω.

4.3 Two-Dimensional Hubbard Model

Immediately after the discovery of high-temperature superconductivity by Bednorz and Müller in 1986[100], Anderson suggested [101] that the two-dimensional (2D) Hubbard model holds the key to explaining this phenomenon. The band structure calculation of cuprates compound [102] indeed showed that the quasi two-dimensional layer CuO_2 has a pronounced contribution near the Fermi energy. Following Anderson's proposal, a great theoretical effort has been devoted to studying the physics of 2D Hubbard model. Despite years of effort, there is no conclusive evidence for the existence of superconductivity. In this connection, it is widely believed that the understanding of the normal state properties may provide important clues to the superconducting mechanism. This is motivated by the fact that cuprates exhibit a number of anomalous properties which is somewhat difficult to understand within the framework of the Fermi-liquid theory. One of the most controversial issues is perhaps the origin of the pseudogap in the single-particle excitation which is a generic feature of the hole- and electron-doped high-T_c systems.

Various approaches have been implemented to investigate the electronic structure of the 2D Hubbard model. The results of numerical simulations within the finite size lattice quantum monte carlo (QMC) have indicated that the groundstate of the model at half-filling is antiferromagnetic insulator. When the system is doped away from half-filling, it becomes metallic and then superconducting. The relationship between the metal-insulator transition (MIT) and antiferromagnetism (AFM), however, remains less understood. In addition, it was shown by several authors that the suitable scenario of pseudogap formation is the one that closely related to the short-ranged AFM fluctuations [103, 104]. In view of MIT, there are two limiting cases that have to be considered. In the weak coupling ($U << W$), spin-density-wave instability occurs due to the presence of van Hove singularity and perfect nesting of the Fermi surface. The MIT in this picture is due to the doubling of the unit cell generated by magnetic ordering. The sec-

ond opinion was suggested by Anderson that assumed large Coulomb repulsion U (compared to the bandwidth W). In this strong coupling approach, the Mott gap is present for all $U > 0$ as in one-dimensional systems. The antiferromagnetic order in the low temperature is thus the consequence of the MIT.

In the previous section, it has been shown that the metal-insulator transition in the high dimensional limit can be tackled efficiently by means of DMFT. Based on the concept of local self energy, the lattice problem is mapped onto the corresponding impurity Hamiltonian with additional self consistency relations. The locality of the self energy however becomes one of the main drawbacks of DMFT. The approximation is thus inappropriate when dealing with various problems in which the contribution of spatial fluctuation is important e.g. spin density waves, *d-wave* pairing, stripes, momentum-selective Mott transition. Investigations of pseudogap formation that is related to the spin fluctuation and also metal insulator transition in 2D Hubbard model should also go beyond the local approximation. In addition, it is well-known that the accuracy of the mean field approximation such as DMFT declines in the lower dimensionality. To overcome this problem, it is thus necessary to restore the spatial dependance of the self energy in the DMFT. As is already pointed out in Chapter 2, the way non-local contributions are brought back into DMFT is not unique and one can thus start from different level of approximations. Some examples are Cluster DMFT, DMFT+$\Sigma_{\mathbf{k}}$, dynamical vertex approximation (DΓA), Extended Dynamical Mean Field Theory (EDMFT).

In this section, we discuss the paramagnetic metal insulator transition in the two-dimensional Hubbard model. The main purpose is to study the role of spatial fluctuations at the verge of the metal insulator transition at and off half-filling. To that end, we employ EDMFT where spatial correlation is incorporated via spin-spin correlation term in the Hubbard Hamiltonian as expressed in the Eq.(2.77). The information of lattice is obtained from the two-dimensional density of states which can be analytically derived from the dispersion energy expressed as

$$\epsilon(\mathbf{k}) = -2t\cos(kx) - 2t\cos(ky) + 4t'\cos(kx)\cos(ky), \tag{4.1}$$

with t, t' correspond to the nearest and the next-nearest neighbor hopping amplitude respectively. In the results presented below, only nearest neighbor will be considered. Thus one deals with symmetric density of states with the van Hove singularity at the center of the band. The effective action of EDMFT as expressed in the Eq.(2.79) together with the self consistency relation of electrons and bosons is finally solved by employing the extended version of QMC method that incorporates the electron-boson degrees of freedom. In the calculation, we set the bandwidth $W = 2$, the temperature $T/W = 0.1$, the Coulomb interaction $U/W = 1$ and the increment of time slices as $\Delta < 0.24$.

At first, let us discuss the evolution of dynamical spin susceptibility for different values of the spin coupling I/W as illustrated in the left panel of Fig.4.10. We note here that since the presented results are obtained in the paramagnetic phase and also in the absence of a magnetic field then the relation of longitudinal χ_z and transversal spin susceptibility $\chi_\pm$ expressed as $\chi_\pm =$

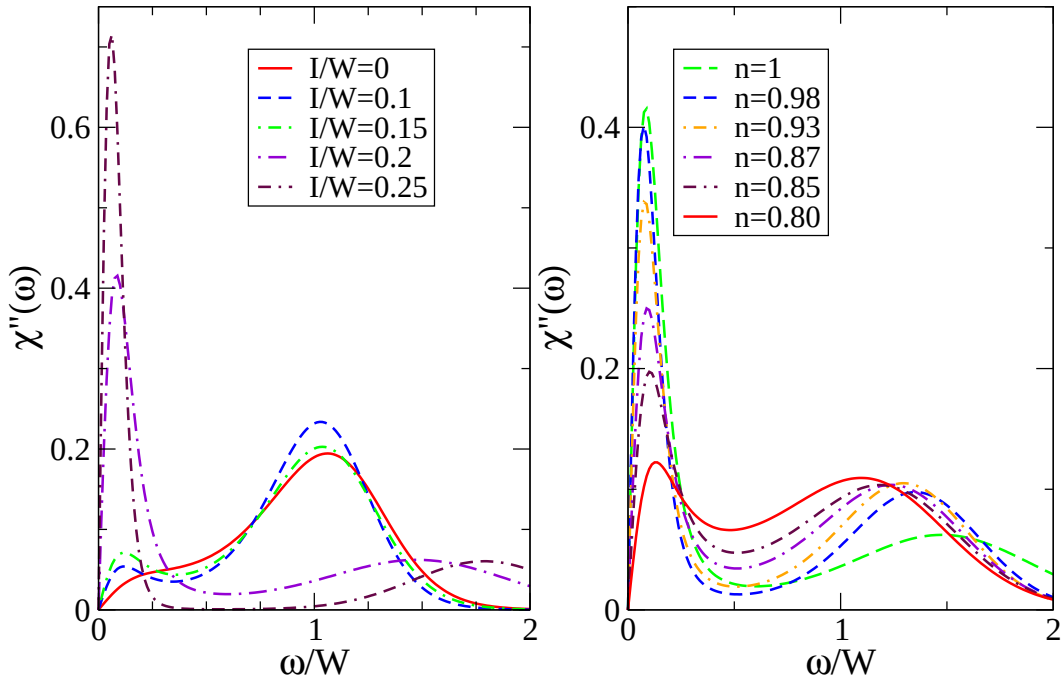

Figure 4.10: The left panel shows the imaginary part of dynamical spin susceptibility $\chi''(\omega)$ of the two-dimensional Hubbard model at half-filling for various coupling I/W at $U/W = 1$. The right panel illustrates the results for various occupation number at $I/W = 0.2$.

$2\chi_z$ holds[105]. Within our calculational scheme, we have checked that the above relation is well fulfilled. The dynamical spin susceptibility is composed of broad single peak in the absence of intersite interaction and the low frequencies are linear in ω. Inclusion of spin interactions slightly changes the high energy part of the susceptibility which is accompanied by the gradual increase of the low-energy spectra. Note that the former is located at the order of $\approx t^2/U$. When spin coupling is increased, the primary low-energy peak becomes sharper and concomitantly suppresses the high energy spectral weight. In order to fully understand these behavior, it is interesting to have a look into the standard phenomenological descriptions of the spin excitation provided by the random phase approximation (RPA) where the spin susceptibility $\chi(\mathbf{k},\omega)$ is expressed as

$$\chi(\mathbf{q},\omega) = \frac{\chi_0(\mathbf{q},\omega)}{1 - I\chi_0(\mathbf{q},\omega)}. \tag{4.2}$$

Here $\chi_0(\mathbf{k},\omega)$ is the non-interacting susceptibility reads

$$\chi_0(\mathbf{q},\omega) = \sum_{\mathbf{k}} \frac{f(\epsilon(\mathbf{k}+\mathbf{q})) - f(\epsilon(\mathbf{k}))}{\omega + \epsilon(\mathbf{k}) - \epsilon(\mathbf{k}+\mathbf{q})}, \tag{4.3}$$

and I is the coupling interaction. In the absence of interactions, the particle-hole propagator can be analytically evaluated. It is also known that in the limit of $\omega \to 0$ the imaginary part of susceptibility is proportional to ω. The increase of coupling I, particularly toward the Stoner instability criteria leads to the enhancement at the low energy peak known usually as paramagnon.

The adjustment of the low-energy susceptibility is simultaneously followed by the changes in the effective mass m^* and equivalently in the single-particle self energy. Generally, this enhancement can be taken as the signal for the formation of the local moment in the system. Armed with this knowledge, the increase of low-energy susceptibility in Fig.4.10 as a function of intersite spin coupling is thus a clear signature of the formation of local moment and the instability of metallic phase.

The influence of dopant concentration on the spin suseptibility is depicted in the right panel of Fig.4.10. It is calculated with the same parameters described above but for $I/W = 0.2$. In general, the spectra are characterized by "peak-dip-hump" structure for all band occupancies. These results indicate that the high energy peak at half-filling for $I/W = 0.2$ is physical. As the system is doped, there is a decrease of low energy spectral weight which is readily observed in the low doping concentration, e.g. $n = 0.98$ and this is followed by the increase of high energy part. We interpret the high energy hump as the excitation from low energy states to other excited states. The changes of spectral weight further evident as the dopant concentration increases. Finally at the highest doping, one observes a broad response which also consists of small peak at low energy part, an artefact from the half-filled case. In contrast with that of half-filling, the overall behavior of the dynamical spin susceptibility in the present case can not be described within RPA theory in particularly at high energies. Nevertheless, the adjustment of the lineshape of the susceptibility marks the influence of the doping and thus electronic correlation and more importantly this changes will be reflected in the single-particle level. In this case, we expect the reduction of effective mass as well as the changes of the self energy toward metallic like behavior. In addition, the presence of the dip in the spin excitation is also of interest since it might contribute to the additional behavior in the single-particle spectra.

Results of single-particle spectral function for different values of I/W are illustrated in the left panel of Fig.4.11. In the absence of intersite spin interactions but for small coupling values, the spectra consist of a single peak resonance signifying the metallic character of the system. This quasiparticle peak is the smoothed van-Hove singularity due to the influence of many body interactions. At small intersite coupling $I/W = 0.15$, one observes a reduction of the spectral weight at $\omega = 0$ which can be attributed to the small increase of the low-energy spin excitation spectrum. As the interaction further increases, the quasiparticle peak is significantly suppressed and the formation of the lower and the upper Hubbard bands becomes more clear. In the higher coupling value $I/W = 0.25$, one can see the formation of a dip at the Fermi level, indicating that the system at the verge of metal insulator transition. In this regime, the imaginary part of self energy diverges and as is already pointed out above, one also observe the formation of local moment. On the basis of this result, one may conclude that the low energy enhancement of the spin susceptibility, has its manifestation at the single particle level namely the opening of dip or the collapse of quasiparticle peak. This also provides an important hint that there is strong instability of metallic phase in two dimensional Hubbard system when the spatial fluctuation is considered.

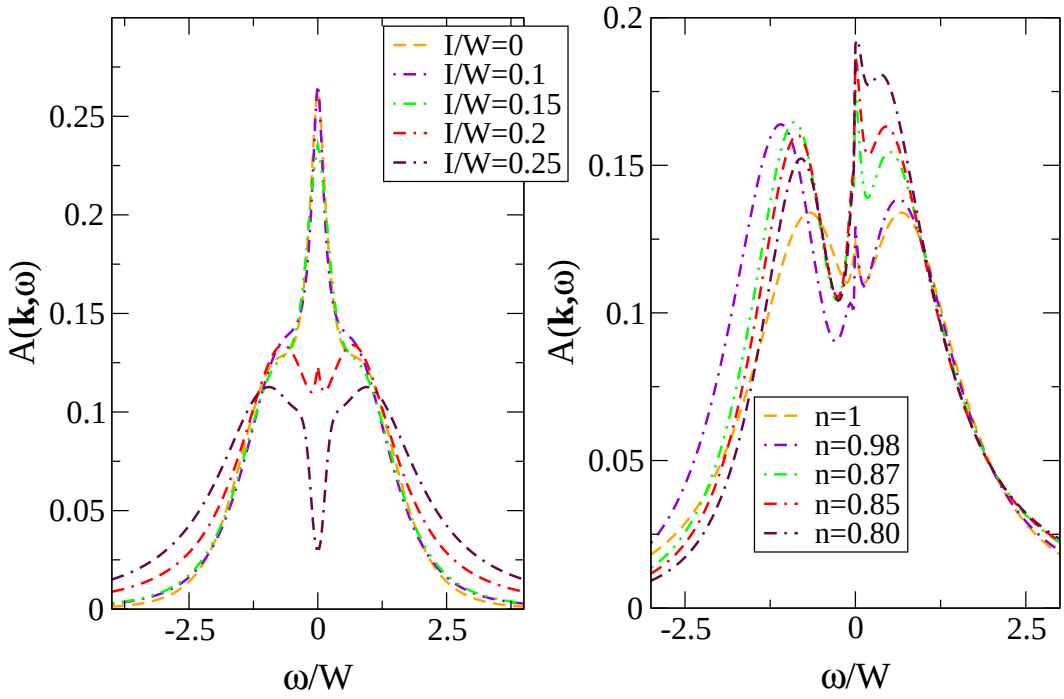

Figure 4.11: The spectral function of the single-band two-dimensional Hubbard model for $U/W = 1$ $T/W = 0.1$ and at momentum vector $\mathbf{k} = (\frac{\pi}{2}, \frac{\pi}{2})$. The results of the left panel are for various values of I/W at half-filling whereas the right panel are for different band fillings.

The results of single-particle spectral function further suggest that the metal insulator transition is possible even in the weak coupling interaction $U < W$ meaning also that the gap is always present for all $U > 0$. Since the calculation are performed in the paramagnetic phase, the strong coupling approach by Anderson is thus more relevant to explain the mechanism of MIT in the 2D Hubbard model. It is interesting to note here that the formation of pseudogap has also been observed within the DMFT+$\Sigma_{\mathbf{k}}$ scheme [33, 34]. They pointed out that, in comparison to the charge density fluctuation, the spin fluctuation induce stronger instability in the metallic phase that finally leads to the formation of gap at the single particle spectra. The same is also shown by cluster extension of DMFT, where in this respect the decrease of the spectral weight at the Fermi energy heavily depends on the cluster sizes. It is shown that in order to obtain the full gap opening at the single particle spectral function, it is necessary to consider large cluster size [106]. The study of the influence of spatial fluctuation in the three dimensional Hubbard model has been recently reported in the ref.[35] that employs the DΓA method. They pointed out that the short-range antiferromagnetic fluctuation could also influence the stability of the quasiparticle peak.

Let us now consider the hole doped case. The spectra are depicted in the right panel of Fig.4.11. The model parameters are still the same as above but in this case the spin coupling is fixed as $I/W = 0.2$. It is clearly seen that doping has a strong influences on the low energy part of the spectra. The resonance close to $\omega/W = 0$ emerges again as a function of doping,

signal of the increase of the itinerant character. Along with this, the spectra now consists of the pseudogap for all band filling that lies close to the peak at Fermi energy. The enhancement of the quasiparticle peak is clearly a manifestation of the diminishing of the low-energy susceptibility. In addition, the pseudogap that persists to the overdoped case can be considered as a counterpart of the low-energy gap in the spin susceptibility. In order to fully understand the nature of the low energy peak as well as the pseudogap it is necessary to inspect the imaginary part of the self energy. This to ensure that such behavior does not originate from the numerical continuation of the imaginary quantities. In this respect, we obtain that the low-energy part of the self energy extrapolates to the finite value $\mathrm{Im}\Sigma(\mathrm{i}0^{+}) = \Gamma \neq 0$ thus suggests that there is a finite lifetime at the Fermi level meaning that the well defined Fermi liquid state is absent. We will further investigate this fact and elaborate the discussion during the presentation of the optical spectra, presented in the next section.

4.3.1 Optical Conductivity and Pair Excitation Within The 2D Hubbard model

As is already pointed out earlier, the electromagnetic response of the system provides a clear signature of electronic correlations. The effects are usually manifested in the shift or in the vanishing of the Drude weight and also in the formation of the optical gap in the conductivity spectra. This for example is observed in the metallic phase of the vanadium oxide (V_2O_3) that shows a Drude weight and an additional incoherent peak at the higher frequency. As electronic correlation increases, the gap appears in the low energy mimics that observed in the spectral function [28, 107]. In this section, we will discuss the evolution of the optical conductivity spectra of the 2D Hubbard model as a function of the non-local spin fluctuation and the dopant concentration. At first, let us observe the influence of the non-local spin fluctuation as illustrated in the left panel of Fig.4.12. In the weak coupling $I/W \leq 0.15$, the spectra show a pronounced peak at $\omega = 0$ which can be attributed to the quasiparticle peak in the single-particle spectra and thus signifying the metallic character. A small increase of the coupling apparently influences only the low energy part and it is reflected in a small shift of the peak. A somewhat similar behavior has been observed in the spectral function where the quasiparticle resonance is only slightly reduced. In the strong coupling regime, there is a drop of the spectral weight which further decreases as the coupling increases. The reduction of the low energy peak together with the readjustment of the spectral weight as the correlation increases is related to the change of the kinetic energy of charge carriers. This quantity can be calculated from Eq.(3.21) and is illustrated in the left panel inset of Fig.4.12. In the weak coupling regime, $K(\Omega)$ rapidly increases as a function of Ω to maximum value and again the spectral weight is independent of I/W. As anticipated, the spectral weight decreases and becomes linearly dependent on Ω in the higher coupling regime which is a restatement of the spectral weight suppression in the optical conductivity. This clearly suggest that the presence of non-local fluctuation responsible to the reduction of the kinetic energy of electron carrier.

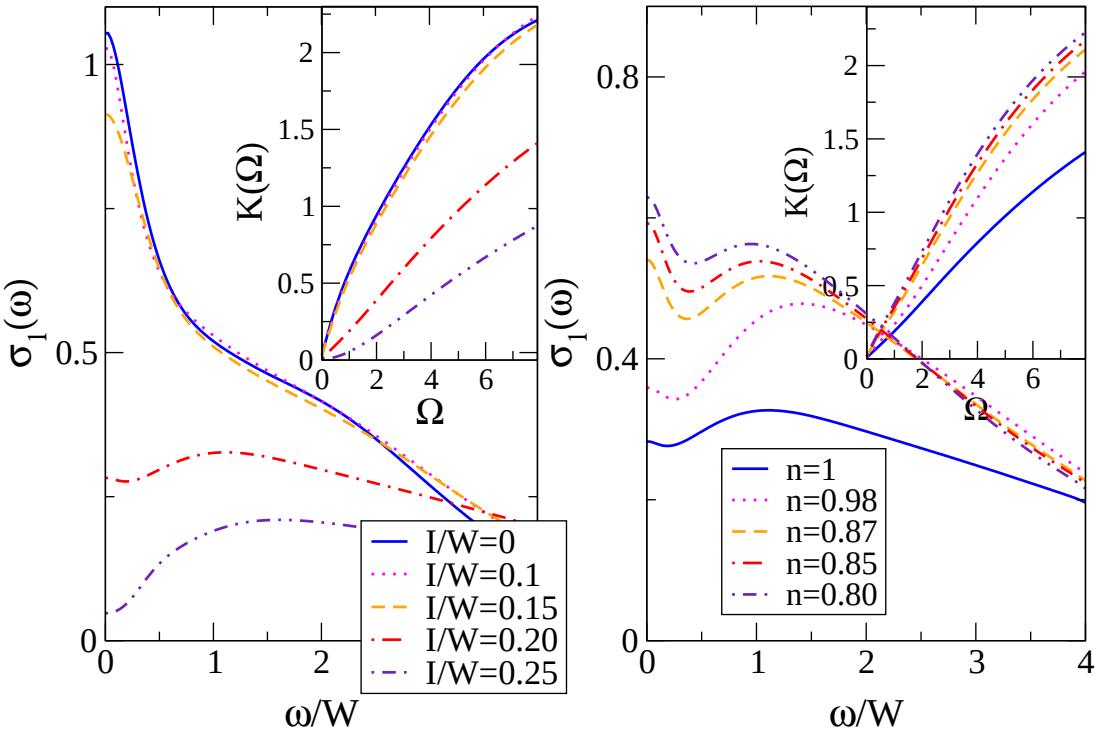

Figure 4.12: The frequency-dependent optical conductivity of the two-dimensional Hubbard model calculated by using the spectral function of EDMFT-QMC. In the left panel, we illustrate the optical spectra at half-filling for various values of I/W. The filling dependence of optical conductivity at $I/W = 0.20$ is depicted in the right panel. The insets show the integrated spectra according to Eq.(3.21).

The right panel of Fig.4.12 shows the optical conductivity for different band fillings which was calculated for $I/W = 0.2$ and $U/W = 1$. The increase of the low energy peak is visible even for the low doping concentration δ ($n = 1 - \delta$). In the high doping regime, the low energy spectra become enhanced and the high energy part displays the isosbestic point about $\omega \approx 2$ indicating the doping independence of the optical spectra. The increase of spectral weight thus indicates that the system again attain its metallic character. The same behavior is also reflected by the kinetic energy as demonstrated in the right panel inset of Fig.4.12. In general, the decay of the high energy optical spectra does not show $1/\omega^2$ behavior as usual for standard metals. This suggests that the necessary condition for the Fermi liquid behavior has been violated. In order to elucidate this behavior, let us investigate the scattering rate and the mass enhancements which can be derived from the generalized Drude model [60] expressed as

$$\sigma(\omega) = \frac{\omega_p^2}{4\pi} \frac{1}{\frac{1}{\tau(\omega)} - i\omega \frac{m^*(\omega)}{m_0}}. \tag{4.4}$$

It follows from this equation that the frequency-dependent scattering rate $\frac{1}{\tau(\omega)}$ and the mass enhancements $\frac{m^*(\omega)}{m_0}$ are associated with the real and the imaginary part of the optical conductivity

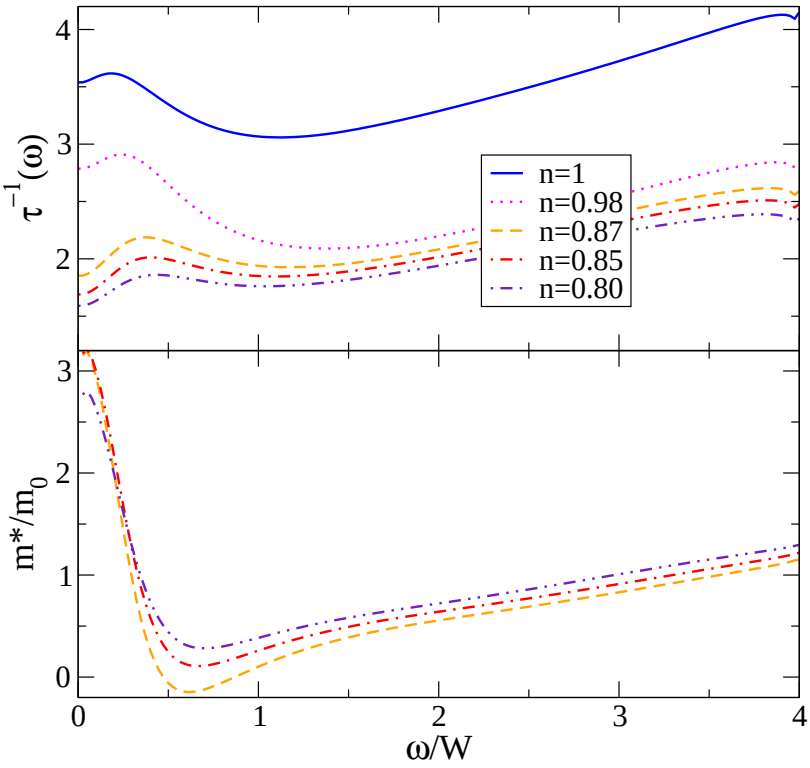

Figure 4.13: The frequency-dependent scattering rate $1/\tau(\omega)$ and the effective mass $\frac{m^*}{m_0}$ in the doped two-dimensional Hubbard model for $U/W = 1, I/W = 0.2$, $T/W = 0.1$ and for various band fillings.

$\sigma(\omega) = \sigma_1(\omega) + i\sigma_2(\omega)$ respectively. Explicitly, they are written as follows

$$\frac{1}{\tau(\omega)} = \frac{\omega_p^2}{4\pi}\mathrm{Re}\left(\frac{1}{\sigma(\omega)}\right), \tag{4.5}$$

and

$$\frac{m^*(\omega)}{m_0} = -\frac{\omega_p^2}{4\pi}\frac{1}{\omega}\mathrm{Im}\left(\frac{1}{\sigma(\omega)}\right). \tag{4.6}$$

It can be seen from Fig.4.13 that the scattering rate is most pronounced in the regime close to half-filling. When the system is doped, the spectral weight of $\tau^{-1}(\omega)$ decreases. The quadratic dependency on the frequency apparently is not observed in the calculated spectra. Instead, it exhibits the linear dependency with the suppression between $\omega = 1$ to $\omega = 2$. This is taken as the indication for the deviation of the Fermi liquid character and thus in accord with the observation in the optical conductivity and also in the self energy. The mass enhancement with the doping variations is shown in the lower panel of Fig.4.13. In general, one observes a sharp drop in the low energy which is followed by the linear increase at higher energy part. A careful examination shows that the low-energy spectral weight increases as the system approaches the half filling condition. At half-filling as well as for low doping concentrations, $\frac{m^*(\omega)}{m_0}$ collapses at low energies indicating the breakdown of the generalized Drude model.

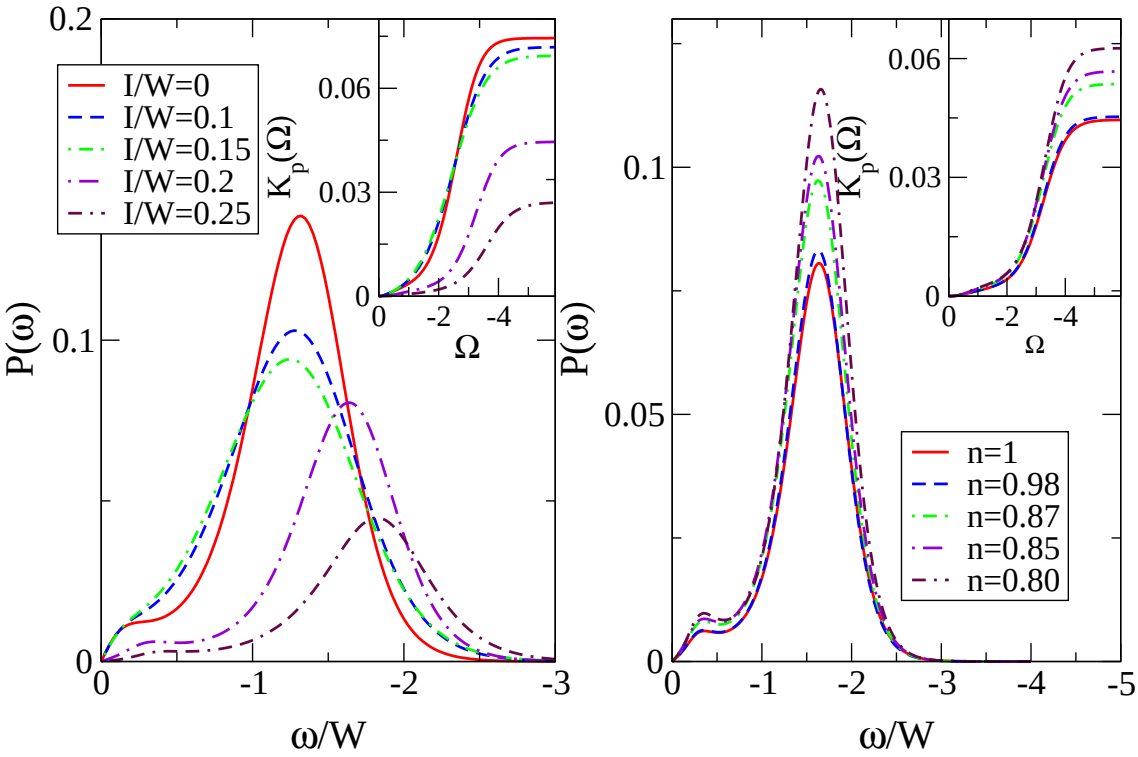

Figure 4.14: The two-particle spectral function of the two-dimensional Hubbard model for $U/W = 1$ and at temperature $T/W = 0.1$. Various curves in the left panel correspond to different interaction strengths I/W. The right panel shows the dependency on the electron occupancies at $I/W = 0.2$. The insets illustrate the integrated spectra according to Eq.(3.40).

Next, we investigate the two-particle spectral function of the 2D-Hubbard model at half-filling as depicted in the left panel of Fig.4.14. The particle-particle spectra exhibit a single broad peak that varies according to the spin exchange coupling. As expected, the most pronounced intensity occurs in the absence of spatial fluctuation. When the non-local interaction is weak the spectral weight decreases gradually but the position of peak remains unchanged. On the other hand, for higher coupling values there is a decrease of the spectral weight which is accompanied by a shift of peak to higher energies (away from zero). Thus one expects a gap opening at low energies (near to zero) if the coupling is further increased. Following the same argument in the single and doubly degenerate band discussed in the previous section, the pronounced intensity in the absence of the spin fluctuations in this respect can thus be attributed to the high probability to obtain two electrons. The increase of electronic correlation generated by the pronounced spatial fluctuation amounts to reduce the formation of the electron pair which is reflected in the two-particle spectra as small spectral weight or the formation of gap-like at low energies. This behavior is clearly comparable to the destruction of the quasiparticle weight in the single-particle spectral function (to easily understand this relation, see for example the results of the first order perturbation theory in the left panel of Fig.4.4). In addition to this, the high intensity clearly marks the high mobility of electrons in the system while the reduction of spectral weight

accompanied by the shift to higher energy corresponds to the increase of localisation character. This can be also seen from the integrated spectra depicted in the left inset of Fig.4.14 which shows a decrease of the spectral weight as I/W increases.

The influence of the hole doping in the two-particle spectra is depicted in the right panel of Fig. 4.14. As expected, the location of peak is roughly the same for all doping value. The effect of doping is clearly manifested in the enhancement of the spectral weight which becomes pronounced as the dopant concentration increases. This behavior suggests that the system attains its metallic character and thus reduces the influences of the spin fluctuation. This is further emphasized by the integrated spectra in the right inset of Fig.4.14 where the spectral weight also increases as a function of doping.

As an interesting question one might ask in this context is about identifying the presence of the pseudogap in the two-particle spectra as a function of the coupling or after the system is doped. From the results presented above, it is clear that the pseudogap of the single particle spectral function does not find its counterparts in the two particle spectra either at half-filling or for the hole-doped case. The reason for this absence can be easily understood by recalling the fact obtained within the first order approximation as well as the ladder approximation described in the previous section. It is shown that both methods deliver smooth line spectra for all coupling values as a result of the convolution procedure that washed out any small dips in the single-particle spectra. The same thus applies in this case and therefore based on this findings, the metallic phase with a single peak mainly at weak coupling, $0 \leq I/W \leq 0.15$ can be only distinguished with the one with the pseudogap at stronger interaction strength by observing the position of the peak as well as the intensity. The peak of the former at half-filling lies relatively close to the low energy regime, while the latter is shifted to higher energies. In the hole doped case, on the other hand one obtains an increase of spectral weight as a function of the dopant concentration without changes of position.

The relation of the calculated two-particle spectra with the $(\gamma, 2e)$ experiments can be again determined within the same formalism described before, namely by assuming the matrix elements to be independent of ω. It is easy to conceive that the calculated results remain relevant to the experiments at a fixed U and for the experimental situation discussed in Chapter 3.

CHAPTER 5

Metal-Insulator Transitions for The Anisotropic Two-Band Model

5.1 Introduction

In recent years a great deal of effort has been devoted to understand the underlying physical mechanisms behind many intriguing properties of the single layered ruthenates $Ca_{2-x}Sr_xRuO_4$ (CSRO). The interests in this material has been initiated by the discovery of unconventional superconductivity in Sr_2RuO_4 by Maeno and his collaborators [108]. Sr_2RuO_4 is the n=1 member of the Ruddlesden-Popper series of the layered perovskite which is isostructural with the high temperature superconductor compound $La_{2-x}Ba_xCuO_4$. As depicted in Fig.5.1, both compounds are highly two-dimensional (2D) systems with CuO_2 and RuO_2 layers for cuprate and ruthenates respectively. Due to their close structural similarity, it was generally believed that by understanding the physics of ruthenates in the normal as well as in the superconducting state might give insights into the nature of the high-T_c cuprates. Nevertheless, it was soon realized that Sr_2RuO_4 and cuprates show substantial differences in terms of the groundstate, the transition temperature, the structural distortion, and also the role of the orbital degrees of freedom.

The electronic structure calculation within the local density approximation (LDA) predicts Sr_2RuO_4 to be metallic. This is inferred from the projected DOS as well as from the calculated band structure of Fig.5.2 [109, 110, 111]. This result was obtained from LDA calculation in combination with linearized muffin-tin orbitals (LMTO) method. The partial density of states shows the contribution from the in-plane O-2p and Ru-4d at the Fermi energy. The states of apical O-2p as well as Sr$-4d$ on the other hand lie below or above the Fermi level. The projected DOS further indicates that the contribution of finite DOS at the Fermi energy is originally from t_{2g} Ru orbitals, xy, yz and xz that hybridizes with the in-plane or apical O-2p . The nature of the hybridization between each of t_{2g} orbitals and 2p orbitals is however different. The xy-orbital π-hybridizes with 2p orbitals of all 4 in-plane O-neighbors which is opposed to the degenerate xz,(yz) orbitals that π-hybridize only with 2 O neighbors along the x(y) axis. As a consequence,

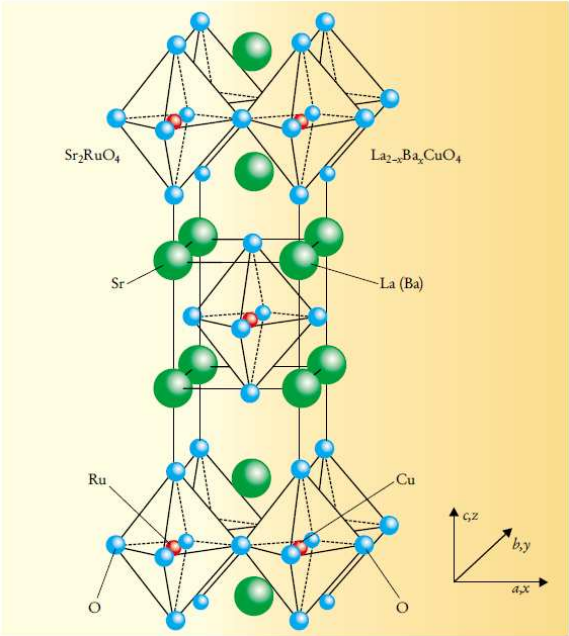

Figure 5.1: The layered perovskite ruthenates [108].

the bandwidth of degenerate orbitals is smaller than that of the xy orbital (see lower right of Fig.5.2). The existence of degenerate orbitals close to the Fermi energy and the fact that they have anistropic bandwidth makes the CSRO an interesting multiorbital system. This system thus allows for investigating the interplay of orbital degrees of freedom and the electronic correlation which is generally believe to be responsible for various intriguing properties.

The band structure of Sr_2RuO_4 within LDA can be described with three nonhybridizing tight binding bands as follows

$$\epsilon(\mathbf{k}) = -\epsilon_0 - 2t_x\cos(k_x) - 2t_y\cos(k_y) + 4t'\cos(k_x)\cos(k_y) \tag{5.1}$$

where (ϵ_0,t_x,t_y,t') being (0.50,0.44,0.44,-0.14), (0.24,0.31,0.045,0.01), (0.24,0.045,0.031,0.01) eV for xy, xy and yz respectively. The result of the Fermi surface from band structure calculation consists of a hole cylinder at the zone center and two electron cylinders with almost square cross-sections centered at the Γ point. The experimental results on the Fermi surface in Sr_2RuO_4 from de-Haas van Alphen effect fully corroborate the shape of the calculated Fermi surface.

The complete replacement of Sr^{2+} by smaller Ca^{2+}-ion leads to an antiferromagnetic insulator at $T_N = 110K$. The Sr_2RuO_4 is thus considered being in the proximity to Mott insulator. Since Ca and Sr are isoelectronic, this transition should not be attributed to the changes in the total carrier concentration but rather to the increase of the effective electron correlation strength relative to the bandwidth. The small Ca ion induces a non uniform structural distortion of the lattice parameter. The RuO_6 rotates and tilts in such a way that the Ru-Ru separation contracts while keeping the distance between Ru and O. This distortion also bends the Ru-O-Ru bond angle away from 180^o and as a result decreases the bandwidth of t_{2g}-orbitals. The CSRO system

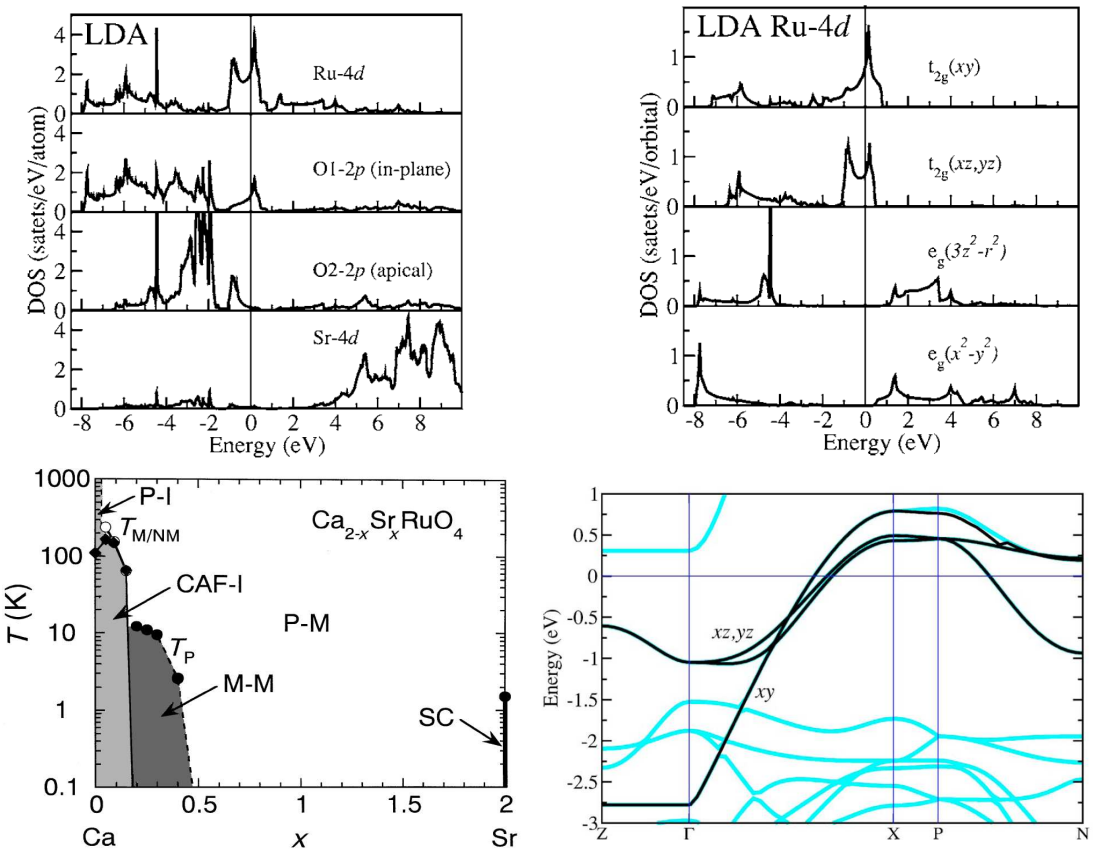

Figure 5.2: From left to right: Upper row shows the partial LDA DOS for Sr_2RuO_4 and Orbitally projected LDA Ru-4d DOS. Lower row, the phase diagram of $Ca_2Sr_xRuO_4$ and the calculated band structure along high symmetry directions in the energy window -3 to 1 eV. In the phase diagram P stands for paramagnetic, CAF for canted antiferromagnetic, M for magnetic, SC for superconducting phase, -M for metallic phase and -I for insulating phase. The metal/nonmetal transition temperature is denoted by $T_{M/NM}$ and T_{CAF} is the CAF transition temperature . These pictures are taken from Ref.[111, 112].

is thus an example of the bandwidth driven system which in contrast to doping driven high-T_c cuprates.

The calculated band structure of Ca_2RuO_4 (CRO) by means of the local spin density approximation (LSDA) [114] is illustrated in the left panel of Fig5.3. While LSDA correctly predicts the existence of AFM ordering and the competition between FM and AFM states in the *Pbca* phase, it is generally fail to describe the insulating phase. This failure hints on the importance of correlation in describing the physics of this system. The inclusion of electronic correlation in the first principle calculations leads to a correct description of the band structure of CRO. The right panel of Fig5.3 shows the result of LSDA+U [113] with the gap opening at the Fermi energy in the AFM phase.

The region between the two end member of $Ca_{2-x}Sr_xRuO_4$ is characterized by several

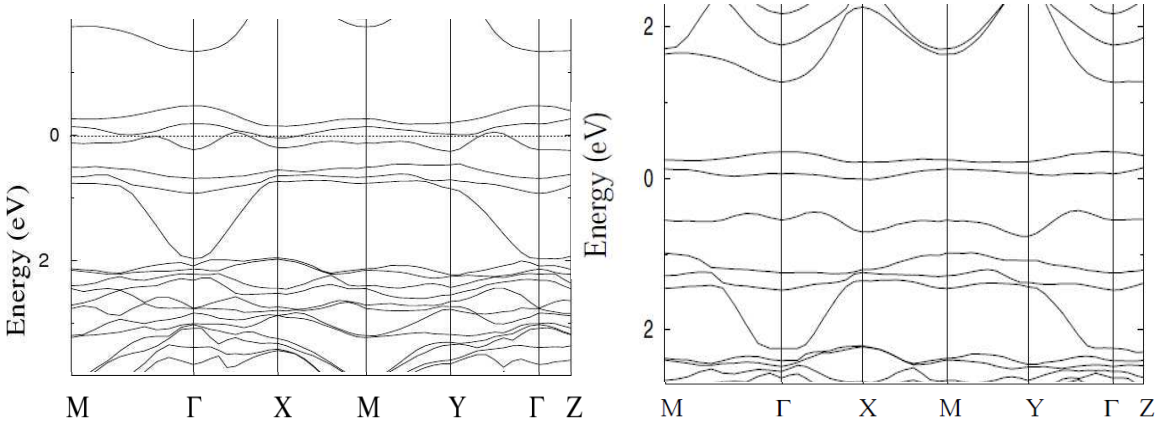

Figure 5.3: The band structure of Ca_2RuO_4 calculated by means of LDA (left panel) and LDA+U (right panel). From Ref.[113].

phases (see the phase diagram in the lower left panel of Fig.5.2) [112]. At low temperatures with rich Ca concentration $(0.09 < x \leq 0.2)$, the system remains in the antiferromagnetic Mott insulator and changes to paramagnetic metal at elevated temperature. As the system is doped with Sr concentrations $(0.2 < x < 0.5)$, the system becomes metallic at all temperatures with antiferromagnetic correlation at low temperature. Further increasing Sr concentration $(0.5 < x < 2)$, brings the system into paramagnetic metal.

In order to understand the physics of ruthenates particularly the origin of the rich phase diagram, it is thus essential to realize how the system evolves from the insulating to metallic phase. Extensive investigations have shown that the transition from insulating to metallic phase in this system is of a novel type owing to the new class of Mott transition. This is due to the fact that the interplay between the electron correlation and the orbital degrees of freedom gives rise to the coexistence of localized and itinerant character. This issue was brought to the forefront by Nakatsuji and Maeno who showed the evidence for a two-step metal insulator transition [115, 112]. Anisimov and coworkers subsequently [116] performed theoretical study of $Ca_{2-x}Sr_xRuO_4$ using a simplified two band system representing wide band xy and narrow band xz, yz. Their calculation neglected the details of structural distortion upon Ca doping. In order to treat the correlation properly, they employed LDA+DMFT in combination with non crossing approximation (NCA) as the impurity solver. For $U = 1.5eV$ they found that while the subbands (xz, yz) open a dip in the spectra, the other subband (xy) still exhibits a strong quasiparticle peak suggesting that the former is more correlated than the latter. This result, however, was questioned by Liebsch [117] who argued that two bands with only small bandwidth differences always undergo a common metal to insulator transition. His calculation was based on DMFT+quantum monte carlo (QMC) on two-band Hubbard model with tight binding lattice is replaced by Bethe DOS. In order to clarify this discrepancies, Koga *et al* [118, 119] performed the calculation using the same scheme as described by Liebsch. Instead of using QMC, they employed the exact diagonalization thus allowing for the inclusion of the full Hund's coupling which was not considered in the earlier

works. Their results suggested the possibility of two step transition which in agreement with the results of Anisimov. The subsequent works by several authors further clarify this issue and also support the possibility of an orbital dependent Mott transition [120, 121, 122, 123, 124]. These works also emphasize that the simplified two band Hubbard model that incorporates only Hund's coupling is sufficient to generate the orbitally dependent MIT. The MIT which is a result of the interplay between the bandwidth anisotropy and the correlation is then known as orbital-selective Mott transition (OSMT).

The experimental evidence for OSMT is, however, remain inconclusive. Based on the results of the transport properties of $Ca_{1.7}Sr_{0.3}RuO_4$ on ab plane and $c-$axis, Jin *et al.* [125] pointed out that the strong antiferromagnetic correlation develops along the $c-$direction suggesting a strong correlation in xz and yz bands. Their results thus support that of original work of Maeno. In contrast, based on ARPES measurement Wang [126] *et al.* showed that the topology of the Fermi surface of $x = 0.5$ remains nearly the same as that of $x = 2$. The main difference was observed only for xy band that changes from an electron like in Sr_2RuO_4 to a hole like in $Ca_{1.5}Sr_{0.5}RuO_4$. The results of the optical analysis [127] corroborate with that of ARPES. They emphasized that the xy band is more correlated than that xz and yz bands.

The recently published work of Neupane *et al.* [128] claimed to observe the orbital-selective Mott transition in the $Ca_{1.8}Sr_{0.2}RuO_4$ based on the results of ARPES. Their results also suggested that electrons in the wide band experience strong correlations for this band becomes insulating when narrow band remains metallic. This conclusion is drawn based on the fact that the Fermi surface of the xy band is absence after the doping. They further argued that the bandwidth difference does not play an essential role in the OSMT. This is supported from the results of slave boson mean field theory in the three-band Hubbard model with bandwidth ratio (W) 1:1:1 and 1:1:1.5 and two electrons per unit cell. It is found that the reduction of quasiparticle weight as a function of charge transfer in the isotropic and non-isotropic bandwidth is hardly different. Based on their results, they concluded that the OSMT is driven by the interplay of the interorbital carrier transfer, the superlattice potential and the orbital degrees of freedom.

In order to understand the physics of OSMT, we therefore discuss in this chapter the metal insulator transition in the two-band Hubbard model with a bandwidth anisotropy. In the first part of this chapter, DMFT method will be employed to study the single-particle excitation in the paramagnetic and antiferromagnetic phase. This will be followed by the results of the optical conductivity and the particle-particle excitation spectra. The second part of this chapter will again discuss the same paramagnetic phase of the Hubbard model. The center of investigation in this case is the influence of spin fluctuation in the anisotropic two-band system. To this end, EDMFT is employed to calculate the single-particle spectra, the spin susceptibility, the optical conductivity and the particle-particle spectra.

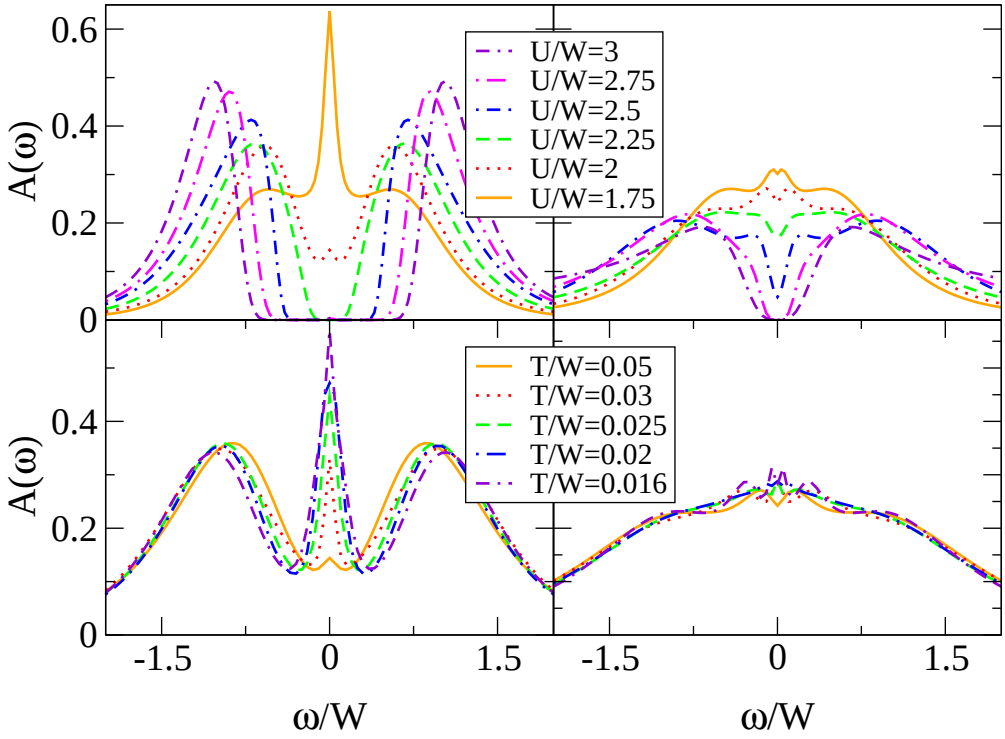

Figure 5.4: *Upper panel*: Orbitally resolved single-particle spectral function of the anisotropic Hubbard model for various values of onsite Coulomb interaction at $T/W = 0.05$. *Lower panel*: same as in the upper panel but for various temperature values and for $U/W = 2$. The left (right) panel corresponds to the narrow (wide) band.

5.2 DMFT Results

5.2.1 Single-Particle Properties of Paramagnetic Phase

Here we discuss the single-particle spectral function of the anisotropic two-band Hubbard model in the absence of a spontaneous symmetry breaking or without a spin polarization. To that end, we employ the model of Eq.(2.10) by considering the Ising like interactions and neglecting pair and exchange processes. In order to keep the model rotationally invariant, the relation $U = U' + 2J$, is employed [13] and thus by choosing $J = U/4$, one can easily determine the values of interband interaction U'. The semicircular density of states is employed as a non-interacting DOS in the self consistency loop, and the bandwidth ratio of narrow W_1 and wide band W_2 is set as $W_2 = 2W_1 = 2W$ with $W = 1$ The calculation is performed at finite temperatures and the time slices of QMC is set as $\Delta\tau \leq 0.5$. Unless otherwise stated, all DMFT results presented in this section as well as the following sections are obtained within the same model and with the same parameters as specified above.

For an overview of the orbital selective mott transition, we first discuss the single-particle spectral function at half-filling, as illustrated in Fig.5.4. When the interactions is weak $U/W < 2$, both bands clearly show the quasiparticle peak indicating the metallic behavior. A small increase

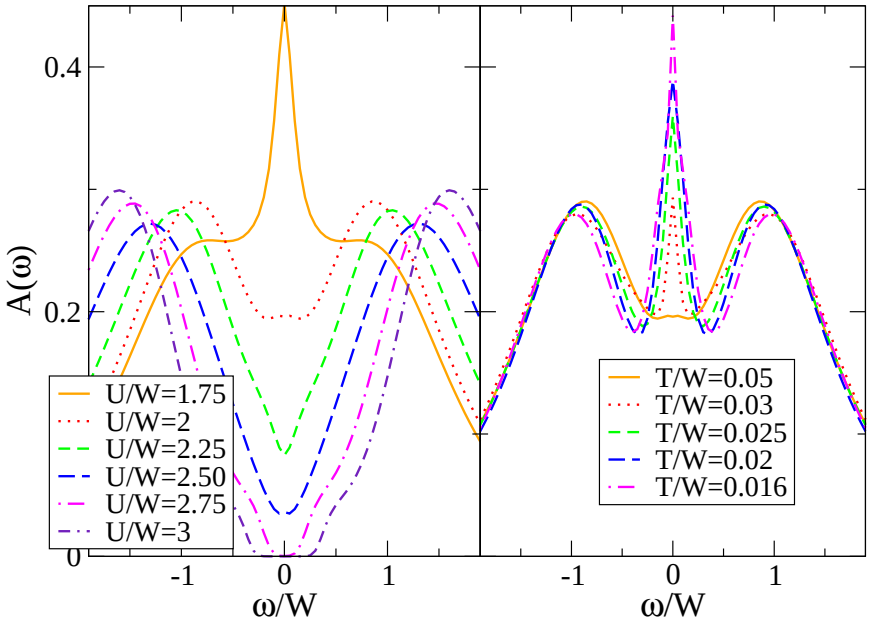

Figure 5.5: The left panel illustrates the total spectral function of the anisotropic two-band Hubbard model at half-filling for different U/W when $T/W = 0.05$. The right panel shows the results for different values of temperature at $U/W = 2$.

of the interaction significantly changes the metallic character of the narrow band which in contrast with the other one. While the latter still exhibits a resonance at $\omega = 0$, the former is now already in the pseudogap state. By further increasing the interaction coupling, both bands undergo independent transitions from the metallic into the insulating phase, i.e. the narrow band is followed by the other one. The narrow band has a larger gap than the wide band for all calculated Coulomb interaction values. This is a signature that the narrow band is more strongly correlated than the wide band. It is noteworthy to mention here that the underlying physics of the metallic phase of both bands is also governed by two different mechanisms. The strong quasiparticle peak in the narrow band is a clear indication of the Fermi liquid behavior. In this case the imaginary part of the self energy (not shown) can be approximated as $\mathrm{Im}\Sigma(\mathrm{i}\omega) \approx -\Gamma(\omega_\mathrm{n} + \ldots)$. In contrast, the self energy of the wide band shows appreciable deviations from Fermi liquid namely the imaginary part has a finite value at $\omega = 0$ and therefore the peak is not due to the quasiparticles but rather finite-lifetime excitation[122, 118, 123]. As the temperature is lowered, the pseudogap state in the spectra of the narrow band evolves continuously into quasiparticle states. In this case the imaginary part of the self energy can be again expressed in the Fermi liquid manner indicating a well-defined Fermi liquid state. The spectra of the wide band on the other hand do not show notable changes for all calculated temperature. The results of self energy also suggest a deviation from the Fermi liquid behavior.

The next figure (see Fig.5.5) is the results of the total spectra calculated as a function of the Coulomb interaction (left panel) and the temperature (right panel). Since off-diagonal terms are not considered in the calculation, these results are obtained from the summation of the diagonal

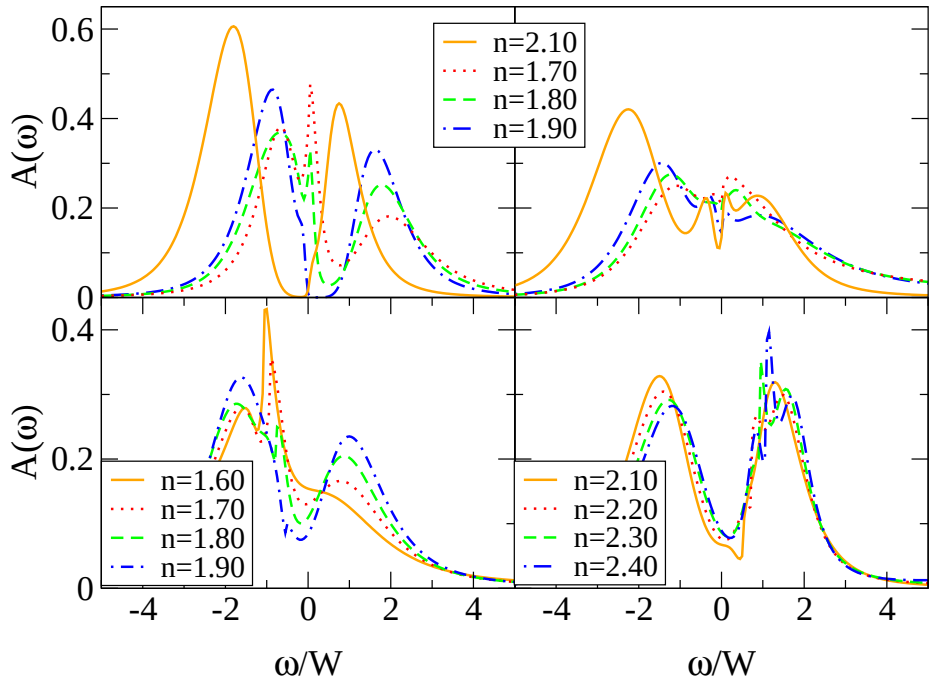

Figure 5.6: The upper-left and the upper-right panels are the orbitally resolved single-particle spectral function of the doped anisotropic Hubbard model in the narrow and the wide band. The spectra is obtained for $U/W = 2.5$ and $T/W = 0.05$. Within the same parameters value, the lower left panel displays the total spectral function for hole doping case while the lower right panel illustrates the results for electron doping.

terms, i.e. narrow and broad band. The behavior of the narrow band strongly influences the total spectra in the metallic phase. The same case also occurs as the temperature is lowered. However, the strong insulating character from the narrow band is not reflected in the insulating phase of the total spectra for it is washed out by that of the wide band. In this case, the imaginary part of a narrow band has been modified by that of wide band with a weak $1/\omega$ character. It is also important to mention that, while the qualitative behavior of the spectra is comparable with those of a two-band isotropic system, the present results have smaller critical coupling. This stems from the fact that the inclusion of Hund's coupling favors the insulating phase as the spin fluctuation increases in the system. This issue will be further elaborated in the next section when considering the influence of non-local fluctuations.

The effect of doping in the anisotropic bandwidth systems is demonstrated in Fig.5.6. The narrow band is apparently insensitive to a low doping concentration as it remains in the gapped-phase (see left panel of Fig.5.6), both for the hole and electron doped case. In contrast, the gap of the wide band is reduced to a pseudogap. As the dopant concentration increases, [1] the narrow band shows a resonance at low energies and it becomes more pronounced for $n = 1.70$. The wide band on the other hand remains in the pseudogap state. As in the half-filled case, the non

[1] In the present case only the results of the hole doping are presented but the same also occurs for the electron doped case.

fermi liquid behavior is robust in the wide band for both types of doping.

The total spectra of the hole and electron doped are displayed in the lower panel of Fig.5.6. Similar as in the half-filled case, the pronounced metallic phase at high doping is mainly due to the strong peak resonance of the narrow band. The pseudogap state on the other hand is clearly related to the presence of the small spectral weight in the wide band. These results are, in general, in a good agreement with the recently published works by Ref.[129].

5.2.2 Optical Conductivity and Particle-Particle Spectra

We now describe the optical conductivity of the anisotropic two-band system which is obtained following Eq.(3.16). Although it is possible to obtain the orbitally-resolved conductivity we will however only present the total conductivity considering that the optical spectroscopy is not orbitally resolved. The results of such calculations are depicted in Fig.5.7. For weak couplings, the conductivity shows a strong Drude peak for low energies which is the hallmark of the metallic character. As the energy increases, the spectral weight decays rapidly, suggesting that the low-energy excitations in the metallic phase of this system follows the standard Fermi liquid behavior As the coupling increases, the Drude weight is diminished indicating a suppression of the itinerant character of the electrons. This is particularly so for the coupling values of $2 \leq U/W \leq 2.5$, and it is usually considered as bad metal system. A further increase of the Coulomb interaction, leads to the formation of an optical gap at low energies indicating that the system is in the insulating phase.

The redistribution of the optical spectral weight as the correlation increases is clearly corresponds to the dynamics of the electron carriers. This can be investigated by inspecting the kinetic energy or the integrated spectra as depicted in the inset of Fig.5.7. For weak couplings, the spectra rapidly increase from $\omega = 0$ to maximum value. This suggests that the electron is effectively accelerated at all frequencies range. As interaction increases, the overall spectral weight is suppressed which corresponds to the reduction of the kinetic energy of the electron carriers. When the system in the insulating phase, the integrated spectra indicate the presence of an optical gap. In this case the acceleration of the electrons requires higher energy. Thus, it is now clear that the loss of electronic coherence can be attributed to the strong suppression of the kinetic energy

The influence of temperature on the optical conductivity is presented in the right panel of Fig.5.7, with the interaction parameter is set as $U/W = 2$. The most important effects of lowering the temperature is the rapid enhancement of the peak at $\omega/W = 0$. This indicates that the system gains its metallic character. In this respect, the resistivity as a function of the temperature $\rho(T) = 1/\sigma(\omega = 0)$ (not shown) has T^2 dependence which is characteristic of the Fermi liquid. It is also interesting to note that the thermodynamic instability occurs only for the low-energy part of the spectra while the high energy part is unaffected for all the calculated temperature values. Following the previously mentioned argument, the enhancement of metallic character corresponds to the increase of kinetic energy. This is indeed observed in the integrated

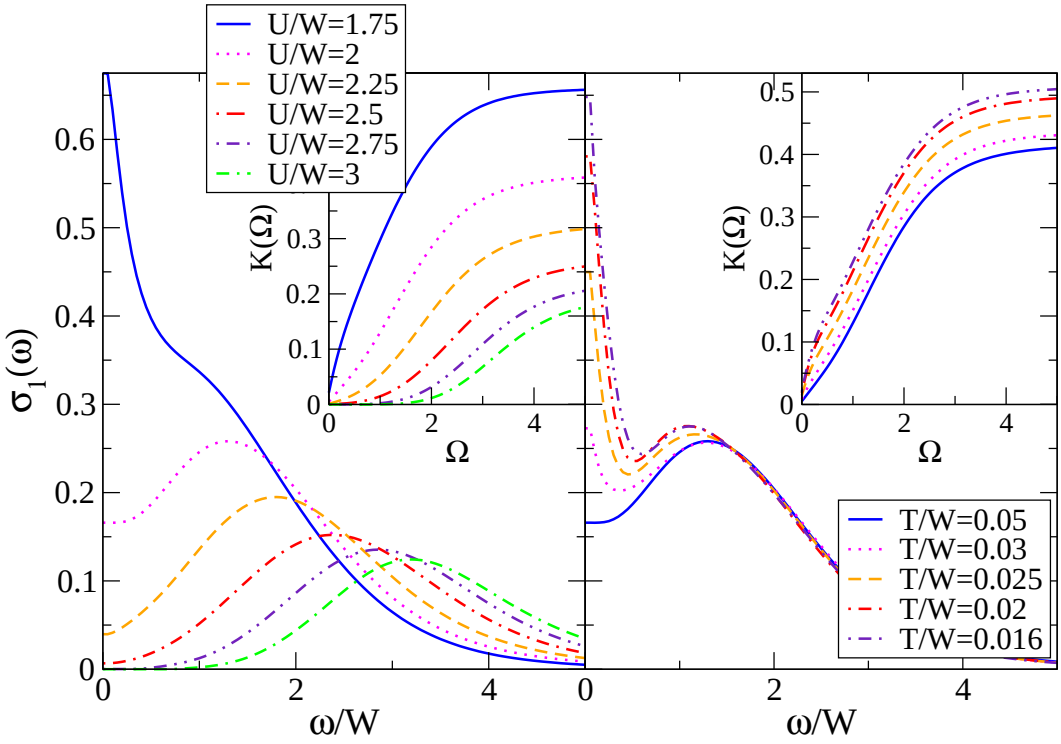

Figure 5.7: The left panel shows the optical conductivity $\sigma_1(\omega)$ of the anisotropic two-band Hubbard model at half-filling for various values of the Coulomb interaction U/W when $T/W = 0.05$. The temperature-dependent optical conductivity at $U/W = 2$ is demonstrated in the right panel. The insets show the frequency-dependent spectral weight $K(\Omega)$ as a function of Ω.

spectra displayed in the inset of Fig.5.7. Here the spectral weight is shifted to higher energies as the temperature is lowered.

As is already pointed out, mass enhancement and scattering rate can be deduced directly from the optical conductivity data. This is done following the lines described in Chapter 4, where both quantities are derived from the extended Drude model. The results of such calculations are presented in Fig.5.8 which displays the scattering rate (upper plane) and the mass enhancement (lower plane). It is clear from the figure that the system at the verge of the metal insulator transition bears the highest scattering rate. When the temperature is lowered, there is a reduction at low energies which can be approximated by $a + \omega^2$ dependence. The quadratic dependence of the spectra is another indication that at low temperatures the low excitation can be described within the Fermi liquid theory.

The enhancement of the mass at lower temperatures is also described nicely within the extended Drude model. The influence of temperatures is clearly identified at low energies where the effective mass decreases as a function of temperature. The higher energies spectra on the other hand shows hardly any difference. This is clearly a reminiscence of the high energy optical spectra and which emphasizes the previous finding that only the low energy part is strongly influenced by temperatures. The extended Drude model however fails to describe the effective

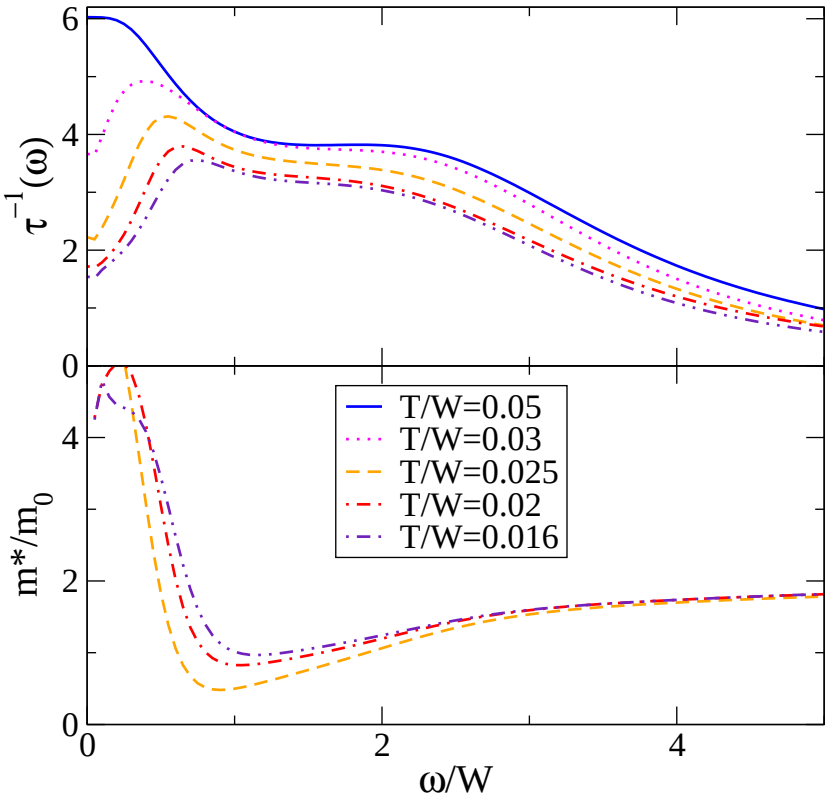

Figure 5.8: The scattering rate (upper panel) and the mass enhancement (lower panel) as a function of ω/W of the anisotropic two-band Hubbard model at half-filling for $U/W = 2$ and different temperature values.

mass at relatively high temperature $T/W = 0.03$ and $T/W = 0.05$. This can be understood using the fact that in this regime there is a pronounced suppression of Drude weight that makes them deviate from the Fermi liquid behavior. This also further explain the validity range of the extended Drude model.

Having obtained the optical conductivity spectra, one can also deduce the spectra of the Electron Energy Loss Spectroscopy (EELS) which is nothing but the inverse of the imaginary part of the dielectric function

$$I_\epsilon(\omega) = -\mathrm{Im}\frac{1}{\epsilon(\omega)} \tag{5.2}$$

where $\epsilon(\omega)$ is the dielectric function in the optical limit ($\mathbf{q} \to 0$)

$$\epsilon(\omega) = 1 + \frac{4\pi i\sigma(\omega)}{\omega}. \tag{5.3}$$

The results of such calculation at half-filling for various U/W and T/W are illustrated in the Fig.5.9, where upper and lower panel demonstrate the results for different values of U/W and for various temperature T/W. The present results are composed of single peak which is associated with the interband transition, namely the transition from the lower band to the quasiparticle resonance. The metallic phase at weak coupling values and at the low temperatures is character-

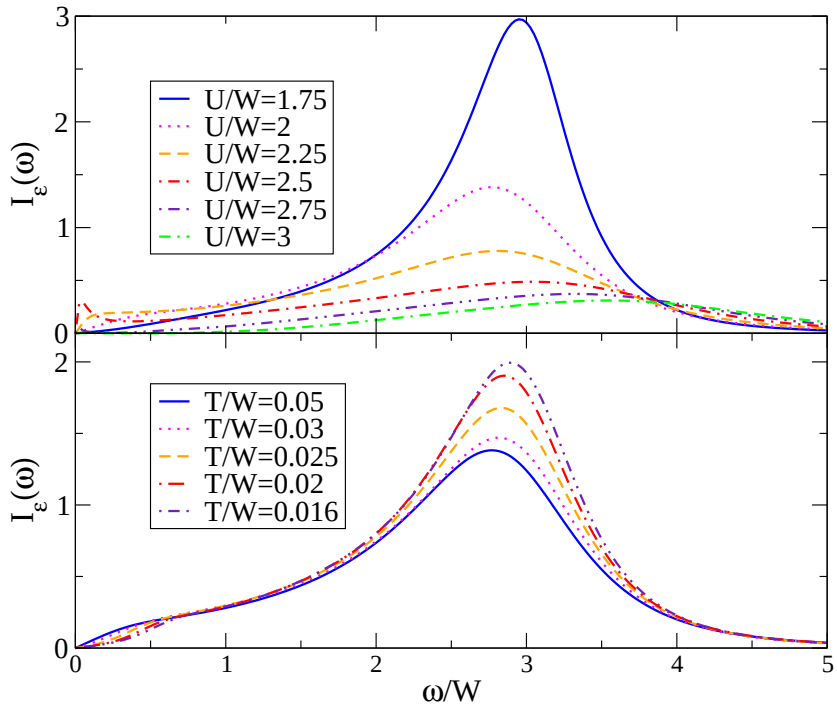

Figure 5.9: The spectra of the Electron Energy Loss Spectroscopy (EELS) of the anisotropic two-band Hubbard model at half-filling, calculated according to Eq.(5.2). The results in the upper panel are for various values of Coulomb interaction when $T/W = 0.05$ while the lower panel are for various temperature values at $U/W = 2$.

ized by a broad band with pronounced intensity. As the coupling increases, notable changes in the spectra is the weight suppression as well as the shift to the higher energies. In the insulating phase, the EELS intensity shows again a gap at low energies which is a counterpart of the low-energy gap of the optical conductivity (see Fig.5.7). We note here that the gap is a restatement of the vanishing of the imaginary part of the dielectric function at low-energy (not shown). When the temperature is lowered at $U/W = 2$, one observes an increase of EELS spectral intensity which is comparable with the low-energy enhancement in the optical conductivity. The changes of intensity and its relation to the kinetic energy of electron can be again understood using the argument mentioned above.

The influence of the hole and the electron doping in the optical conductivity is demonstrated in Fig.5.10. As expected, the low-energy weight increases as the number of holes in the system increases and it is accompanied by the shift of the high energy peaks to lower energies. The number of the dopants used in the present calculation is, however, not sufficient to generate a strong Drude peak in the metallic state. Similarly to the hole doped case, as the electron number in the system increases, the low-energy part rises gradually. In addition to this, one observes the shift in the upper energy and also the isosbestic point at $\omega \approx 2.8$. The above results thus suggest that the system remains close to the bad metallic phase which is clearly manifested by a pronounced scattering rate (not shown) obtained from the extended Drude model. The effective

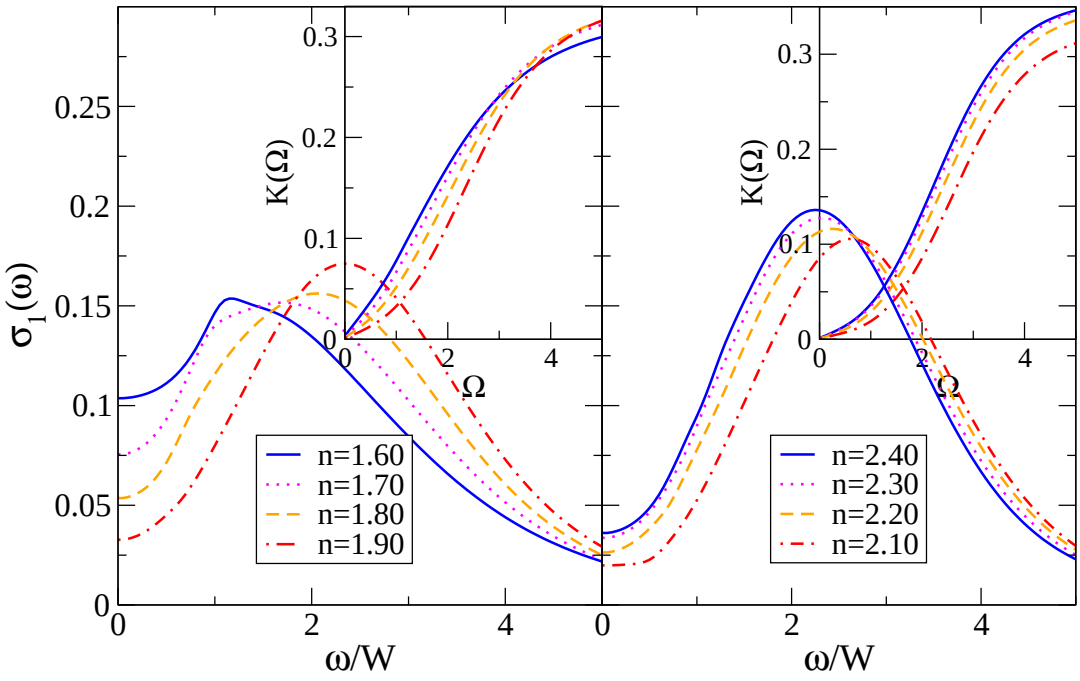

Figure 5.10: Optical conductivity of the anisotropic two-band Hubbard model in the hole- (left panel) and electron-doped (right panel) when $U/W = 2.5$ and $T/W = 0.05$. The insets show the optical integral.

mass on the other hand can not be described within this model. In this case the imaginary part of the conductivity obtain negative values at low energies.

We now turn to the dynamical pair-correlation $P(\omega)$ at half-filling as depicted in Fig.5.11. The general features of the spectra remain the same as before namely a single peak like structure with the intensity varies according to the coupling interaction. In the weak coupling, the spectra are composed of pronounced peak that decreases as the interaction U/W increases. This adjustments can be associated with that of the single-particle spectra, namely the reduction of the quasiparticle weight and the shift of the Hubbard band. In the strong coupling regime , the low-energy part of the two-particle excitations are depleted and transferred to higher energies and it is accompanied by a suppression of the spectral weight. The shift of the peak to higher energies result in gap formation which can be attributed to the distance of Hubbard bands in the single-particle spectra. This low-energy gap is a signature of the insulating phase from the perspective of two particles. The changes of spectral behavior as the interaction increases are closely related to the variation of the double occupancy in the system, which in the case of degenerate orbital corresponds to the contribution of the interband and the intra-band (see sum rule of Eq.(3.52)). In this case, the double occupancy $\langle n_\uparrow n_\downarrow \rangle$ of total band (not shown) decreases as the interaction increases which is in a good agreement with the integrated spectra depicted in the inset of Fig.5.11. The same trends are observed for intraband. The double occupancy in the interband on the other hand fluctuates for all coupling interactions. In addition, we also observe that the double occupancy in the narrow band is quantitatively smaller thus in line with the behavior of the

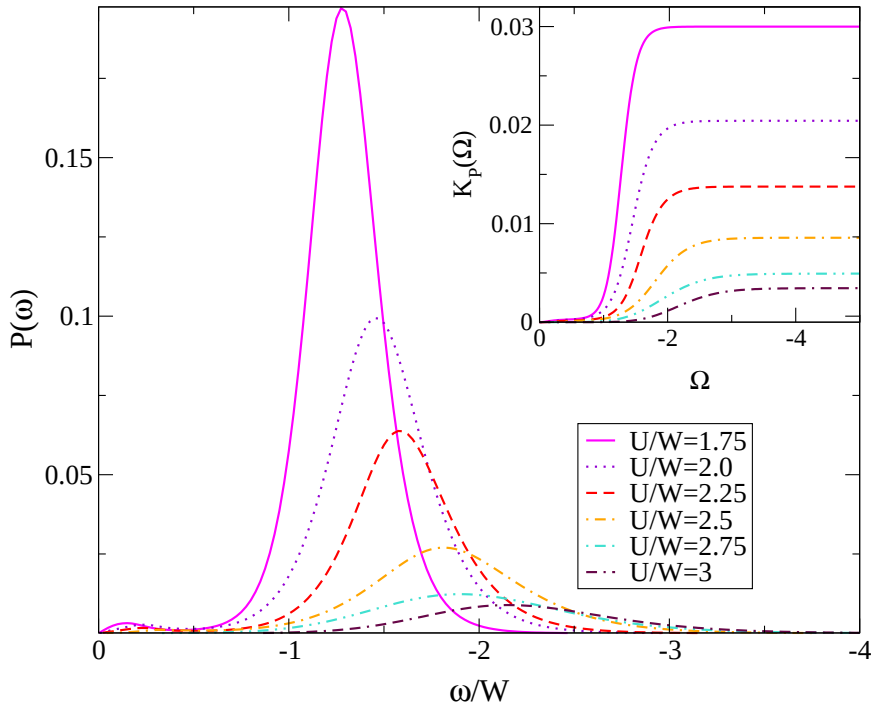

Figure 5.11: The pair excitation of the anisotropic two-band Hubbard system at half-filling within DMFT-QMC for $T/W = 0.05$ and various values of onsite Coulomb interaction. The inset illustrates the integrated spectra as a function of Ω.

single-particle spectral function described above. As a comparison, we note here that the double occupancy in the isotropic two-band Hubbard model fluctuates for all U/W although the total double occupancy eventually decreases as the coupling increases. The discrepancy of the fluctuation of double occupancy in these two systems is believed to be linked to the interplay between orbital degrees of freedom and strong correlation. In the isotropic system, the effect of bandwidth is relatively small and thus the site occupation is strongly dictated by U/W. In contrast the interplay of the bandwidth anisotropy and the strong interaction (that leads to the different effective interaction on each bands) dominantly influences the electrons in the intra-band. It is interesting to note that the overall behavior of the particle-particle spectra at half-filling has its counterpart in the particle-hole excitation as obtained by the imaginary part of the inverse dielectric function (see Fig.5.9). The main difference is the shift of the peak of EELS which is less pronounced than that for the particle-particle case.

The influence of the hole and the electron doping in the two-particle spectral function is demonstrated in Fig.5.12. As expected, the peak is located at the order of U/W and its weight slightly changes as the dopant concentration increases. The lowest intensity is observed for systems with occupancy close to half-filling. Upon doping, the spectra of two particles build up and becomes maximal in the overdoped case signaling the increase of double occupancy in the system. This is supported by the integrated spectra as depicted in the insets of Fig.5.12 for the hole as well as for the electron doped case.

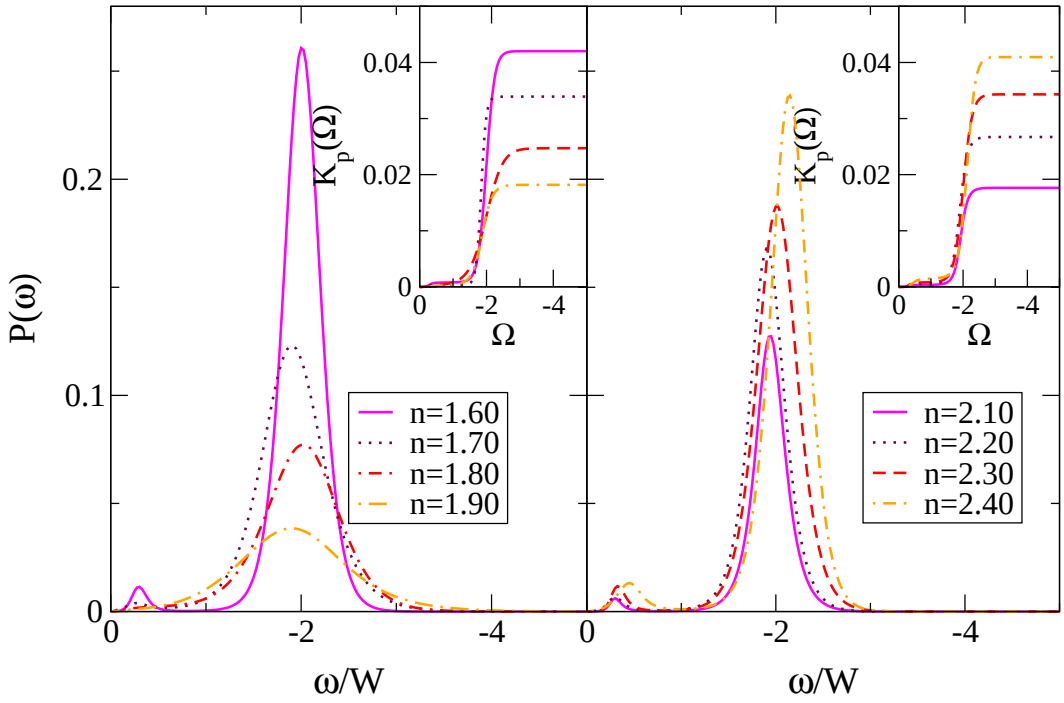

Figure 5.12: The same as in Fig.5.11 with the same notation. Here however the two-particle spectra are calculated for hole- (left panel) and electron-doped (right panel) for $T/W = 0.05$, $U/W = 2.5$. The insets show the result of the integrated spectra.

5.2.3 Antiferromagnetic Phase

While the coexistence of the itinerant and the localized character is possible in the paramagnetic phase of the anisotropic two-band system, the possibility of OSMT remains unclear in the antiferromagnetic phase. We, therefore allow for the antiferromagnetic ordering in our calculations and investigate the magnetic properties as well as the possibility of selective Mott transition. To this end, the same model specified above is employed together with the DMFT method that is modified to accommodate the Neel ordering. The left panel of Figure.5.13 shows the staggered magnetization $m_\alpha = \langle n_{\alpha\uparrow} - n_{\alpha\downarrow} \rangle$ of the narrow (m_1) and wide band (m_2) as a function of temperature for two values of the Coulomb interaction. The magnetization of the narrow band is clearly more pronounced for all values of U/W. As the temperature increases, the magnetization of each band gets smaller and eventually becomes approximately equal around the critical temperature. This then suggests that each band undergoes a transition into antiferromagnetically ordered phase at the same critical temperature. From the figure one also observes the increase of the magnetization as a function of U/W. Thus, in the strong coupling regime in which the magnetization has fully developed, the anisotropic two-band system can be also mapped onto the Heisenberg model. By performing the same calculation for different values of U/W and T/W we then construct the $T - U$ phase diagram as depicted in the right panel of Fig.5.13. The diamond shape scattered in the figure indicates the location where the calculation have actually been performed. Based on this points, the shaded area is then constructed to make a clear sep-

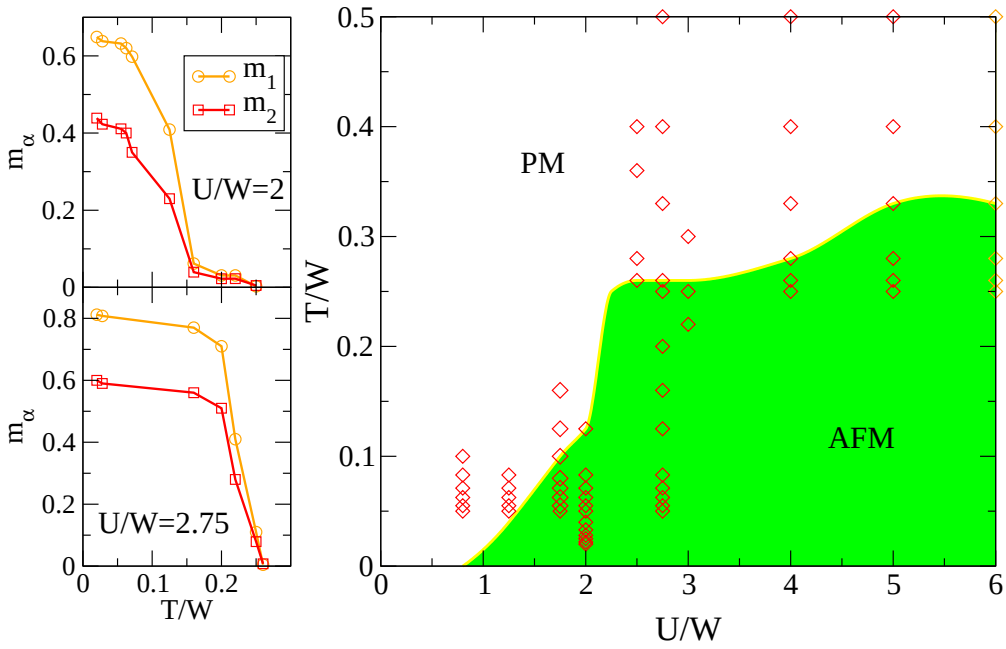

Figure 5.13: Left panels illustrate the staggered magnetization m_α as a function of temperature T/W in the anisotropic two-band Hubbard model at half-filling. m_1 denotes the magnetization for narrow band while the other for broad band. The right panel displays the $T-U$ phase diagram consisting of antiferromagnetic (AFM) and paramagnetic phase (PM). The points denote the parameter values where the calculations were done.

aration between the antiferromagnetic and the paramagnetic phase. Clearly, at half-filling, the antiferromagnetically ordered state exists at low temperatures which occur even for small U/W. The line in the phase diagram indicates that both bands undergo a common transition to the antiferromagnetic phase as the coupling is increased. The same is also observed as a function of temperature. This suggests that the bandwidth anisotropy does not play a role in determining the nature of magnetic phase transition in the two-band system.

To make definitive statement on the nature of Mott transition in this phase, it is instructive to calculate the single particle excitations which we illustrate in Figure 5.14. The figures show orbital- and spin-resolved spectral function in the particle-hole symmetry calculated for various values of the Coulomb interaction at $T/W = 0.05$. The upper left and lower left panels illustrate the results of the spin-up and the spin-down respectively and the same also in the right panel for a wide band. The most notable feature of the spectra in the weak coupling $U/W = 1.75$ is the appearance of the pseudogap at the Fermi energy. In addition, the difference between the total densities of the spin-up and spin-down is also clearly apparent. As the interaction increases, the spectra exhibit an antiferromagnetic gap at $\omega = 0$. Its width becomes larger as a function of the coupling interaction. The appearance of the gap in the spectra is related to the vanishing of the imaginary part of the single-particle self energy particularly for $\omega \to 0$. Based on the phase diagram, we expect that the transition from the pseudogap to the gapped phase occurs continuously. The presence of the pseudogap in the weak coupling with finite magnetization indicate that mag-

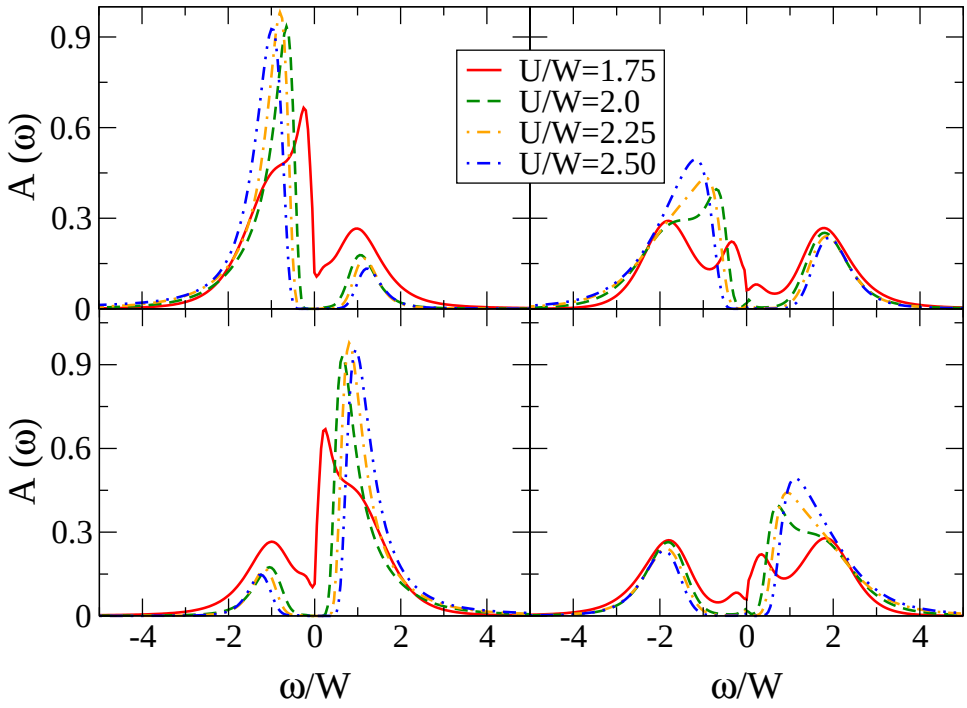

Figure 5.14: The spin-resolved single particle spectral function of the half-filled anisotropic Hubbard model in the antiferromagnetically ordered phase for various values of onsite Coulomb interaction and for $T/W = 0.05$. The left panels up (down) display the spectra of narrow band for spin up (spin down) while the right panels show the spectra of the wide band.

netic ordering is developed earlier than the metal insulator transition. This occurs particularly for $1.5 \leq U/W \leq 1.75$ where the single particle spectra (not shown) also show a pseudogap with non-negligible magnetization. This is in accord with the proposal of Slater that describes the metal insulator transition as a consequence of the broken magnetic symmetry. In addition to the above points, we also observe that the qualitative behavior of the spectra of both bands remains the same for higher couplings. This stems from the fact that the imaginary part becomes very large and thus completely smear out the structure of the spectra. In this regime, one also observes the saturation of magnetization (cf. left panel of Fig.5.13).

The results of the single particle spectral function and the phase diagram described above has clearly indicated the absence of a selective Mott transition in the antiferromagnetic phase. It is however interesting to discuss some evidences that can be used to identify the role of the bandwidth anisotropy. This can be seen for example in the staggered magnetization as well as from the single particle spectra. The spectra for the narrow band case (see Fig.5.14) show a satellite peak for all calculated U/W which can be attributed to the pronounced magnetic ordering for each sub lattice. In contrast, the wide band shows a “band like” structure and its intensity is also suppressed compared to the other band. This difference is comparable with the one in staggered magnetization where the narrow band also shows a larger value than the broad band for all calculated U/W. This observation implies that the effective Coulomb interaction

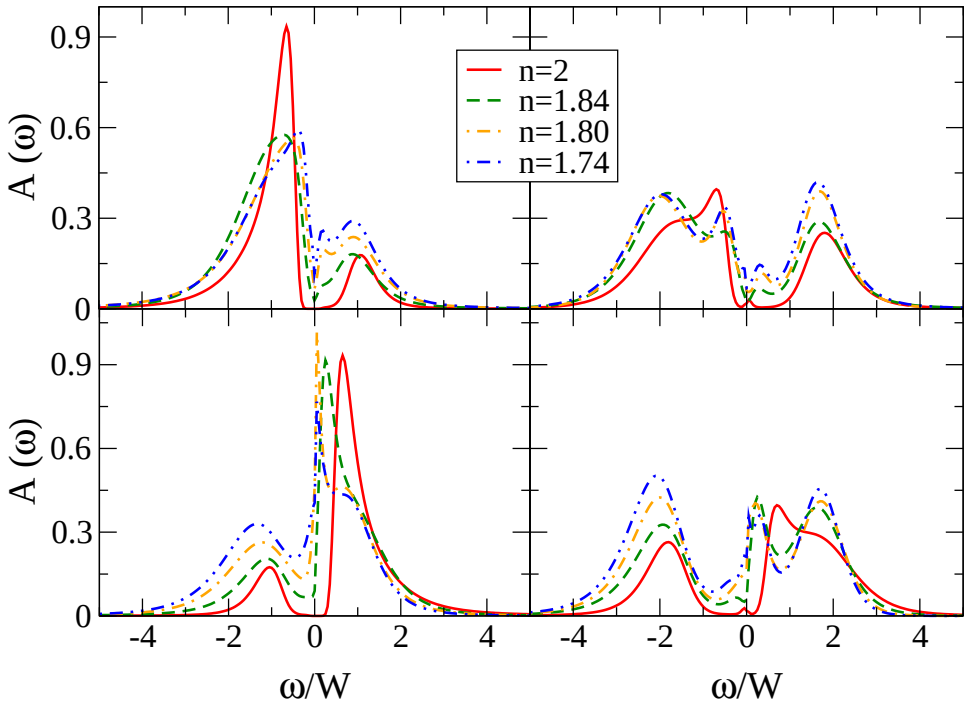

Figure 5.15: The upper(lower) left panel corresponds to the spin-up (down) spectral function of the narrow band for $U/W = 2$, $T/W = 0.05$ and for different band fillings. The right panels show the results of the wide band.

is different in both bands and it is related to the presence of a bandwidth anisotropy. Recently, the authors of Ref.[130] have investigated the magnetization of the anisotropic two-band system at and off half-filling. They employed DMFT combined with continuous time quantum monte carlo (CTQMC) as impurity solver. They pointed out that the magnetization of the narrow band is always larger than that the other one which is in line with the above presented results. Based on this data they argued that the bandwidth anisotropy does not induce selective Mott transition as in the paramagnetic phase.

The influence dopant concentration in the antiferromagnetic phase is illustrated in Fig.5.15. The results are obtained for $U/W = 2$ within the same temperature as specified above. The antiferromagnetic gap reduces to pseudogap as the hole concentration increases. For low doping, both bands undergo a simultaneous transition from the gapped phase to the pseudogap state indicating the absence of the orbital-selective Mott transition. For higher doping, the spin down channel increases rapidly showing the quasiparticle-like peak. The spin up on the other hand exhibits a weak resonance. We note here that the magnetization (not shown) also decreases as the doping increases. Within the same temperature as employed here but for different interaction parameters, Ref.[130] indicates the presence of an orbital-selective Mott transition by hole doping at the chemical potential $\mu/\mu_h \approx 0.67$.

In the next figure, we discuss the evolution of the spectral function under the influence of the external magnetic field $h = 0.1$. The results are obtained within the same parameter values

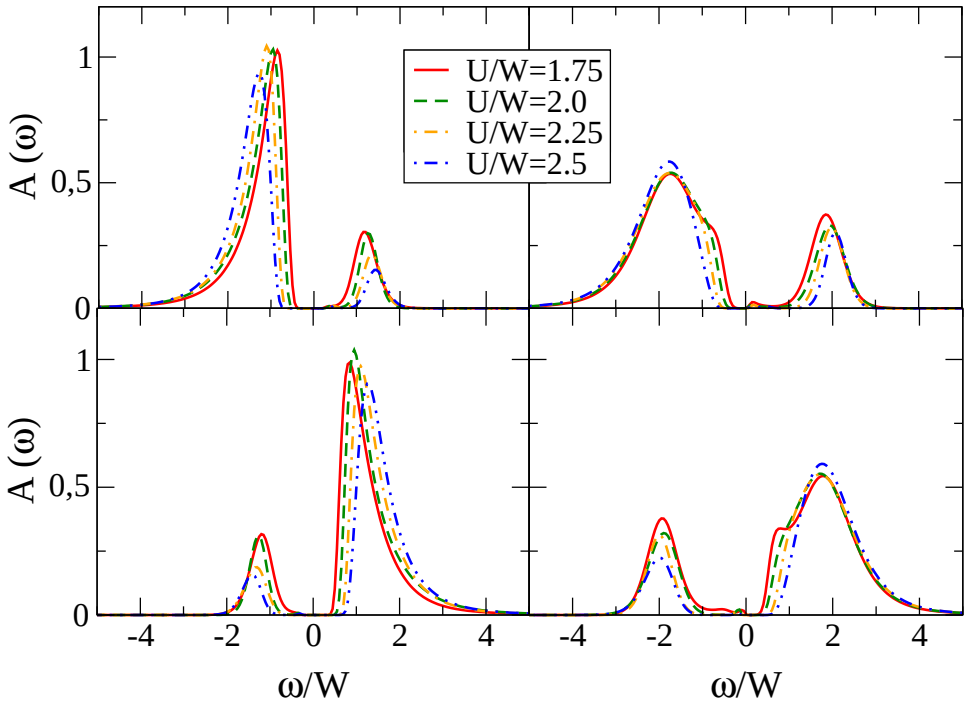

Figure 5.16: The same as in Fig.5.14, however in this case with finite external field $h = 0.1$.

specified above. Clearly, the presence of the external magnetic field induces the formation of magnetic ordering. This is also manifested in the values of staggered magnetization (not shown) which in general become larger than those in the absence of a magnetic field. In addition to that, the system becomes insulating as indicated by the single particle excitations composed of antiferromagnetic gap for all calculated U/W. The increase of the coupling generally does not induce any qualitative changes in the spectra which can be understood following the argument pointed above. The most interesting behavior is that the spectral weight of the narrow and the wide band remains different signaling that the pertinent feature of the narrow and the wide band remains unchanged.

Optical Conductivity and Particle-Particle Spectra

We now discuss the optical conductivity of the antiferromagnetic phase at half filling which is depicted in Fig.5.17. These spectra are obtained by evaluating Eq.(3.29) together with the single particle spectral function of Fig.5.15. In the weak coupling, there is a finite conductivity at $\omega/W = 0$ which can be associated with the pseudogap in the single particle spectra and signal of the metallic character. As interaction increases, the Drude weight vanishes and the conductivity is shifted to higher energies. Simultaneously, the low-energy part exhibits an optical gap which becomes larger as a function of couplings. This clearly indicates that the system becomes insulating. This low-energy gap is also demonstrated by the kinetic energy at strong coupling as depicted in the inset of Fig.5.17 and it is accompanied by the decrease of spectral

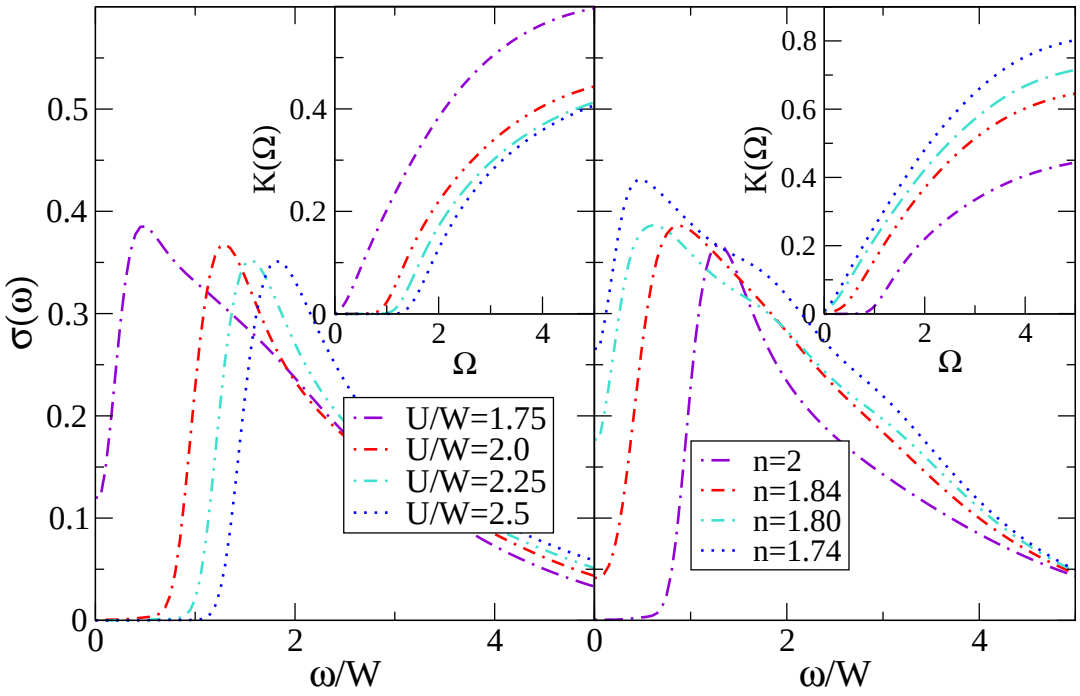

Figure 5.17: Optical conductivity for the antiferromagnetically ordered phase of the half-filled anisotropic Hubbard model. The left panel shows the results for various values of onsite Coulomb interaction at $T/W = 0.05$ while the right panel for different band occupations at $U/W = 2$. The insets show the integrated spectra $K(\Omega)$ as a function of Ω.

weight. For $U > W$, following Ref.[65], it can be shown that the behavior of $\omega.\sigma(\omega)$ could be described by a Lorentzian function as $\omega.\sigma(\omega) \propto 1/((\omega - \omega_0) + \gamma^2)$ where $\omega_0 = Um_s$ and γ is a quantity that is introduced to take care the finite imaginary part of the single particle self energy. By taking $m_s = 1$ it can be easily shown that the sharp resonance occurs at $\omega \approx U$. We mention here that the peak of the optical conductivity lies approximately in the order of U/W is a signal of the conductivity of Mott insulating type.

Away from half-filling, the optical gap becomes narrow and the Drude weight rises gradually as the dopant concentration increases, signaling that the system has attained a metallic character. In the highly doped case, the spectra do not indicate a pronounced Drude peak as usually observed for a good metal. This stems from the fact that each band as well as spin in the single particle spectra (cf.5.15) exhibits a different behavior, i.e. the low-energy peak, pseudogap. Although direct comparison to the experimental results of the optical conductivity of antiferromagnetic ruthenates Ca_2RuO_4 is relatively difficult, the present results however have given an insights to the nature of Mott transition in the antiferromagnetic phase of anisotropic two-band system. The correlation is apparently important to generate the insulating phase at anisotropic orbitally-degenerate system as is also indicated by the LSDA results. The interplay of orbital and the strong coupling at antiferromagnetic phase, however, does not induce the OSMT both at half-filling and hole/electron doped case.

5.3 The Influence of Spin Fluctuation

5.3.1 Extended Two-Band Hubbard Model

In the previous chapter, it has been shown that EDMFT offers a systematic way to incorporate the non-local contributions by considering the spin fluctuations in the Hubbard Hamiltonian. The application of the method to the two-dimensional Hubbard model points out an interesting relationship between the spatial fluctuation and the formation of pseudogap in the single-particle spectral function. The results suggest that the mechanism of MIT in this system is related to the strong electronic correlation and thus rule out the weak coupling picture. Recalling the facts that the ruthenates compound is composed of two dimensional ruthenates RuO_2 layer, one expects that the spatial fluctuations also contribute to the electronic properties of this system. In order to elucidate this issue, we revisit in this section the anisotropic two-band Hubbard model in the paramagnetic phase within the framework of EDMFT. Similar to what have been previously done in the single band Hubbard model, the non-local contributions are incorporated in the intersite spin interaction. The Hamiltonian of the two band-Hubbard model with spin fluctuations reads

$$\begin{aligned} H = & -\sum_{ij\alpha\sigma} t_{ij\alpha} c^{\dagger}_{i\alpha\sigma} c_{i\alpha\sigma} + U \sum_{i\alpha} n_{i\alpha\uparrow} n_{i\alpha\downarrow} \\ & + \sum_{i\sigma\sigma'} (U' - \delta_{\sigma\sigma'} J) n_{i1\sigma} n_{i2\sigma'} + \sum_{ij\alpha} I_{ij\alpha} \mathbf{S}_{i\alpha} . \mathbf{S}_{j\alpha} \end{aligned} \tag{5.4}$$

The notation in the above Hamiltonian follows that described in Eq.(2.10). The last term is the intersite spin interaction with exchange coupling $I_{ij\alpha}$. that takes account the non-local fluctuations. The single site action of Hamiltonian (5.4) is then solved by means of QMC that incorporates the boson degrees of freedom. Unless otherwise stated, the parameters of calculation are as follows: bandwidth $W = 1$, $T/W = 0.1$, and $U/W = 1.5$. In what follows we will discuss the characteristic of the dynamical spin susceptibility, the single-particle spectral function, optical conductivity and the pair spectral function.

5.3.2 Magnetic Susceptibility

In order to easily distinguish the influence of each interaction parameter in the magnetic spin susceptibility of the anisotropic Hubbard model, we first describe in Fig.5.18 the results obtained in the absence of intersite spin coupling with various values of the Hund's coupling J/W and the Coulomb interaction U/W. The other parameters is determined in such a way that the system remains rotationally invariant. The magnetic susceptibility $\chi''(\omega)$ for $U/W = 1$ but in the absence of Hund's coupling shows a broad responses. As expected, the peak is located at $\omega/W \approx 1$. In the finite Hund's coupling value, one can see the formation of peak-like feature at low energies and a simultaneous suppression at the higher energy part. When the Coulomb interaction and the Hund's coupling increase the peak at the low energy part is further enhanced and there is a suppression at higher energy. The most pronounced enhancement at low energy is observed

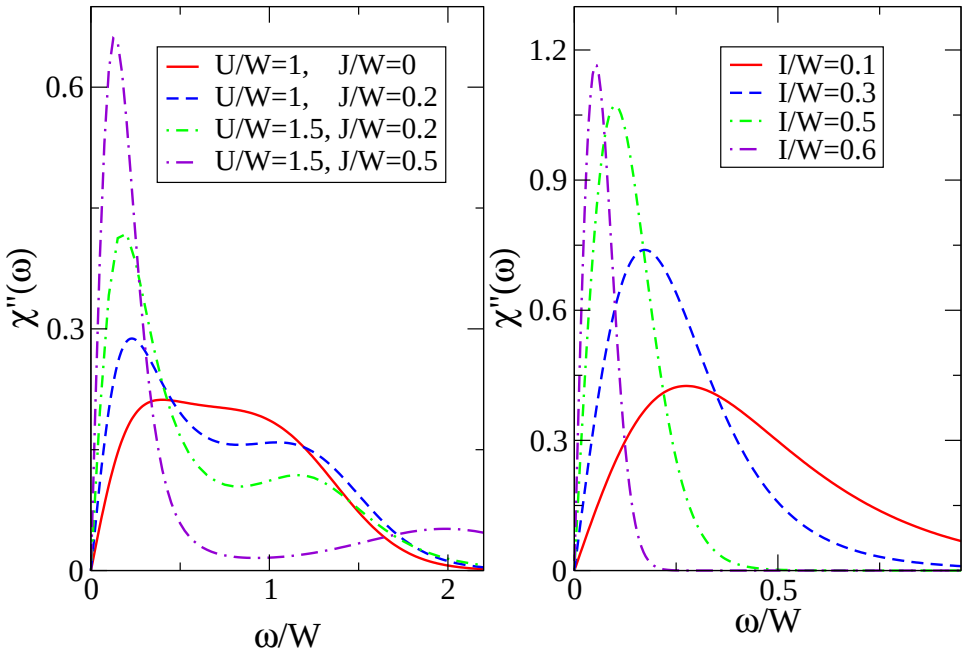

Figure 5.18: The left panel shows the dynamical spin susceptibility $\chi''(\omega)$ of the anisotropic two-band Hubbard model at half-filling for different interaction strengths U/W, Hund's coupling J/W and at temperature $T/W = 0.1$. The right panel displays the results for Hund's coupling $J/W = 0$ and for various values of intersite interaction I/W.

for $U/W = 1.5$ and $J/W = 0.5$. We argue in this case that the overall behavior of spectra can be described within RPA theory. The enhancement of the low energy peak thus corresponds to the fact that the Stoner instability criteria is approached. This result suggests that the presence of Hund's coupling increases the spin fluctuations in the system.

The right panel of Fig.5.18 illustrate the results of the magnetic susceptibility in the absence of Hund's coupling but for different value of the intersite spin interaction I/W. As expected, the spin susceptibility shows a broad response in the weak coupling regime. The gradual enhancement of the low energy peak is observed when the intersite interaction is considered. The characteristics of the spin susceptibility in the present case is clearly comparable to the previous one which is composed of single peak like. This results also indicate that the inclusion of the intersite spin interactions leads to a more pronounced spin fluctuations which strongly effects the low energy regime.

Having considered the influence of the Hund's coupling and the non-local spin interactions separately, let us now discuss the magnetic susceptibility in the case where all parameters in the Hamiltonian of (5.4) are considered. In this respect, the model parameters are $U/W = 1.5$, Hund's coupling J/W=0.5. The results of the calculations are depicted in the left panel of Fig.5.19. The general feature of spin spectra in the present results is again comparable with the two previous case described above. The low energy part is gradually enhanced as spin coupling I/W increases signaling a pronounced fluctuation and consequently the enhanced effective mass.

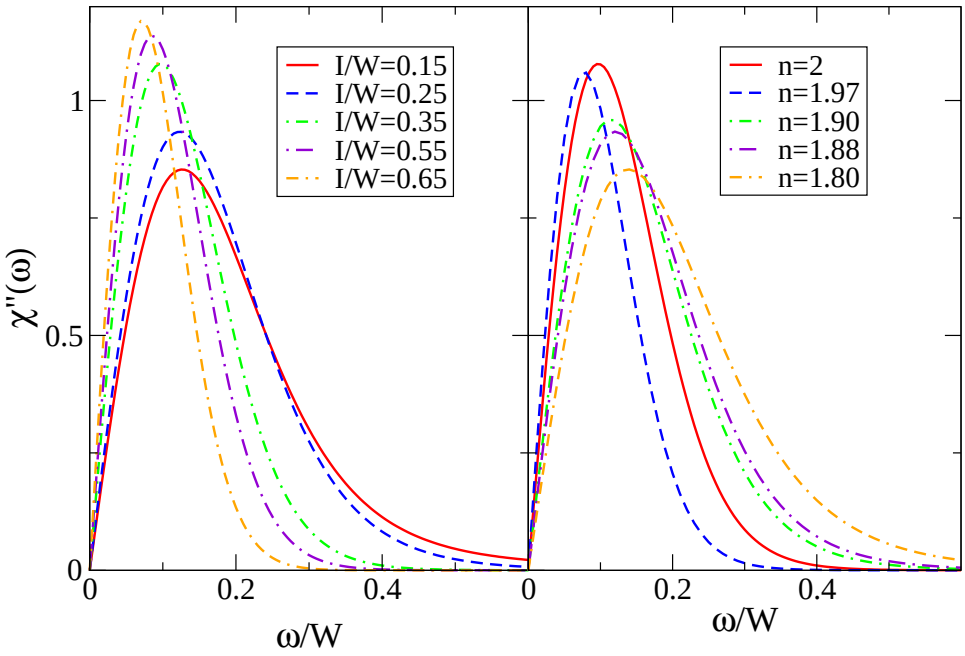

Figure 5.19: The same as Fig.5.18 with the same notation. The present case is, however, obtained for U/W=1.5, J/W=0.5, and for various values of intersite interaction I/W (left panel). The right panel depicts the results for various electron occupancies at $I/W = 0.35$.

When the system is doped, the intensity of low energy spectral weight gradually decreases. This is shown in the right panel of Fig.5.19. In this case, the parameters are set to $U/W = 1.5$, $J/W = 0.5$ and $I/W = 0.5$. From this behavior one thus learns that the doping suppresses the fluctuation in the system and will be also reflected in the changes of the effective mass or the imaginary part of the self energy. We note here, in contrast with the single band-two dimensional case described in the previous chapter, there is no additional feature e.g low-energy dip in the spin susceptibility. The whole feature is thus expected to be captured by the RPA approximation.

5.3.3 Single-Particle Spectral Function

The effect of low-energy enhancement in the spin susceptibility at the single-particle level will be investigated in this section based on the results of the single-particle spectral function. At first, let us consider the role of Hund's coupling as illustrated in the left panels of Fig.5.20 with upper and lower panels referring to a narrow and a broad band respectively. The solid line in the figure is the non-interacting density of states derived from the tight binding bands. The narrow band is characterized by two van Hove singularity at the upper and the lower Fermi level while in between it shows a parabolic like behavior that mimics the one dimensional DOS. The wide band consists of a single van-Hove singularity that lies close to the Fermi energy. Clearly these bands are asymmetric with respect to the Fermi level and according to the LDA results, the occupancy ratio of the narrow xz,yz and the wide yz bands are 8/3 and 4/3 respectively [116]. By considering only the Coulomb interaction, the spectral weight of both bands decreases and

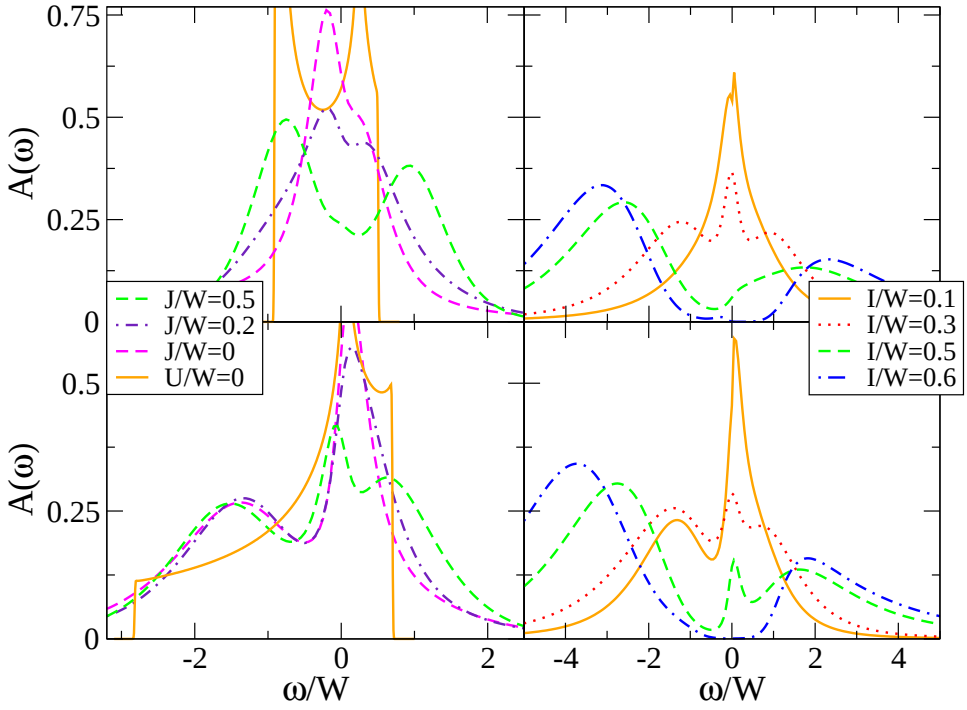

Figure 5.20: The left panel shows the single-particle spectral function of the half-filled anisotropic Hubbard model for $U/W = 1.5$, and for various values of Hund's coupling J/W. Note that the solid curve is non-interacting density of states $U/W = 0$ derived from tight binding bands. Right panels: same as in the left panel but in the absence of Hund's coupling and various value of spin interaction I/W. The upper panels illustrate the spectra of the narrow band while the lower panels show the results of wide band.

also broadens. The narrow band is composed of a single peak-like structure while the broad band shows a dip at lower energies. When Hund's coupling is considered the peak in the spectra of both bands is suppressed. For $J/W = 0.5$, the narrow band shows one-dimensional like DOS that is renormalized by the interaction. The other band on the other hand consists of three peak structure with shoulders at lower and higher energies. The reduction of the spectral weight in the single-particle spectra is clearly related to the increase of the low-energy spin susceptibility, described in Fig.5.18.

A close inspection to the imaginary part of the self energy (not shown) reveals that the low energy part of both bands for weak coupling $J/W \leq 0.2$ can be extrapolated to zero meaning that there exists a well-defined Fermi liquid state. When the Hund's coupling is further increased up to $J/W = 0.5$ the imaginary part of self energy becomes finite, thus indicating a finite life time. This behavior is in contrary to previous DMFT results that use Bethe DOS, where the violation of the Fermi liquid behavior only occurs in the broad band. It also conflicts with the suggestion of LDA results that claim the Fermi liquid characteristic to hold even in the presence of interactions. The presence of non Fermi liquid character in this two band system is clearly corresponds to the Hund's coupling which tends to increase the spin fluctuation which eventually favors the gapped phase. Due to the presence of pronounced singularity in the DOS, it is difficult

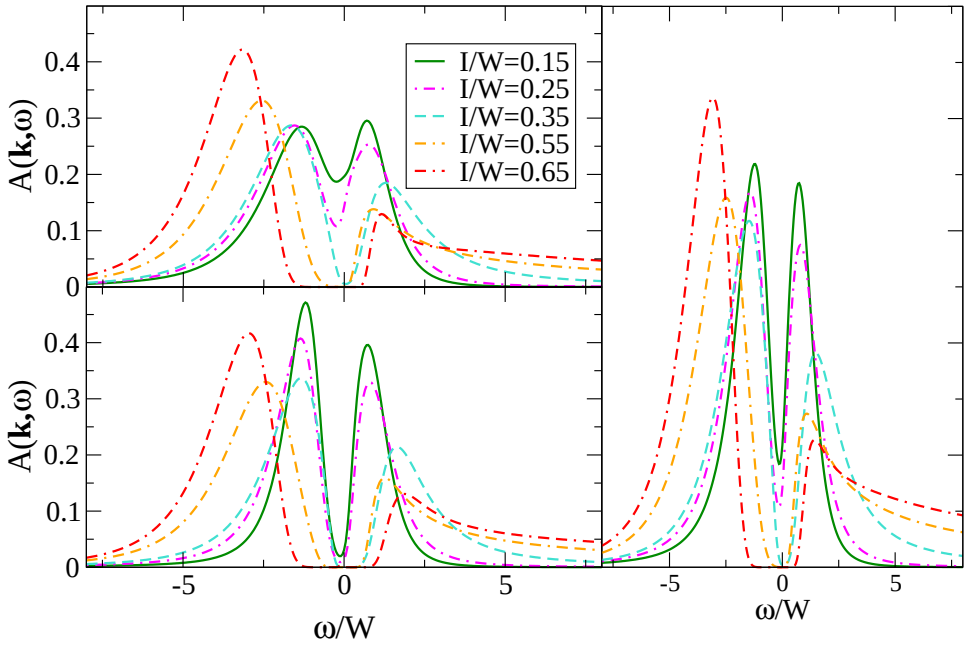

Figure 5.21: Orbitally-resolved spectral function of the half-filled anisotropic Hubbard model at momentum vector **k**=($\frac{\pi}{2}$, $\frac{\pi}{2}$), for U/W=1.5, J/W=0.5, $T/W = 0.1$ and for various values of non-local interaction I/W, The upper-left panel shows the single-particle spectral function for wide band whereas the lower-left panel for the narrow band. The right panel displays the results of the total spectral function.

to go beyond the interaction values specified above since the increase of the interaction only amounts to a broadening of the spectra.

Let us now consider the case without incorporating the Hund's coupling but for various values of the non-local interactions as depicted in the right panel of Figure 5.20. In this case, one observes three peaks for both bands at $I/W = 0.3$, much the same as in the single band Hubbard model (see figure 4.1). As the coupling increases the quasiparticle of narrow band collapses and the spectrum shows a gap. In contrast, the other band shows a resonance albeit its weight is also reduced. In the highest calculated coupling $I/W > 0.5$, both bands enter the gapped phase with the largest gap width is obtained for the narrow band. This suggest that the narrow band is more correlated than the wide band and more importantly, the variation of intersite interaction also drives the two step transition. The suppression of the spectral weight as well as the gap opening should be again understood as the result of the pronounced spin fluctuation in the system which is also manifested in the low-energy part of the spin susceptibility (see Fig.5.18). Another important point that can be drawn from this results is that the narrow band with lower dimensionality is strongly influenced by the non-local fluctuation.

In the next figure (see Fig.5.21) we illustrate the results of the spectral function for different values of the intersite interaction. The interaction parameters are set to U/W=1.5, J/W=0.5. As is clearly seen, even for small values of the intersite interaction I/W, the spectra exhibit a gap like structure which is more pronounced for the narrow band. As the interaction increases, both

bands undergo consecutive transitions to the gapped-phase. In the strong coupling $I/W \geq 0.55$ the gap widths of both bands become approximately the same which can be understood by arguing that the difference of the bandwidth is smeared by strong electronic correlations. The results of Fig.5.20 and Fig.5.21 thus generally suggest that localized and itinerant character also appear even in the presence of the spatial fluctuations. The inclusion of intersite spin interactions clearly enhances the effective Coulomb interactions and the system favors the insulating state. From the total spectral function (right panel of Fig.5.21) one observes the similar trends as observed before in the DMFT. The contribution of the narrow band is significant in the weak coupling case while the other band for stronger coupling.

Very recently, two different groups have also addressed the same issue discussed here. The authors of Ref.[131] describe OSMT as a single correlated band that is coupled with fully localized orbital. Their Hamiltonian is closely related to the Kondo lattice model except that the onsite Coulomb interaction is also considered. In order to observe the metal insulator transition in the weakly correlated band, they employed determinant quantum monte carlo (DQMC) [132] which is modified to include the effects of the fluctuating local spin degrees of freedom of the localized bands. Their calculation is performed on a lattice of size 8x8 sites with the density is fixed equal to one. They showed that OSMT is possible in their simplified model since the single-particle spectral function of the itinerant band evolves from the metallic in the small coupling value to the insulating phase for larger values. They pointed out that by considering non-local fluctuations, there is a significant formation of the intersite magnetic correlations. This however does not influence the nature of the Mott transition in the itinerant band and thus they argue that the physics of OSMT remains the same even if the spatial fluctuations is also taken into consideration.

Within the same model as described before for DMFT, the authors of Ref.[133] also investigated the influence of spatial fluctuation in OSMT. They employed the state-of-the art dynamical cluster approximation with small cluster sizes $N_c = 2$ and $Nc = 4$ combined with the continuous time quantum monte carlo method as an impurity solver. The calculations are performed in the half-filling with various values of the Coulomb interactions and temperatures. In the $N_c = 2$ their results indicate that both bands undergo a simultaneous transition since there is a pronounced antiferromagnetic fluctuations within this cluster size. For $N_c = 4$ that also incorporates next nearest-neighbor, they finally observe the OSMT in the strong onsite interaction values. They further indicated that the weakly correlated case has a well-defined Fermi state which is in contrast with intermediate coupling where the Fermi liquid theory breaks down. In general, the results of DCA and DQMC suggest the existence of the OSMT when spatial fluctuations are considered and in a good agreement with the results presented in this section. The presence of the pseudogap in the small weak coupling value I/W thus in the context of DCA can be associated with the smaller cluster size. It is however difficult to associate the number of clusters and the values of coupling I/W employed in the present case. Based on the single band cases, the large number of cluster is required to open full gap for fixed interaction parameters.

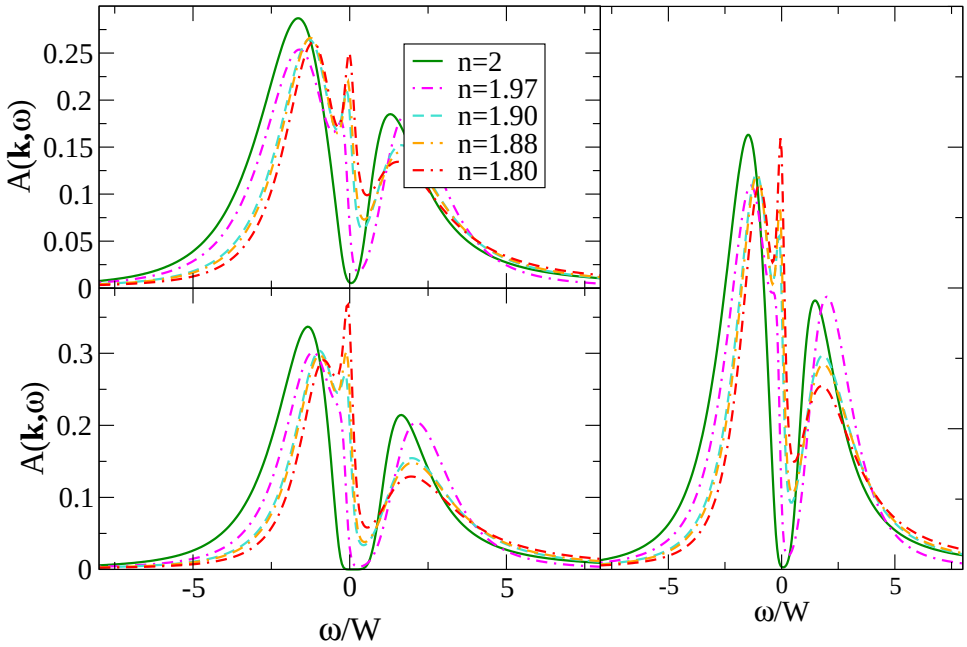

Figure 5.22: The same as in Fig.5.21, however the spectra in the present case are obtained by varying the electron occupancy at coupling strength of $I/W = 0.35$.

The two band system with the cluster size is more than 8 clearly demands a large computational efforts. In this regard EDMFT method offers a technical advantage in that the spatial fluctuations are incorporated within a single site scheme and thus the effects of a large cluster size can be investigated by choosing a large intersite coupling.

Having discussed the behavior of the system at half-filling, in what follows we describe the system in the hole doped case as presented in Fig.5.22. These results were obtained for $I/W = 0.35$, $U/W = 1.5$. The increase of the hole doping concentration leads to a decrease of the gap in the spectra. The gap of both bands reduces to the pseudogap for $n = 1.90$ with the wide band being more sensitive to the presence of doping. A further increase of the doping leads to the formation of metallic peak at low energies together with an additional pseudogap for higher energies. To make sure that such a behavior is not from analytical continuation, we have compared the self energy (not shown) of both bands. It turned out that the self energy of the narrow band is always smaller than for the other one, meaning that the correlation in the narrow band is more pronounced. The imaginary part of the self energy also indicates a deviation from the standard Fermi liquid and hence the resonance is not due to a quasiparticle peak but rather to the short-lived excitations. The changes of gap into pseudogap as well as the presence of peak can be again understood as a direct consequence of the reduction of the low energy peak in the spin susceptibility (cf. Fig.5.19).

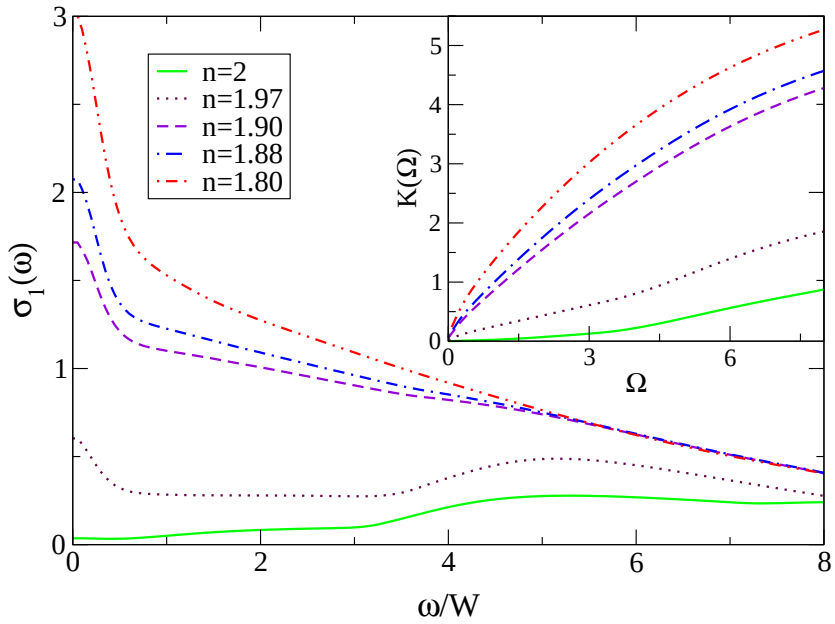

Figure 5.23: The frequency-dependent optical conductivity of the anisotropic Hubbard model for U/W=1.5, J/W=0.5, $I/W = 0.35$, $T/W = 0.1$ and for different band fillings n. The inset shows the optical integral.

5.3.4 Optical Conductivity and Particle-Particle Spectral Function

The frequency-dependent optical conductivity in the EDMFT can be evaluated essentially in a similar manner as in the DMFT. This again follows the observation that the momentum independent self energy is retained as a consequence of the vanishing of higher-order vertex contributions. The effect of nonlocality thus enters from the single-particle spectra since (see Eq.3.16) the self energy has incorporated the feedback of the spin fluctuations. In the present case, the lattice structure is obtained from the tight binding DOS as expressed in Eq.5.1. We now describe the evolution of the conductivity in the hole doped case illustrated in Fig.5.23. Close to half-filling, suppression of the spectral weight at low as well as at high energies is evident. When the system is doped, the peak at $\omega/W = 0$ shifts to higher energies and the spectra show Drude like peak in the high-doped regime signaling the metallic character. The presence of hole doping clearly increases the mobility of electron carriers. This is clearly manifested in the integrated spectra as depicted in the inset of Fig.5.23. While the spectral weight is suppressed near half-filling, $K(\Omega)$ of the metallic phase rapidly increases as a function of Ω indicating an increase of the kinetic energy of the carriers. It is remarkable however that the decay of the conductivity does not show standard power law namely $\sigma(\omega) = \omega^{-2}$ [60]. Deviation from this condition is a clear indication that the systems is from non Fermi liquid type.

We further investigate the scattering rates $\tau^{-1}(\omega)$ and the mass enhancement m^*/m_0, as demonstrated in Fig.5.24. The scattering close to the Mott insulating phase is well pronounced. For $n = 1.97$, one observes a broad hump at low energies which is followed by a suppression

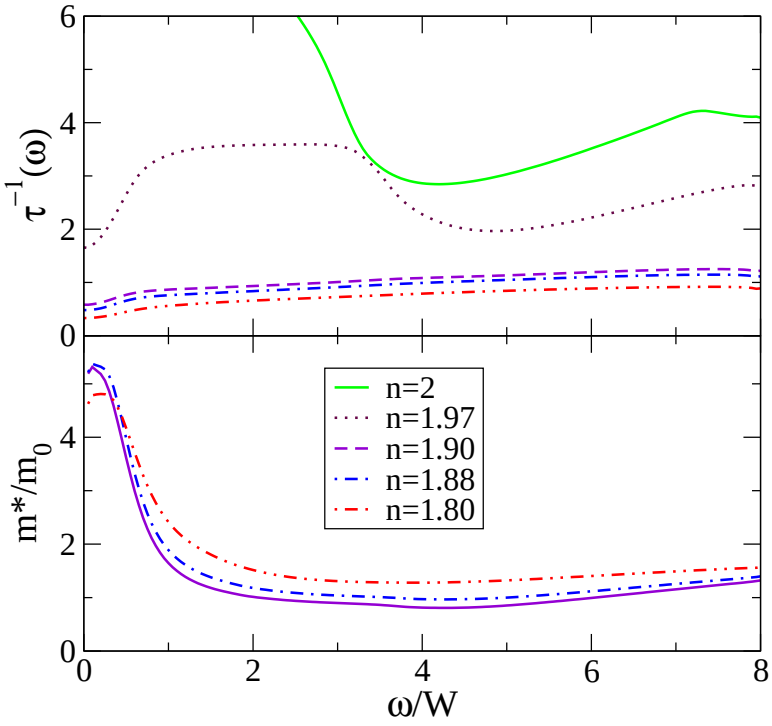

Figure 5.24: The frequency dependence of the scattering rate (upper plane) and the mass enhancement (lower panel) of the anisotropic two-band Hubbard model. The spectra are calculated by using the same parameters as in Fig.5.23.

at high energies. This corresponds to the suppression of conductivity at $1 \leq \omega \leq 4$ as well as the interband peak at higher energies. In contrast, the scattering rate in the highly doped case is characterized by a linear dependence of ω reminiscent to what occurs in heavy fermion compounds [134] which signals the violation of the standard Fermi liquid behavior. When the system is further doped, the spectral weight shifts to lower energies while still maintaining the overall behavior. The lower panel of Fig.5.24 illustrates the effective mass as a function of doping. While the spectra show monotonous behavior at high frequencies there is a clear peak shift as a function of the doping at the low energy scale. The decrease of effective mass as the doping increases is a restatement of the enhancement of the low spectral weight of conductivity and also the kinetic energy.

The influence of the spatial fluctuations onto the two-particle excitation is illustrated in the left panel of Fig.5.25. A broad response is observed for all values of the spin-exchange coupling I/W. As anticipated, the intensity of the spectra diminishes as a function of the spin coupling and the position of the peak remains unchanged. At the largest spin interaction values, the total spectral weight is significantly suppressed. In addition, there is a gap formation at low energies (near to zero) for $I/W \geq 0.55$ which is comparable with that of the single-particle spectral function. Following the argument pointed out before, the suppression of the spectral weight together with low energy gap is again a clear indication of the non metallic character.

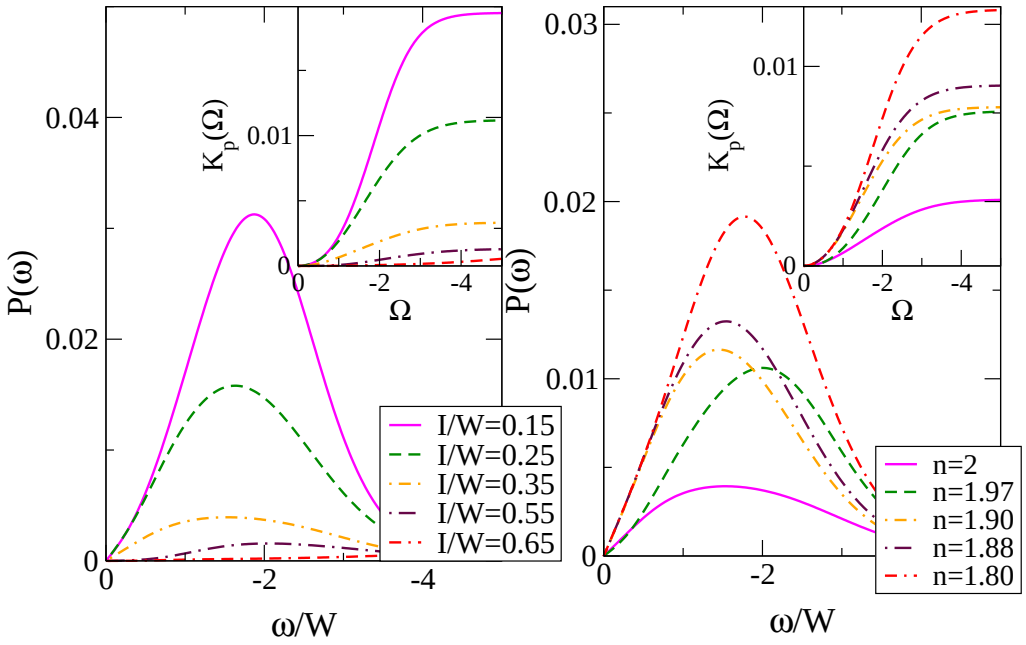

Figure 5.25: The EDMFT-QMC results for the two-particle spectral function of the anisotropic two-band Hubbard model at half-filling for $U/W = 1.5$, $J/W = 0.5$ and for $T/W = 0.1$. The left and the right panels correspond to the two-particle spectra for various values of I/W and for different band occupation respectively. The insets show the results of integrated spectra as function of Ω.

The reduction of spectral weight is also indicated by the integrated spectra illustrated in the inset of Fig.5.25. These results therefore suggest that the interplay of the Coulomb interaction, the Hund's coupling and the intersite spin interaction favors the insulating state which in line with the discussion based on the single-particle excitations and the optical conductivity. As the system is doped away from half-filling (see the right panel of Fig.5.25), the spectral weight quickly increases and becomes maximal for a value of $n = 1.80$. The same behavior can be also observed in the integrated spectra as depicted in the inset of the right panel. In the the low energy part, one observes that the spectra are characterized by linear dependency for all band fillings. We point out here, that the pseudogap or small dip at single-particle spectra is clearly missing in the local particle-particle spectral function.

CHAPTER 6

Summary and Outlook

The correlation-induced metal-insulator transition (MIT) constitutes one of the most challenging problems in the solid state physics. After more than six decades of endeavors, the interest in the subject is unabated. The introduction of the dynamical mean field theory (DMFT) has led to a significant progress in the understanding some important aspects of the problem. The novelty of this approach lies on its ability to simplify the complexity of certain problems into a more manageable one and yet to capture the essence of the original problems. In addition, it allows to obtain the dynamic of the physical quantity that can be directly related to the experimental results. Study of the metal-insulator transition within DMFT is usually done by exploring the single particle properties that are experimentally investigated via single-particle photoemission. Details of transport properties are then investigated from the two particle quantity such as the optical conductivity. While this procedure is relatively established for the particle-hole sector, the particle-particle properties are on the other hand relatively less explored. This is mainly due to the lack of experimental techniques that are capable of measuring the particle-particle excitations. With the recent rapid progress in designing the experimental setup, it is now possible to excite simultaneously two electrons (hole) and to measure their energies and momenta. Applications of this method known as $(\gamma, 2e)$, in the context of metal-insulator transition is expected to yield more insights into the mechanism of Mott transition.

In order to investigate the particle-particle excitations, there are three main routes that have been implemented in this work. The first and the second route, the first order approximation and the ladder approximation, calculate the two particles from the knowledge of the single-particle spectral function which in this case is delivered by DMFT. In the implementation, they are closely related to the procedure for calculating the optical conductivity. In the third approach, the two-particle quantities are directly evaluated within the loop of DMFT and quantum monte carlo (QMC). Due to the structure of the DMFT approximation, that only allows for calculating the local quantities, all procedures thus provide the local pair correlations. These schemes are applied

to the single- and isotropic two-band Hubbard model at half-filling and in the hole-doped case. The behavior of the two particles is then analyzed at the verge of metal-insulator transition. Since the integrated spectra of the two particle quantity corresponds the double occupancy in the system, the accuracy of the approach is determined based on the fulfillment of this relation. From the results of DMFT-QMC, one obtains a good agreement between the integrated spectra and the two-particle sum rule. The transition from metal to insulating phase is marked by the reduction of the spectral weight as well as the shift of the spectral peak to higher energy. Based on this observation, it is argued that the two-particle spectral function provides a clear signature of the correlated metal-insulator transition. In contrast to the above self-consistent two-particle spectra, the results from the first order and the ladder approximation tend to deviate from the sum rule constraint. This suggests the importance of self consistency in the calculation of the two-particle quantity. The relation between the calculated spectra and the measured quantity in two-particle spectroscopy has been made straightforwardly. Under certain conditions, the intensity of $(\gamma, 2e)$ is proportional to the two-particle spectral function.

DMFT becomes unreliable in various cases where the effects of the non-local correlation becomes non negligible. In addition, the accuracy of the mean-field like approximation is also known to deteriorate for low-dimensional system. Various methods have been introduced to improve this approximation, and some of them have been briefly discussed in this thesis. In the present work, the extended dynamical mean field theory (EDMFT) is employed to study the role of the non-local contributions in the metal-insulator transition. Within this method, the spatial fluctuation enters via non-local term in the Hubbard model e.g spin-spin or charge interaction. Following DMFT, the central approximation is the locality of the self energy which in this respect, applies not only to the single-particle self energy but also to the two-particle. This method is then employed to calculate the single- and the two-particle correlation function of the two-dimensional Hubbard model The single-particle spectrum shows a gap formation as the intersite spin coupling increases. This indicates that the paramagnetic metal-insulator transition in the 2D Hubbard model is the consequence of the interplay between the local Coulomb and the spin fluctuations. It also suggests that the gap can be realized at any finite Coulomb interactions, which is in accord with Anderson's proposal. The study of the system in the hole-doped case reveals the existence of the pseudogap for all band fillings. Inspection of the behavior of the self energy as well as the transport properties in this regime indicates the violation of canonical Fermi liquid behavior. The different nature of metallic and insulating phase at and away from half-filling is also investigated from the two-particle spectral function. In general, the results resemble those obtained in the high-dimensional Hubbard model with the metallic phase is characterized by the peak intensity and the insulating phase is marked by the gap at low energies. The pseudogap observed in the single-particle spectra is, however, not reflected in the two-particle spectra.

A new class of metal-insulator transition has recently observed in the ruthenates compounds that are isostructural with the high-T_c cuprates. In this system, various components such as the orbital degrees of freedom, the local interaction, the anisotropic bandwidth and the ex-

change interaction are strongly involved in determining the nature of the Mott metal-insulator transition. In this work, this phenomena is studied within the two band Hubbard model that incorporate the Hund's exchange coupling. Results of the single-particle spectral function in the paramagnetic phase show a good agreement with previously published works. The interplay of the anisotropic bandwidth and the local correlation leads to the orbital-selective Mott transition (OSMT). The calculated optical conductivity and the EELS spectra indicates the clear signal of Fermi liquid behavior. Within DMFT+QMC, the two-particle spectral function of total band is also presented. The general feature mimics that the single-band Hubbard model. The increase of coupling leads to the suppression of spectral weight which corresponds to the reduction of double occupancy.

In contrast to paramagnetic case, the metal-insulator transition in the antiferromagnetic phase of the anisotropic two band Hubbard model occurs simultaneously for both bands. They are distinguished however by the magnetization values and intensities of the spectra which are found to be stronger in the narrow band. As the system is doped, all bands evolve simultaneously to metallic phase signaling the absence of OSMT. The behavior of the optical conductivity in this phase resembles that single particle case namely it consists of single peak structure and with low-energy gap signaling the insulating character. The influence of the spatial fluctuations in the orbitally selective Mott transition has been also addressed in this work by incorporating the intersite spin-spin interaction in the two band Hubbard model. The lattice structure is obtained from the two dimensional tight binding DOS that is derived from the LDA results. The interplay of strong interaction and the spatial fluctuation clearly indicates the possible existence of the itinerant and localized character. The same is also observed for the particle-hole and the particle-particle sectors.

A natural extension of the present work would be to calculate the momentum-dependent single- and two-particle spectral functions. This would be extremely useful to investigate various phenomena such as the momentum dependence MIT, kink in the dispersion energy and the non-local pairing which can not be investigated within DMFT as well as EDMFT. Another possible extension is also to investigate the nature of the two-particle excitations in the magnetically ordered phase.

Bibliography

[1] J. Hubbard. *Proc. Roy. Soc. A*, 276:238, 1963.

[2] E.H. Lieb and F.Y.Wu. *Phys. Rev. Lett*, 20:1445, 1968.

[3] M.C. Gutzwiller. *Phys. Rev. Lett*, 10:159, 1963.

[4] J.Kanamori. *Prog. Theor. Phys*, 30:275, 1963.

[5] J.H. de Boer and E.J.W Verway. *Proc. Phys. Soc. London A*, 49:59, 1937.

[6] R. Peierls. *Proc. Phys. Soc. London A*, 49:72, 1937.

[7] N.F. Mott. *Proc. Phys. Soc. London A*, 62:416, 1949.

[8] N.F. Mott. *Metal-Insulator Transitions*. Taylor and Francis, London, 1990.

[9] M. Imada, A. Fujimori, and Y Tokura. *Rev.Mod.Phys*, 70:1039, 1998.

[10] P. Limelette, P. Wzietek, S. Florens, A. Georges, T.A. Costi, C. Pasquier, D. Jerome, C. Méziére, and P. Batail. *Phys.Rev.Lett*, 91:016401, 2003.

[11] D.B. McWhan, J.P. Remeika, T.M. Rice, W.F Brinkman, J.P Maita, and A.Menth. *Phys. Rev. Lett*, 27:941, 1971.

[12] D.B. McWhan, A.Menth, J.P. Remeika, W.F Brinkman, and T.M. Rice. *Phys. Rev. B*, 7:1920, 1973.

[13] C. Castellani, C. Natoli, and J. Ranninger. *Phys. Rev. B*, 18:4967, 1978.

[14] W.F. Brinkman and T.M Rice. *Phys. Rev. B*, 2:4302, 1970.

[15] M.C. Gutzwiller. *Phys. Rev*, 134:A923, 1964.

[16] M.C. Gutzwiller. *Phys. Rev*, 137:A1726, 1965.

[17] W. Metzner and D. Vollhardt. *Phys. Rev. Lett*, 62:324, 1989.

[18] J.P. Lu. *Phys. Rev*, 49:5687, 1994.

[19] J.W. Negele and H. Orland. *Quantum many-Particle system*. Westview Press, New-York, 1998.

[20] S. Hüfner. *Photoelectron Spectroscopy*. Springer Verlag, Berlin, 1995.

[21] F. Reinert and S. Hüfner. *New Journal of Physics*, 7:97, 2005.

[22] A. Damascelli, Z Hussain, and Zhi-Xun Shen. *Rev. Mod. Phys*, 75:473, 2003.

[23] H.R. Hertz. *Annalen der Physik und Chemie*, 31:983, 1887.

[24] W.Hallwachs. *Annalen der Physik und Chemie*, 33:301, 1888.

[25] A. Einstein. *Ann. Phys*, 17:132, 1905.

[26] C.N. Berglund and W.E. Spicer. *Phys. Rev*, 136:A1030, 1964.

[27] A. Georges and G. Kotliar. *Phys. Rev. B*, 45:6479, 1992.

[28] A. Georges, G. Kotliar, M. Rozenberg, and W. Krauth. *Rev. Mod. Phys*, 68:13, 1996. and references therein.

[29] P.W. Anderson. *Phys. Rev*, 124:41, 1961.

[30] N. Blümer. *Mott-Hubbard Metal-Insulator Transition and Optical Conductivity in High Dimensions*. Shaker-Verlag, Aachen, 2002.

[31] G. Kotliar, S.Y. Savrasov, G. Pállson, and G. Biroli. *Phys. Rev. Lett*, 87:186401, 2001.

[32] M.H. Hettler, A.N.Tahvildar-Zadeh, M. Jarrell, T. Pruschke, and H.R. Krishnamurthy. *Phys. Rev. Lett*, 58:R7475, 1998.

[33] E.Z. Kuchinskii, I.A. Nekrasov, and M.V. Sadovskii. *Low. Temp. Phys*, 32:398, 2006.

[34] M.V. Sadovskii, I.A. Nekrasov, E.Z. Kuchinskii, Th. Pruschke, and V.I. Anisimov. *Phys. Rev. B*, 72:155105–1, 2005.

[35] A. Toschi, A.A. Katanin, and K.Held. *Phys. Rev. B*, 75:045118–1, 2007.

[36] Q. Si, S. Rabello, K. Ingersent, and J.L. Smith. *Nature*, 413:804, 2001.

[37] Ping Sun and G. Kotliar. *Phys. Rev. B*, 66:085120–1, 2002.

[38] K. Haule, A. Rosch, J. Kroha, and P. Wölfle. *Phys. Rev. B*, 68:155119–1, 2003.

[39] S. Burdin, D.R. Grempel, and M. Grilli. *Phys. Rev. B*, 75:224423, 2007.

[40] J. Llweilun Smith and Qimiao Si. *Phys. Rev. B*, 61:5184, 2000.

[41] K. Yosida and K. Yamada. *Prog. Theor. Phys*, 46:244, 1970.

[42] K. Yosida and K. Yamada. *Prog. Theor. Phys*, 53:1286, 1975.

[43] V.B. Zlatić, B. Horvatić, and D. Sokcević. *Z. Phys. B*, 59:151, 1985.

[44] N. Bickers. *Rev. Mod. Phys*, 59:845, 1987.

[45] V. Drchal, V. Janis, J. Kudrnovsky, V.S. Oudovenko, X. Dai, K. Haule, and G. Kotliar. *J. Phys. Cond. Mat*, 17:61, 2005.

[46] C. Gros, W. Wenzel, R. Valenti, G. Hülsenbeck, and J. Stolze. *Europhys. Lett*, 27:299, 1994.

[47] J.E. Hirsch and R.M. Fye. *Phys. Rev. Lett*, 56:2521, 1986.

[48] Suzuki. *Many-Particle system*. Westview Press, New-York, 1988.

[49] F.F. Assaad eds H.Fehske, Alexander Weiβe, and Ralf Schneider. *Computational Many-Particle system*. Springer-Verlag, Berlin, 2008.

[50] S.R. White. *Phys. Rev. Lett*, 69:2863, 1992.

[51] K.G. Wilson. *Rev. Mod. Phys*, 47:773, 1975.

[52] H. Kajueter and G. Kotliar. *Phys. Rev. Lett*, 77:131, 1996.

[53] P.Werner, A. Comanac, Luca de' Medici, M. Troyer, and A.J. Millis. *Phys. Rev. Lett*, 97:076405, 2006.

[54] A.N. Rubtsov, V.V. Savkin, and A.I. Lichtenstein. *Phys. Rev.*, 77:131, 1996.

[55] K. Takegahara. *J. Phys. Soc. Japan*, 62:1736, 1993.

[56] D.J. Scalapino and R.L. Sugar. *Phys. Rev. B*, 24:4295, 1981.

[57] Yukitoshi Motome and G. Kotliar. *Phys. Rev. B*, 62:12800, 2000.

[58] M. Jarrell and J.E. Gubernatis. *Phys. Rep*, 269:133, 1996.

[59] R.K. Bryan. *Eur. Biophys*, 18:165, 1990.

[60] M. Dressel and G. Grüner. *Electrodynamics of Solids*. Cambridge University Press, Cambridge, 2003.

[61] G. Mahan. *Many-Particle system*. Plenum Press, New-York, 1990.

[62] D.G. Scalapino, S.R. White, and S. Zhang. *Phys. Rev. B*, 47:7995, 1993.

[63] A. Khurana. *Phys. Rev. Lett*, 64:1990, 1990.

[64] M. Jarrell, J.K. Freericks, and Th. Pruschke. *Phys. Rev. B*, 51:11704, 1995.

[65] Th. Pruschke and R. Zitzler. *J. Phys. Cond. Mat*, 15:7867, 2003.

[66] W. Nolting. *Z. Phys. B*, 80:73, 1990.

[67] W. Nolting, G. Geipel, and K.Ertl. *Z. Phys. B*, 92:75, 1993.

[68] W. Nolting, G. Geipel, and K.Ertl. *Phys. Rev. B*, 45:5790, 1992.

[69] N.A. Alford, A. Barrie, I.W. Drummond, and Q.C. Herd. *Surf. Interface Anal.*, 1:36, 1979.

[70] J.J. Lander. *Phys. Rev*, 91:1382, 1953.

[71] C.J. Powell. *Phys. Rev. Lett*, 30:1179, 1973.

[72] M. Cini. *Solid. State. Commun*, 24:681, 1977. and references therein.

[73] G.A. Sawatzky. *Phys. Rev. Lett*, 39:504, 1977.

[74] G. Treglia, M.C. Desjonqueres, F. Ducastelle, and F. Spanjaard. *J. Phys. C*, 14:4347, 1981.

[75] V. Drchal. *J. Phys. Cond. Mat*, 1:4773, 1989.

[76] V. Drchal and J. Kudrnovsky. *J. Phys. F*, 14:2443, 1984.

[77] W. Nolting, G. Geipel, and K.Ertl. *Phys. Rev. B*, 44:12197, 1991.

[78] I.E McCarthy and E. Weigold. *Rep. Prog. Phys*, 54:789, 1991.

[79] J. Weigold. *J. Phys. Colloq*, 3:C6–187, 1993.

[80] J.R. Dennison and A.L. Ritter. *J. Elec. Spec. Relat. Phenom*, 77:99, 1996.

[81] E. Weigold and M. Vos. *Many Particle Spectroscopy of Atoms, Molecules, Cluster and Surfaces*. edited by J. Berakdar and J. Kirschner. Kluwer Academic/Plenum Publishers, New York, 2001.

[82] O.M. Artamonov, S.M. Samarin, and J. Kirshner. *J. Appl. Phys. A*, 65:535, 1997.

[83] M. Vos, A.S. Kheifets, C. Bowles, C. Chen, E. Weigold, and F. Aryasetiawan. *Phy. Rev. B*, 70:205111, 2004.

[84] K.A. Kouzakov and J. Berakdar. *J. Phys. Cond. Mat*, 15:L41, 2003.

[85] S.A. Canney, M.J Brunger, I.E McCarthy, P.J. Storer, S. Utteridge, M.Vos, and E. Weigold. *J. Elec. Spec. Phen*, 83:65, 1997.

[86] C. Chen, M.N. Gale, A.S. Kheifets, M. Vos, and M.R Went. *J. Phys. Cond. Mat*, 17:7689, 2005.

[87] F.O. Schuman, J. Kirschner, and J. Berakdar. *Phys. Rev. Lett*, 95:117601, 2005.

[88] R.Herrmann, S. Samarin, H. Schwabe, and J. Kirschner. *Phys. Rev. Lett*, 81:2148, 1998.

[89] C. Caroli, D. Lederer-Rozenblatt, B. Roulett, and D.S. James. *Phys. Rev. B*, 8:4552, 1973.

[90] N. Fominykh, J. Henk, J. Berakdar, P. Bruno, H. Gollisch, and R. Feder. *Sol. Stat. Comm*, 113:666, 2000.

[91] N. Fominykh, J. Henk, J. Berakdar, and P. Bruno. *Phys. Rev. Lett*, 89:086402, 2002.

[92] J. Berakdar. *Phys. Rev. B*, 58:9808, 1998.

[93] N. Fominykh and J. Berakdar. *J. Elec. Spec. Rel. Phen*, 100:20, 2007.

[94] F.O. Schumann, N. Fominykh, C. Winkler, J. Kirschner, and J. Berakdar. *Phys. Rev. B*, 77:235434–1, 2008.

[95] N. Fominykh, J. Henk, J. Berakdar, and P. Bruno. *Surf. Sci*, 507-510:229, 2002.

[96] A. Fetter and J.D. Walecka. *Quantum Theory of Many Particle System*. McGraw-Hill,Inc, New-York, 1971.

[97] J. Berakdar. *Phys.Rev.Lett*, 83:5150, 1999.

[98] J.Berakdar. *Concepts of Highly Excited Electronic System*. Wiley-VCH, Berlin, 2003.

[99] G. Seibold and J. Lorenzana. *Phys. Rev. lett*, 100:016405, 2008.

[100] J.G. Bednorz and K.A. Müller. *Z. Phys. B*, 64:189, 1986.

[101] P.W. Anderson. *Science*, 235:1196, 1987.

[102] W.E. Pickett, E.H. Krakauer, D.A. Papaconstantopoulos, and L. Boyer. *Phys. Rev. B*, 35:7252, 1987.

[103] A. Kampf and J.R. Schrieffer. *Phys. Rev. B*, 41:6399, 1990.

[104] M. Vekic and S.R. White. *Phys. Rev. B*, 47:1160, 1993.

[105] R. White. *Quantum Theory of Magnetism*. Springer 3rd Edition, Berlin, 2006.

[106] S. Moukouri and M. Jarrell. *Phys. Rev. Lett*, 87:167010–1, 2001.

[107] M.J. Rozenberg, G. Kotliar, H. Kajueter, G.A. Thomas, D.H. Rapkine, J.M. Honig, and P. Metcalf. *Phys. Rev. Lett*, 75:105, 1995.

[108] Y. Maeno, T.M. Rice, and M. Sigrist. *Physics Today*, 54:42, 2001.

[109] T. Oguchi. *Phys. Rev. B*, 51:1385, 1995.

[110] D. Singh. *Phys. Rev. B*, 52:1358, 1995.

[111] Z.V. Pchelkina, I.A. Nekrasov, Th. Pruschke, A. Sekiyama, S. Suga, V.I. Anisimov, and D. Vollhardt. *Phys. Rev. B*, 75:035122, 2007.

[112] S. Nakatsuji and Y. Maeno. *Phys. Rev. Lett*, 84:2666, 2000.

[113] K.T. Park. *J. Phys. Cond. Mat*, 13:9231, 2001.

[114] L.M. Woods. *Phys. Rev. B*, 62:7833, 2000.

[115] S. Nakatsuji and Y. Maeno. *Phys. Rev. B*, 62:6458, 2000.

[116] V.I. Anisimov, I.A. Nekrasov, D.E. Kondakov, T.M. Rice, and M. Sigrist. *Eur. Phys. J. B*, 25:191, 2002.

[117] A. Liebsch. *Phys. Rev. Lett*, 91:226401–1, 2003.

[118] Akihisa Koga, Norio Kawakami, T.M. Rice, and Manfred Sigrist. *Phys. Rev. Lett*, 92:216402–1, 2004.

[119] Akihisa Koga and Norio Kawakami. *Phys. Rev. B*, 72:045128–1, 2005.

[120] S. Biermann, L.de Medici, and A. Georges. *Phys. Rev. Lett*, 95:206401, 2005.

[121] Kensuke Inaba and Akihisa Koga. *Phys. Rev. B*, 73:155106–1, 2006.

[122] C. Knecht, N. Blümer, and P.G.J. van Dongen. *Phys. Rev. B*, 72:081103–1, 2005.

[123] A. Liebsch. *Phys. Rev. Lett*, 95:116402, 2005.

[124] A. Liebsch and H. Ishida. *Phys. Rev. Lett*, 98:216403, 2007.

[125] R. Jin, J.R. Thompson, J. He, J.M. Farmer and. N. Lowhorn, Jr G.A. Lamberton, T.M Tritt, and D. Mandrus. *arxiv. cond. mat*, 0112405v1, 2001.

[126] S.C. Wang et.al. *Phys. Rev. Lett*, 17:177007–1, 2004.

[127] J.S. Lee, S.J. Moon, T.W. Noh, S. Nakatsuji, and Y. Maeno. *Phys. Rev. Lett*, 96:057401, 2006.

[128] M. Neupane, P. Richard, Z.-H. Pan Y.-M. Xu, R. Jin, D. Mandrus, X. Dai, Z. Fang, Z. Wang, and H. Ding. *Phys. Rev. Lett*, 103:097001, 2009.

[129] E. Jakobi, N. Blümer, and P.G.J. van Dongen. *Phys. Rev. B*, 80:115109, 2009.

[130] Y. Koyama, A. Koga, N. Kawakami, and P. Werner. *Phys. Rev. B*, 404:3267, 2009.

[131] K. Bouadim, G.G. Batrouni, and R.T. Scalettar. *Phys. Rev. Lett*, 102:226402–1, 2009.

[132] R. Blankenbecler, D.J. Scalapino, and R.L. Sugar. *Phys. Rev. D*, 24:2278, 1981.

[133] H. Lee, Y.Z. Zhang, H.O. Jeschke, and R.Valenti. *Phys. Rev. Lett*, 104:026402, 2010.

[134] L. Degiorgi, P. Wachter, M.B. Maple, M.C. de Andrade, and J. Herrmann. *Phys. Rev. B*, 54:6065, 1996.

ERKLÄRUNG

Ich versichere, dass ich die von mir vorgelegte Dissertation selbständig angefertigt, die benutzten Quellen und Hilfmittel vollständig angegeben und die Stellen der Arbeit - einschliesslich Tabellen, Karten, und Abbildungen -, die anderen Werken im Wortlaut oder dem Sinn nach entnommen sind, in jedem Einzelfall als Entlehnung kenntlich gemacht habe

ACKNOWLEDGEMENT

Throughout the course of my thesis work, I have incurred debts of gratitude to numerous individuals who, in various ways, have given me valuable help to bring this work to completion. Herein, I would like to express my profound thanks to them. My sincere gratitude goes to my advisor Prof. Jamal Berakdar for his guidance and continued support at all stages of my thesis. I am particularly grateful for giving me the freedom to explore the world of correlated systems such that I can enhance my knowledge in this fascinating field. I also feel grateful to Prof. Trimper and Prof. Potthoff for their willingness to act as referees.

I would like to acknowledge my present and former colleagues at the group of non-equilibrium many-body physics: Alexander, Andrei, Anita, Jia, my office mate Koray, Yaroslav, Zhen Gang, Levan, Nick, Johannes and Ahsan. I enjoyed a research atmosphere in our group as well as our interesting discussions on various topics in many occasions particularly during lunch time. Special thanks to Yaroslav for many stimulating discussions on physics and computational methods and also for the prompt response in resolving many issues concerning the computer systems. Thanks also to fellows of Max Planck with whom I had a delightful conversation particularly Ren bin who consistently complained about his experimental instruments and himself.

My whole family deserve the warmest gratitude, my parents, *inangtua*, brother and sisters, for their compassion, pray and unwavering support over the years. I also wish to express the memory of my father who always supported for higher education yet could not see the end of this work. I always smile when I think of him. Let me also thank God for illuminating the path and for the inspiration. I thank also those who I could not explicitly mention here.

Finally I wish to extend my acknowledgement to the Max-Planck Institute with the International Max-Planck research school program for the financial support that made this research possible. *Horas!*